

AD-A197 316

NAVAL POSTGRADUATE SCHOOL
Monterey, California



THESIS

DTIC
ELECTE
AUG 23 1988
S H D

MULTISPECTRAL SATELLITE ANALYSIS OF
MARINE STRATOCUMULUS CLOUD
MICROPHYSICS

by

Gary M. Mineart

March 1988

Thesis Advisor

Philip A. Durkee

Approved for public release; distribution is unlimited.

Unclassified

Security classification of this page

REPORT DOCUMENTATION PAGE

1a Report Security Classification Unclassified		1b Restrictive Markings	
2a Security Classification Authority		3 Distribution Availability of Report Approved for public release; distribution is unlimited.	
4b Declassification Downgrading Schedule		5 Monitoring Organization Report Number(s)	
6a Name of Performing Organization Naval Postgraduate School		7a Name of Monitoring Organization Naval Postgraduate School	
6b Office Symbol (if applicable) 35		7b Address (city, state, and ZIP code) Monterey, CA 93943-5000	
8a Name of Funding Sponsoring Organization		9 Procurement Instrument Identification Number	
8b Office Symbol (if applicable)		10 Source of Funding Numbers	
9c Address (city, state, and ZIP code)		Program Element No Project No Task No Work Unit Accession No	
11 Title (include security classification) MULTISPECTRAL SATELLITE ANALYSIS OF MARINE STRATOCUMULUS CLOUD MICROPHYSICS			
12 Personal Author(s) Gary M. Mineart			
13a Type of Report Master's Thesis		13b Time Covered From To	
14 Date of Report (year, month, day) March 1988		15 Page Count 149	
16 Supplementary Notation The views expressed in this thesis are those of the author and do not reflect the official policy or position of the Department of Defense or the U.S. Government.			
17 Cosati Codes		18 Subject Terms (continue on reverse if necessary and identify by block number)	
Field	Group	Subgroup	FIRE, satellite analysis, cloud microphysics, marine stratocumulus, aerosol, cloud droplet distribution, cloud reflectance
19 Abstract (continue on reverse if necessary and identify by block number) Variations in marine stratocumulus cloud microphysics during FIRE IFO 1987 are observed and analyzed through the use of NOAA-9/10 AVHRR satellite data and aircraft in-cloud measurements. The relationships between channel 3 reflectance and cloud microphysical properties are examined through model reflectances based on Mie theory and the delta-Eddington approximation, and reveal a channel 3 reflectance dependence on cloud droplet size distribution. The satellite observations show significant regions of continental influence over the ocean through higher channel 3 reflectances resulting from the injection of continental aerosols and the associated modification of cloud droplet characteristics. Additionally, channel 3 reflectance gradients across individual cloud elements correspond to radially varying cloud droplet size distributions within the elements. Various mesoscale and microscale features such as ship stack effluent tracks and pollution sources are observed in the data. Correlations between reflectance values and aircraft measurements illustrate the potential of estimating cloud droplet size distribution and marine atmospheric boundary layer aerosol composition and concentration through the use of satellite data. Such an estimation technique may prove useful in determining the climatic implications of cloud reflectance changes due to the influence of natural and man-made aerosol sources, and provide a means to assess the performance of boundary layer electro-optic systems.			
20 Distribution Availability of Abstract <input checked="" type="checkbox"/> unclassified unlimited <input type="checkbox"/> same as report <input type="checkbox"/> DTIC users		21 Abstract Security Classification Unclassified	
22a Name of Responsible Individual Philip A. Durkee		22b Telephone (include Area code) (408) 646-3465	
		22c Office Symbol 63De	

DD FORM 1473,84 MAR

83 APR edition may be used until exhausted
All other editions are obsolete

Security classification of this page

Unclassified

Approved for public release; distribution is unlimited.

Multispectral Satellite Analysis of
Marine Stratocumulus Cloud
Microphysics

by

Gary M. Mineart
Lieutenant, United States Navy
B.S., Iowa State University, 1980

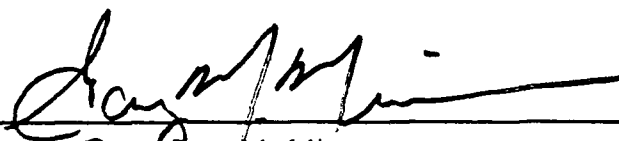
Submitted in partial fulfillment of the
requirements for the degree of

MASTER OF SCIENCE IN METEOROLOGY AND OCEANOGRAPHY

from the

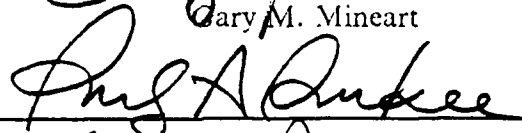
NAVAL POSTGRADUATE SCHOOL
March 1988

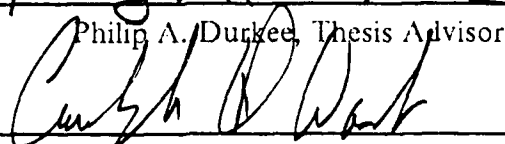
Author:

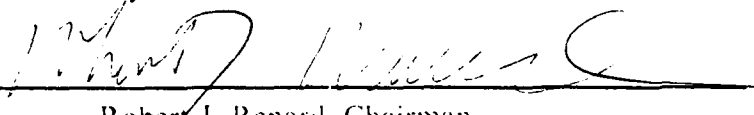



Gary M. Mineart

Approved by:



Philip A. Durkee, Thesis Advisor

Carlyle H. Wash, Second Reader

Robert J. Renard, Chairman,
Department of Meteorology

Gordon E. Schacher,
Dean of Science and Engineering

ABSTRACT

Variations in marine stratocumulus cloud microphysics during FIRE IFO 1987 are observed and analyzed through the use of NOAA-9/10 AVHRR satellite data and aircraft in-cloud measurements. The relationships between channel 3 reflectance and cloud microphysical properties are examined through model reflectances based on Mie theory and the delta-Eddington approximation, and reveal a channel 3 reflectance dependence on cloud droplet size distribution. The satellite observations show significant regions of continental influence over the ocean through higher channel 3 reflectances resulting from the injection of continental aerosols and the associated modification of cloud droplet characteristics. Additionally, channel 3 reflectance gradients across individual cloud elements correspond to radially varying cloud droplet size distributions within the elements. Various mesoscale and microscale features such as ship stack effluent tracks and pollution sources are observed in the data. Correlations between reflectance values and aircraft measurements illustrate the potential of estimating cloud droplet size distribution and marine atmospheric boundary layer aerosol composition and concentration through the use of satellite data. Such an estimation technique may prove useful in determining the climatic implications of cloud reflectance changes due to the influence of natural and man-made aerosol sources, and provide a means to assess the performance of boundary layer electro-optic systems.

iii

Obtained from the color plates: All color reproductions will be in black and white.

Accession For	
NTIS GRA&I	<input checked="" type="checkbox"/>
DTIC TAB	<input type="checkbox"/>
Unannounced	<input type="checkbox"/>
Justification	
By	
Distribution/	
Availability Codes	
Dist	Avail and/or Special
A-1	

TABLE OF CONTENTS

I. INTRODUCTION	1
A. ELECTRO-OPTIC SYSTEM DEPENDENCE ON AEROSOLS AND CLOUD DROPLETS	1
B. CLIMATIC VARIABILITY DUE TO THE RADIATIVE CONTRIB- UTION OF CLOUDS AND AEROSOLS	2
C. THE FIRST ISCCP REGIONAL EXPERIMENT (FIRE)	3
D. THESIS OBJECTIVE	5
II. THEORETICAL BACKGROUND	7
A. CLOUD MICROPHYSICS	7
1. Aerosols and Aerosol Distribution Spectra	7
2. Effect of Aerosols on Cloud Droplet Formation and Distribution	7
3. Cloud Droplet Spectra Observed in Marine Stratocumulus Clouds	10
B. RADIATIVE TRANSFER PRINCIPLES	11
1. Total Radiance	11
2. Cloud Radiative Processes	15
a. Overview	15
b. Spectral Variations	18
c. Anisotropy	20
C. MODEL REFLECTANCE OF MARINE STRATOCUMULUS CLOUDS	20
1. Reflectance Calculations	20
2. Reflectance Variability	24
III. DATA ANALYSIS	31
A. SATELLITE DATA PROCESSING	31
1. Channel 1	31
2. Channel 3	32
3. Channel 4	33
4. Composite Images	33
B. AIRCRAFT DATA	34

IV. CASE STUDY RESULTS AND EVALUATION	36
A. FIRE IFO 1987 CASE STUDIES	36
1. CS1 (28-30 June)	36
a. Synoptic Summary	36
b. AVHRR Subscenes	37
c. Reflectance Cross-Sections	53
d. Aircraft Data	63
2. CS2 (13-14 July)	65
a. Synoptic Summary	65
b. AVHRR Subscenes	71
c. Reflectance Cross-Sections	83
d. Aircraft Data	92
3. CS3 (6 July)	95
a. Synoptic Summary	95
b. AVHRR Subscene	97
c. Reflectance Cross-Sections	99
4. CS4 (18 July)	102
a. Synoptic Summary	102
b. AVHRR Subscene	103
c. Reflectance Cross-Sections	104
d. Aircraft Data	111
5. Reflectance Analysis	113
V. CONCLUSIONS AND RECOMMENDATIONS	119
A. CONCLUSIONS	119
B. RECOMMENDATIONS	121
APPENDIX COMPOSITE IMAGES	124
LIST OF REFERENCES	134
INITIAL DISTRIBUTION LIST	137

LIST OF TABLES

Table 1. Continental/Marine Stratocumulus Cloud Parameters	13
Table 2. Modified Gamma Distribution Empirical Constants	21
Table 3. Mie Output Parameters for $0.63\mu\text{m}$	23
Table 4. Mie Output Parameters for $3.70\mu\text{m}$	24
Table 5. Delta-Eddington Reflectances for $0.63\mu\text{m}$	29
Table 6. Delta-Eddington Reflectances for $3.70\mu\text{m}$	30
Table 7. CS1 Satellite Subscenes	45
Table 8. Selected NCAR Electra Data for 29 June 1987	63
Table 9. Selected NCAR Electra Data for 30 June 1987	67
Table 10. CS2 Satellite Subscenes	71
Table 11. Selected NCAR Electra Data for 14 July 1987	94
Table 12. Selected NCAR Electra Data for 18 July 1987	111

LIST OF FIGURES

Fig. 1. FIRE IFO 1987 Operations Area	4
Fig. 2. Idealized Aerosol Distribution Spectra	8
Fig. 3. Profiles of Stratocumulus Cloud Droplet Parameters	11
Fig. 4. Profiles of Equivalent Liquid Water Content (EQLWC)	12
Fig. 5. Mie scattering efficiency factor (Q)	16
Fig. 6. Model Cloud Droplet Distributions	22
Fig. 7. Reflectance versus Droplet Radius for $z = 0.25$ km	26
Fig. 8. Reflectance versus EQLWC for $z = 0.25$ km	27
Fig. 9. Reflectance versus Cloud Thickness (z)	28
Fig. 10. 29 June 1987 12 UTC Regional OI Analysis	38
Fig. 11. 30 June 1987 12 UTC Regional OI Analysis	39
Fig. 12. San Nicolas Island Rawinsonde Sounding	40
Fig. 13. NORAPS 29 June 1987 00-24 UTC Parcel Trajectories	41
Fig. 14. NORAPS 29 June 1987 00-24 UTC Parcel Trajectories	42
Fig. 15. NORAPS 30 June 1987 00-24 UTC Parcel Trajectories	43
Fig. 16. NORAPS 30 June 1987 00-24 UTC Parcel Trajectories	44
Fig. 17. NOAA-10 AVHRR 1639 UTC 28 June 1987 Channel 1	46
Fig. 18. NOAA-10 AVHRR 1639 UTC 28 June 1987 Channel 3 Reflectance	47
Fig. 19. NOAA-9 AVHRR 2230 UTC 29 June 1987 Channel 1	48
Fig. 20. NOAA-9 AVHRR 2230 UTC 29 June 1987 Channel 3 Reflectance	49
Fig. 21. NOAA-10 AVHRR 1555 UTC 30 June 1987 Channel 1	50
Fig. 22. NOAA-10 AVHRR 1555 UTC 30 June 1987 Channel 3 Reflectance	51
Fig. 23. CS1 Continental/Marine Air Mass Interface	54
Fig. 24. Reflectance Cross-Sections A and B	55
Fig. 25. Reflectance Cross-Section C	56
Fig. 26. Reflectance Cross-Section D	58
Fig. 27. Reflectance Cross-Section E	59
Fig. 28. Reflectance Cross-Section F	60
Fig. 29. Reflectance Cross-Section G	61
Fig. 30. Reflectance Cross-Section H	62
Fig. 31. NCAR Electra Flight Track, 29 June 1987	64

Fig. 32. NCAR Electra Flight Track, 30 June 1987	65
Fig. 33. FSSP Probe Droplet Size Distribution Histograms for 30 June 1987	66
Fig. 34. 13 July 1987 12 UTC Regional OI Analysis	68
Fig. 35. 14 July 1987 12 UTC Regional OI Analysis	69
Fig. 36. Research Vessel POINT SUR Rawinsonde Soundings	70
Fig. 37. NORAPS 12 July 1987 00-24 UTC Parcel Trajectories	72
Fig. 38. NORAPS 12 July 1987 00-24 UTC Parcel Trajectories	73
Fig. 39. NORAPS 13 July 1987 00-24 UTC Parcel Trajectories	74
Fig. 40. NORAPS 13 July 1987 00-24 UTC Parcel Trajectories	75
Fig. 41. NOAA-10 AVHRR 1613 UTC 13 July 1987 Channel 1	76
Fig. 42. NOAA-10 AVHRR 1613 UTC July 1987 Channel 3 Reflectance	77
Fig. 43. NOAA-9 AVHRR 2321 UTC 13 July 1987 Channel 1	79
Fig. 44. NOAA-9 AVHRR 2321 UTC 13 July 1987 Channel 3 Reflectance	80
Fig. 45. NOAA-10 AVHRR 1551 UTC 14 July 1987 Channel 1	81
Fig. 46. NOAA-10 AVHRR 1551 UTC 14 July 1987 Channel 3 Reflectance	82
Fig. 47. NOAA-9 AVHRR 2310 UTC 14 July 1987 Channel 1	84
Fig. 48. NOAA-9 AVHRR 2310 UTC 14 July 1987 Channel 3 Reflectance	85
Fig. 49. CS2 Continental/Marine Air Mass Interface	86
Fig. 50. Reflectance Cross-Sections M and N	88
Fig. 51. Reflectance Cross-Sections O and P	89
Fig. 52. Reflectance Cross-Sections Q and R	90
Fig. 53. Reflectance Cross-Section S	91
Fig. 54. Reflectance Cross-Section T	92
Fig. 55. Reflectance Cross-Section U	93
Fig. 56. NCAR Electra Flight Track, 14 July 1987	95
Fig. 57. Size Distribution Histograms for 14 July 1987	96
Fig. 58. 6 July 1987 12 UTC Regional OI Analysis	98
Fig. 59. San Nicolas Island Rawinsonde Sounding	99
Fig. 60. NOAA-10 AVHRR 1524 UTC 6 July 1987 Channel 1	100
Fig. 61. NOAA-10 AVHRR 1524 UTC 6 July 1987 Channel 3 Reflectance	101
Fig. 62. Reflectance Cross-Section I	102
Fig. 63. Reflectance Cross-Section J	103
Fig. 64. Reflectance Cross-Sections K and L	104
Fig. 65. 18 July 1987 12 UTC Regional OI Analysis	105

Fig. 66. Vandenburg AFB Rawinsonde Sounding	106
Fig. 67. NOAA-10 AVHRR 1604 UTC 18 July 1987 Channel 1	107
Fig. 68. NOAA-10 AVHRR 1604 UTC 18 July 1987 Channel 3 Reflectance	108
Fig. 69. Two-Dimensional Reflectance Cross-Section V	109
Fig. 70. Two-Dimensional Reflectance Cross-Section W	110
Fig. 71. NCAR Electra Flight Track, 18 July 1987	112
Fig. 72. Size Distribution Histograms for 18 July 1987	114
Fig. 73. Reflectance verses FSSP Mean Droplet Radius	115
Fig. 74. Channel 1 Reflectance verses Cloud Thickness	117
Fig. 75. Channel 3 Reflectance verses Droplet Radius	118
Fig. 76. NOAA-10 AVHRR 1639 UTC 28 June 1987 Composite Image	125
Fig. 77. NOAA-9 AVHRR 2230 UTC 29 June 1987 Composite Image	126
Fig. 78. NOAA-10 AVHRR 1555 UTC 30 June 1987 Composite Image	127
Fig. 79. NOAA-10 AVHRR 1613 UTC 13 July 1987 Composite Image	128
Fig. 80. NOAA-9 AVHRR 2321 UTC 13 July 1987 Composite Image	129
Fig. 81. NOAA-10 AVHRR 1551 UTC 14 July 1987 Composite Image	130
Fig. 82. NOAA-9 AVHRR 2310 UTC 14 July 1987 Composite Image	131
Fig. 83. NOAA-10 AVHRR 1524 UTC 6 July 1987 Composite Image	132
Fig. 84. NOAA-10 AVHRR 1604 UTC 18 July 1987 Composite Image	133

ACKNOWLEDGEMENTS

The author wishes to thank Professor Philip A. Durkee for his guidance, insight, support and assistance throughout the course of this research. His attention to detail contributed a great deal to the success of this work. Professor Carlyle H. Wash is thanked for his careful review of the manuscript and for his helpful comments. Much appreciation is extended to the staff of the Naval Postgraduate School's Interactive Digital Environmental Analysis (IDEA) Laboratory, especially to Mr. Richard A. Kohrs for his assistance in satellite data navigation and processing, and to Mr. Craig E. Motell for his role in improving the capabilities of the satellite data processing code. The author wishes to thank Mr. Rolf Langland of the Naval Environmental Prediction Research Facility for providing applicable synoptic forecast products and trajectory data. In addition, Mr. Robert Whritner of the Scripps Institution of Oceanography Satellite Oceanography Facility is thanked for his support and guidance during satellite data collection. The entire science experiment team for the First ISCCP Regional Experiment (FIRE) marine stratocumulus field observations held in the summer of 1987 is thanked for allowing the author to participate as a contributing member of this significant event. Finally, a special loving thanks to the author's wife Janis and children Daniel and Emily, whose steadfast patience and understanding throughout this effort have paid incalculable dividends.

I. INTRODUCTION

A. ELECTRO-OPTIC SYSTEM DEPENDENCE ON AEROSOLS AND CLOUD DROPLETS

The molecular and aerosol components of the atmosphere which are within an order of magnitude of the operating wavelength of a military sensor or weapons system may absorb emitted energy, or scatter a large percentage of it out of the beam path, severely reducing its efficiency. Infrared wavelength imaging and ranging systems, currently deployed in numerous military applications, are shown by Milton *et al.* (1977) to be profoundly affected by variable distributions of atmospheric aerosols. Laser systems are also strongly affected, especially systems designed to operate from ground-based or shipboard platforms where beam paths are confined to the lower atmosphere. According to Bloembergen *et al.* (1987), the optimum wavelength region for laser systems is 0.4-1.0 μ m. This band avoids severe attenuation from atmospheric molecular components at short wavelengths and water vapor absorption at longer wavelengths. Atmospheric aerosols in this band are still strong contributors to energy losses. Cordray *et al.* (1977) describes meteorological effects on a horizontally propagating deuterium fluoride chemical laser operating at 3.2 μ m in the lower atmosphere, and recognizes that aerosol density, size distribution, and chemical and physical composition constitute most of the meteorological parameters affecting laser sensitivity. The aerosol contribution is critical and Cordray *et al.* recommends real-time microscale measurement capability at each sensor platform in order to assess and predict the performance of friendly and threat electro-optic systems, and to plan strategy and tactics. A knowledge of the exact aerosol size distribution is especially valuable for free electron lasers since they possess a variable output wavelength which can be adjusted to minimize atmospheric effects. Although several high power chemical laser systems have already been built and their use has been under study much longer than other directed energy systems, Bloembergen *et al.* (1987) state that these lasers are less attractive candidates for weapons systems. While chemical lasers are closest to the required performance levels in a relative sense; technological limitations, primarily the inability to avoid atmospheric degradation, will require an increase in laser output power over current maximum operational levels in order for the weapons systems to be effectively lethal.

It is clear that the ability to assess the distribution of atmospheric particulates on a real-time basis is essential in order to optimize the performance of each electro-optic emitter. Liquid water in the form of cloud droplets severely attenuates electro-optic energy. In stratoform clouds confined to the lower atmosphere, cloud droplet size distribution is a function of the resident aerosol population and may indicate the concentration and general composition of coincident aerosols. Thus, the cloud droplet size distribution may serve as a measure of the potential effectiveness of electro-optic systems.

B. CLIMATIC VARIABILITY DUE TO THE RADIATIVE CONTRIBUTION OF CLOUDS AND AEROSOLS

The scattering and absorption of solar radiation by clouds and aerosol particles influences the earth's energy budget and thus can have an impact on variations in climate. The possible climatic effects from an increasing concentration of man-made aerosols through industrial pollution and other sources has received global attention from the scientific community and the media. A description of the effect of aerosols on the transfer of radiant energy in the atmosphere is provided by Coakley *et al.* (1983). Inclusion of the exact aerosol effect in climate models is difficult since the shape, index of refraction, size distribution, concentration and spatial variability of the aerosols must be known in principle, and these parameters are either too complex to describe or virtually impossible to quantify due to unknown initial conditions and temporal variations. Most climate models rely on broad approximations to describe the distribution of these constituents.

Apart from the direct effect of aerosols on the transfer of solar radiation, Twomey *et al.* (1984) showed that aerosols can affect the radiative properties of clouds and create an additional influence on the radiation balance. According to Coakley *et al.* (1987), the effect of aerosols on the earth's radiation budget through their influence on clouds may be *several times* that of the direct interaction of the aerosol with solar radiation. Aerosols are the primary source of nuclei around which cloud droplets and ice crystals form. These cloud condensation nuclei (CCN), which may be less than $0.01\mu\text{m}$ in diameter, can rapidly form cloud droplets of several micrometers in radius upon entering a suitable supersaturated environment. While the minute CCN have only a weak effect on the transfer of radiation, the cloud droplets which form on them have a major impact on the radiation balance. Charlson *et al.* (1987) showed the importance of phytoplankton-produced dimethylsulphide (DMS) gas in the marine environment. The sulfate particles

that form when DMS oxidizes may be the principal source of CCN in marine air. This implies that oceanic biological variability may play a major role in marine cloud albedo changes and in planetary climatic trends. The inclusion of variable aerosol contributions to the radiative properties of cloud fields, such as continental pollution sources or increases in DMS concentration, has yet to be completely examined on a regional or global scale.

C. THE FIRST ISCCP REGIONAL EXPERIMENT (FIRE)

FIRE is a multidisciplinary research program in support of the International Satellite Cloud Climatology Program (ISCCP) to study the roles that clouds play in the global climate. The objectives and milestones for FIRE are enumerated by Randall *et al.* (1984) and detailed by Cox *et al.* (1987). The 43 members of the initial FIRE science experiment team conceived of the following six general objectives for the experiment:

1. characterization of clouds,
2. validation and improvement of satellite cloud-retrieval techniques,
3. improvement of cloud radiation models,
4. description of cloud space/time statistics,
5. improvement of cloud dynamics models, and
6. validation and improvement of general circulation model cloud parameterizations.

The data for this thesis were collected during the first marine stratocumulus intensive field observations (IFO), conducted from 29 June to 20 July 1987 off the southern California coast as shown in Fig. 1. This IFO was the first of two planned for marine stratocumulus cloud field measurements. It included a variety of meteorological and surface radiation measurements conducted from San Nicolas Island, including an instrumented 19-meter tower for moisture and heat flux measurements, two tethered balloons which probed the marine atmospheric boundary layer (MABL) structure, a microwave radiometer, a Doppler radar and sodar, and rawinsonde releases from the island itself and from the research vessel POINT SUR operating upwind from the island. Five aircraft participated in the measurement effort: the National Aeronautics and Space Administration (NASA) high-altitude ER-2, the University of Washington C-131, the National Center for Atmospheric Research (NCAR) Electra, a C-130 operated by the British Meteorological Office, and a Piper Navaho provided by the Naval Ocean Systems Center (NOSC). The individual capabilities of these aircraft, as well as the

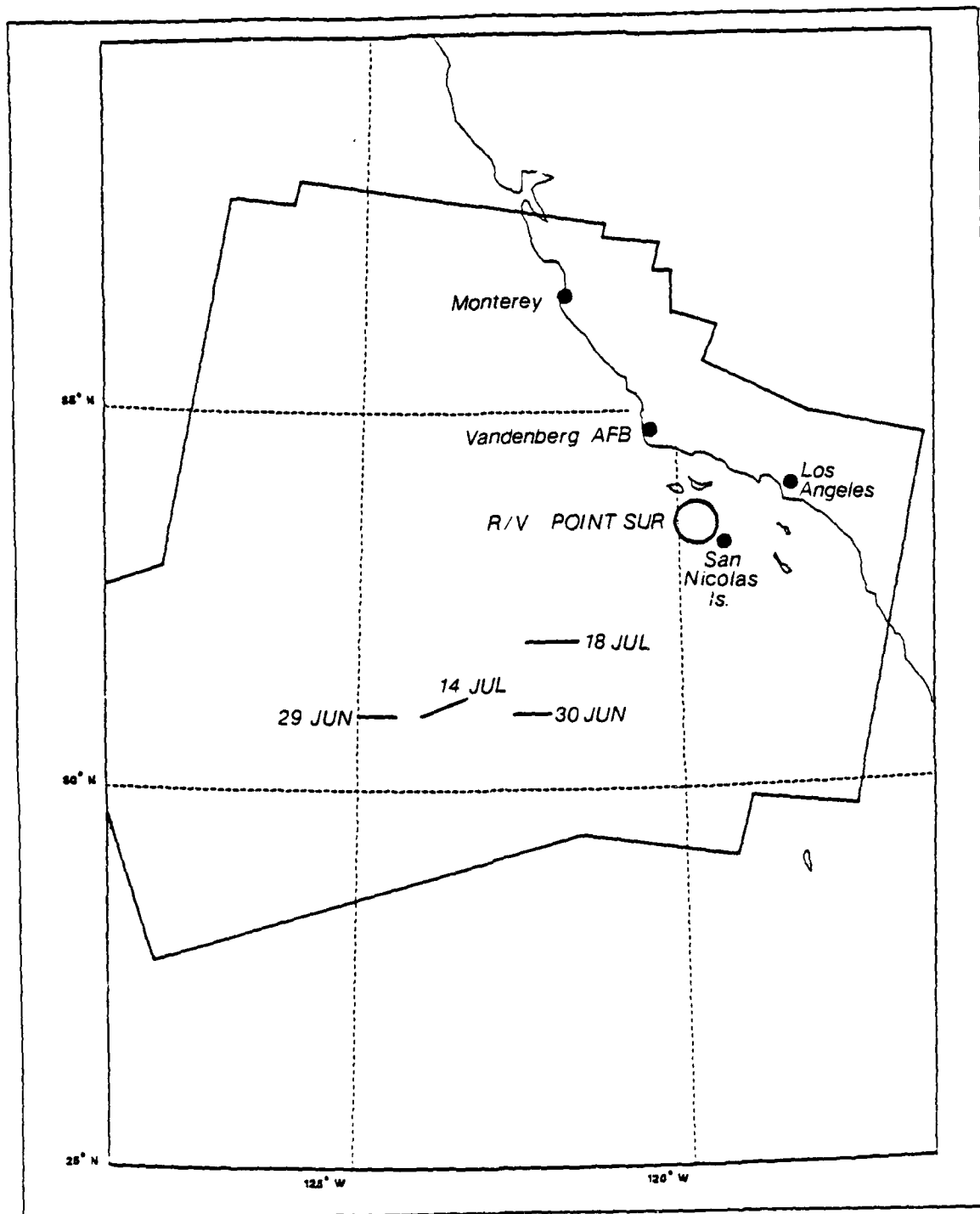


Fig. 1. FIRE IFO 1987 Operations Area: Outlined area indicates region encompassing case study satellite subscenes; line segments are applicable case study aircraft mission tracks.

other ground and satellite-based measurement systems, are described by Cox *et al.* (1987). Aircraft operations were coordinated with various satellite overflights.

The satellite data utilized in this thesis are from the National Oceanic and Atmospheric Administration (NOAA) polar orbiting platforms' (NOAA-9/10) Advanced Very High Resolution Radiometer (AVHRR) collected at the Scripps' Satellite Oceanography Facility. Cloud microphysical data illustrated herein were obtained by sensors aboard the NCAR Electra during MABL cloud-penetrating missions in support of the IFO. Data for use in trajectory analyses are provided by the Fleet Numerical Oceanography Center (FNOC) Navy Operational Regional Analysis and Prediction System (NORAPS) forecast model. Synoptic summaries are derived from National Meteorological Center (NMC) regional optimal interpolation (OI) analyses.

Kloesel *et al.* (1988) provides a summary of FIRE IFO 1987 operations and synoptic conditions. The data in this summary are utilized in this thesis to describe synoptic effects and to fix the geographic positions of aircraft flight tracks.

D. THESIS OBJECTIVE

The objective of this thesis is to demonstrate the ability to deduce cloud microphysical parameters (primarily cloud droplet size distribution) of marine stratocumulus clouds utilizing AVHRR high resolution picture transmission (HIRPT) satellite data. The boundary between air masses of continental and marine origin are highlighted; however, additional phenomena previously observed by Coakley *et al.* (1987), Coakley and Davies (1986), and Rogers (1987) are observed, such as cloud edge effects and tracks resulting from the discharge of ship stack effluents. A multispectral image processing technique is used which combines AVHRR channels 1, 3 and 4. This technique relies on the basic physical principles of radiative transfer in the atmosphere rather than complex image enhancement schemes. Channel 1 provides cloud solar reflectance in visible wavelengths which is corrected for anisotropy during processing. The thermal emission contribution to the near-infrared (NIR) channel 3 is removed using the thermal emission measured in channel 4, and the remaining reflectance value is corrected for anisotropy. In addition to providing thermal emission values for channel 3 correction, channel 4 temperature is utilized as a threshold to mask the contribution from any cloud elements which might exist above the MABL. The resulting reflectance values are compared to theoretical calculations and aircraft measurements in order to determine the relationship between solar reflectance and the microphysical properties of stratocumulus clouds and their co-existent MABL during the IFO. This will be accomplished using

relationships between reflectance and cloud microphysics illustrated in this thesis. The ability to discern boundary layer air mass characteristics through remote sensing techniques provides the opportunity to determine broad-scale effects of MABL composition changes on the earth's radiative balance, as well as assess the range-dependent performance of directed energy systems.

In Chapter II the necessary theoretical background is presented. A discussion of the relationship between the distribution of aerosols, cloud droplets and droplet spectra observed in marine stratocumulus clouds is followed by an illustration of applicable radiative transfer principles, including variations expected in marine stratocumulus clouds. Model-generated reflectances for marine stratocumulus clouds are illustrated and discussed. Chapter III describes the satellite data and details image processing. Finally, Chapter IV illustrates four case studies from FIRE IFO 1987. Each case study includes a synoptic description, applicable satellite images, an analysis of cross-sections of solar reflectance, a comparison with theoretical expectations, and a comparison with the NCAR Electra cloud microphysics data for the satellite passes with aircraft mission coincidence.

II. THEORETICAL BACKGROUND

A. CLOUD MICROPHYSICS

This section describes basic cloud microphysical parameters which drive variations in radiative properties. Typical aerosol distributions are examined, including their role as CCN and their variation between air masses of continental and marine origin. This is followed by a discussion of the dependence of cloud droplet distribution on the initial aerosol distribution. Finally, typical droplet spectra in marine stratocumulus clouds are observed.

1. Aerosols and Aerosol Distribution Spectra

The atmospheric particles that are larger than the molecular scale can be separated into two categories: (1) cloud droplets and ice crystals, and (2) aerosols. Aerosols range in size from about $0.001\mu\text{m}$ for small ions made up of charged molecular clusters, to more than $10\mu\text{m}$ for the largest dust, salt and combustion particles. The radii of aerosols of optical importance are between 0.01 and $10\mu\text{m}$; cloud droplets are much larger and vary between 1 and $100\mu\text{m}$. Aerosols are concentrated in the lowest few kilometers of the troposphere. According to Chahine *et al.* (1983) their small mass and size allow them to remain suspended in the atmosphere for lifetimes on the order of a week. Variations in concentration and dispersal are governed by wind patterns, so that during their lifetime aerosols may be advected thousands of kilometers and chemically and/or physically interact, resulting in complex shapes and chemical compositions. Brock (1972) states that nearly 75% of the aerosol mass in the atmosphere can be attributed to natural and anthropogenic primary sources such as sea spray (40%), wind-generated dust (20%), fires (10%), and industrial operations and combustion products (5%). The remaining 25% is accounted for by photochemical and other chemical processes which involve conversion of atmospheric gaseous constituents such as DMS to small particles. Aerosols continually undergo a variety of chemical and physical transformations, including coagulation, scavenging, precipitation washout, condensation, sedimentation, dispersion and mixing. Slinn (1975) has provided an idealized presentation of typical aerosol spectra, presented in Fig. 2.

2. Effect of Aerosols on Cloud Droplet Formation and Distribution

In general, aerosols can be classified as hygroscopic, neutral, or hydrophobic depending on their affinity for water. This affinity depends on aerosol solubility which

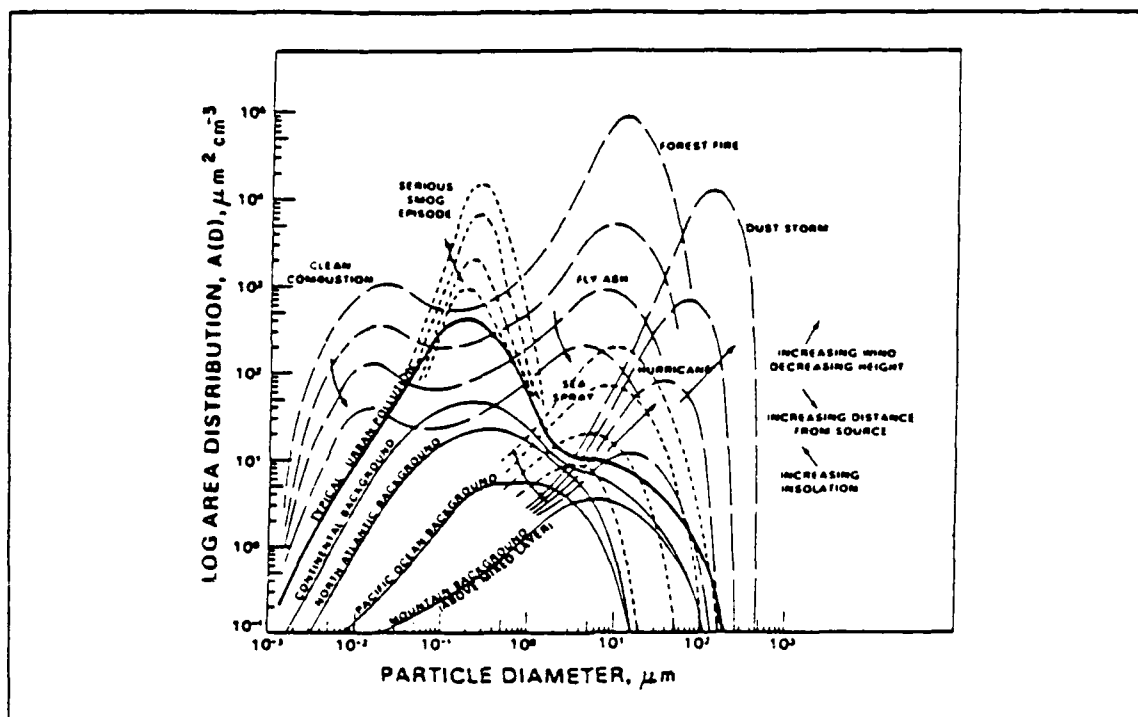


Fig. 2. Idealized Aerosol Distribution Spectra: Includes typical ground-level background distributions and the general dependence of the spectra on height, wind speed, distance from source, and surface heating (from Slinn, 1975).

allows ions to collect on the surface of the growing droplet, attracting additional water vapor and adding to the droplet mass. Cloud droplets form most efficiently on the hygroscopic nuclei. Cloud droplet nucleation on a neutral aerosol requires about the same level of supersaturation as spontaneous or homogeneous nucleation (from Rogers, 1979; the supersaturation required is approximately 300-400 percent excess relative humidity, and these levels are never observed in the atmosphere). Hydrophobic aerosols require even higher supersaturation levels. Soluble hygroscopic aerosols require much lower levels of supersaturation, although the small aerosols made up of ion clusters provide little improvement over homogeneous nucleation, and large ($10\mu\text{m}$) aerosols are of limited importance because of their short residence time and their relatively low concentration. In the atmosphere, the only condensation nuclei (CN) that enter into the cloud droplet formation process nucleate at supersaturations of approximately 1% or less. This subset of the CN distribution defines the CCN. CN and CCN are generally classified according to their geometric size as Aitken or small (radius (r) $< 0.1\mu\text{m}$), large

($0.1\mu\text{m} < r < 1\mu\text{m}$) and giant ($r > 1\mu\text{m}$). Aitken nuclei are products of combustion and natural processes in the atmosphere, while large and giant nuclei are mostly salt particles that result from the bursting of ocean surf bubbles.

It is the role of aerosols as CCN that allows the inference of aerosol distribution based upon the resident cloud droplet distribution. Twomey and Warner (1967) made direct measurements of cloud droplets and nuclei in non-precipitating cumuli with tops warmer than 0°C . They found that cloud nuclei concentration can be used to infer the cloud droplet concentration. The droplet concentration of maritime clouds corresponds to the number of large salt nuclei observed when wind conditions are moderate, on the order of a few tens per cm^3 . Conversely, clouds which form under the influence of continental air usually contain several hundred drops per cm^3 while the number of large nuclei composed of sea salt remain at about 10 per cm^3 . The continental aerosol distribution also contains significant quantities of soluble sulfate components such as sulfuric acid or ammonium sulfate from various natural and man-made sources, and insoluble particles from the soil. Charlson *et al.* (1987) indicates that the droplet concentration of maritime clouds may be more closely tied to the ambient source level of DMS-induced sulfates. Low droplet concentrations in marine clouds may result from a lack of suitable CCN. The relative importance of each of the aerosol constituents depends upon the spatial and temporal history of the associated air mass and its interaction with land and sea surfaces.

An example of a continental influence on aerosol distribution and its associated effect on the concentration of cloud droplets is illustrated by Warner and Twomey (1967). An additional source of CCN observed over maritime regions east of Australia was isolated as cane fire smoke products resulting from inland burning during the harvest season. In this CCN-rich air, cloud droplet concentrations in low-level, warmer than 0°C clouds were observed in concentrations 5 to 10 times higher than had previously been observed in the same maritime region, and 10 or more times higher than the median concentration expected in maritime cumuli. Hindman *et al.* (1977) observes the dependence of cloud droplet size distribution on size-categorized CCN in warm, non-raining clouds. The results of both measurements and calculations show that high concentrations of large and giant CCN lead to droplet size distributions which contain large droplets only if low concentrations of small CCN are present. If high concentrations of small CCN are present, the droplet size distributions contain few, if any, large droplets, regardless of the concentration of the larger CCN. High droplet concentrations are

commonly observed in clouds which contain few large droplets, while low droplet concentrations usually indicate the presence of a greater percentage of large droplets. It appears that the relative concentration of small and large CCN, not the concentration of giant CCN, determines the extent of large droplets in low-level warm cumuli.

3. Cloud Droplet Spectra Observed in Marine Stratocumulus Clouds

The droplet spectra in marine stratocumulus clouds is largely dependent upon the number and chemical nature of the CCN, which are in turn controlled by air mass source, sea-spray aerosols as regulated by the surface wind speed, and oceanic biological activity. Noonkester (1984) made detailed observations of cloud droplet spectra in marine stratus layers 110-150 kilometers southwest of San Diego, CA, in the spring and summer of 1981 (this location coincides with the FIRE IFO 1987 operating area). Two days were selected for study: one day reflecting the influence of a marine air mass (29 May 1981) and the other representing the influence of continental air (18 August 1981). These associations were based on estimates of air parcel trajectories from synoptic analyses. It was observed that droplet spectra on the continental and marine days were different, primarily due to the existence of many more small droplets in air of continental origin. In the upper third of cloud layers, the continental regime surrendered values of 500-600 droplets per cm^3 at an average modal droplet radius (i.e., the radius of peak concentration) near $4\mu m$. The marine case gave droplet concentrations of 200-300 per cm^3 at an average modal radius near $6\mu m$. Fig. 3 shows measurements of these parameters and the mean droplet radius as a function of the distance from the cloud base for both air mass types. Values at various flight levels within the cloud are listed in Table 1.

The equivalent liquid water content (EQLWC) is defined as the mass of the liquid water contained in all of the cloud droplets or ice crystals per unit volume. The EQLWC measured in the vertical by Noonkester (1984) reveal an average value of $0.1 g/m^3$ at mid-cloud levels increasing to $0.3 g/m^3$ near the cloud top for both continental and marine cases as shown in Fig. 4.

Noonkester (1984) also observed that the aerosol spectra in air of continental origin may vary based upon the length of time air parcels may be modified by the marine environment as they pass over ocean surfaces. An air mass off the southern California coast may consist mainly of "fresh" continental CCN due to offshore flow over the adjacent coastline, or may contain "aged" CCN advected into the region from coastal, continental sources farther north (the Pacific Northwest or possibly Canada).

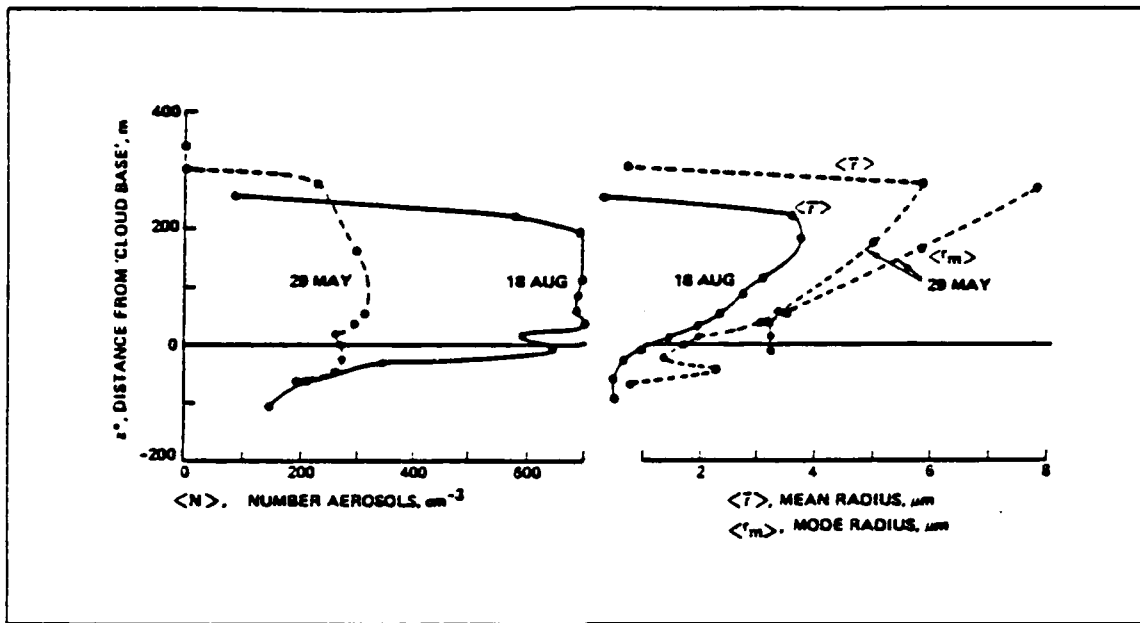


Fig. 3. Profiles of Stratocumulus Cloud Droplet Parameters: Samples are from continental air (18 Aug) and marine air (29 May) through the cloud layer. Dots are sampling elevations (from Noonkester, 1984).

The CCN in the latter have been modified through the addition of marine aerosols and the loss processes described in the previous section.

B. RADIATIVE TRANSFER PRINCIPLES

The satellite data utilized in this thesis comprise three of the five AVHRR channels employed on the NOAA-9/10 polar orbiting platforms. These include channel 1 (0.58-0.68μm bandwidth; centered at 0.63μm) in visible wavelengths, channel 3 (3.55-3.93μm; 3.70μm) in the NIR, and channel 4 (10.30-11.30μm; 11.00μm) in the infrared (IR) region. The following section provides a discussion of the radiative transfer characteristics in these portions of the electromagnetic spectrum in order to understand the methods developed and utilized for satellite image processing. Where appropriate, simplifications are made based on the assumption that only satellite pixels encompassing stratocumulus clouds will be considered in the radiative balance.

1. Total Radiance

The total satellite-measured spectral radiance in units of $W/m^2\text{-sr-}\mu\text{m}$ is given by

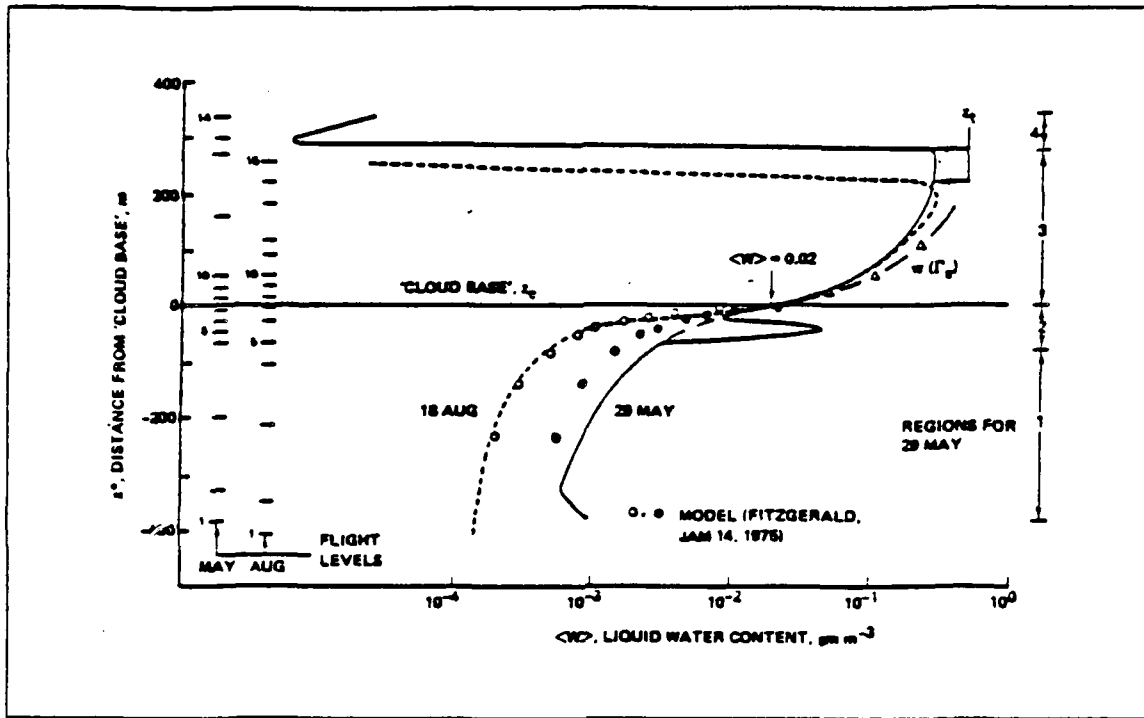


Fig. 4. Profiles of Equivalent Liquid Water Content (EQLWC): The solid curve represents the marine regime, while the dashed curve represents the continental regime. The zero reference level is cloud base, defined to be where EQLWC is 0.02 g/m^3 (from Noonkester, 1984).

$$L_i(\lambda, \theta, \phi) = L_0(\lambda, \theta, \phi) t(\lambda) + \int_0^{\delta(\lambda)} \frac{J^*(\lambda, z, \theta, \phi) t(\lambda, z)}{\sigma_e(\lambda, z)} \frac{d\delta}{\cos \theta}, \quad (1)$$

where

$$t(\lambda) = e^{-\delta(\lambda)/\cos \theta} \quad (2)$$

and

$$t(\lambda, z) = e^{-\delta(\lambda, z)/\cos \theta}. \quad (3)$$

The function $J^*(\lambda, z, \theta, \phi)$ is a combination of thermal emission and scattering given by

$$J^*(\lambda, z, \theta, \phi) = [\varepsilon(\lambda, \vec{x}) B(\lambda, T(\vec{x}))] + \left[\frac{\sigma_s(\lambda) P(\psi_s) L(\lambda) e^{-\delta_s(z)/\cos \theta_0}}{4\pi} \right]. \quad (4)$$

TABLE 1
CONTINENTAL/MARINE STRATOCUMULUS CLOUD PARAMETERS
(after Noonkester, 1984)

Flight Level	Z^* (m from cloud base)	EQLWC (g/m^3)	Number of Droplets at \bar{r} (cm^{-3})	Mean Droplet Radius \bar{r} (μm)
Marine Air Mass Regime				
1	-380	0.00103	21	0.87
4	-63	0.00314	194	0.83
8	18	0.0337	260	2.00
11	167	0.217	296	4.82
12 (CLD TOP)	274	0.288	228	5.77
13	301	0.00001	2	0.70
Continental Air Mass Regime				
1	-407	0.00014	111	0.41
5	-62	0.00054	213	0.49
8	17	0.0374	589	1.48
12	121	0.199	693	3.13
14 (CLD TOP)	222	0.263	575	3.56
15	254	0.00002	90	0.31

The following definitions apply:

- L_i = upwelling radiance,
- λ = wavelength,
- θ = satellite zenith angle,
- ϕ = azimuth angle,
- L_0 = surface radiance,
- δ = optical depth,
- z = vertical distance,
- σ_e = beam attenuation coefficient,
- ϵ = emissivity,
- \vec{x} = elemental position vector,
- B = Planck function,
- σ_v = volume scattering coefficient,

$P(\psi_s)$	= scattering phase function,
L	= incident radiance,
δ_s	= scattering optical depth, and
θ_0	= solar zenith angle.

The first term on the right hand side of Eq. 1 represents the direct surface transmittance, that is, the probability of surface reflected or emitted radiant energy passing unobstructed through the atmosphere. The contribution to total radiance from this term is small for satellite pixels filled with clouds of sufficient thickness. The surface contribution is masked by the clouds in visible wavelengths and is dominated by the clouds in the IR. The reflection and emission from cloud surfaces in the NIR comprise virtually all of the upwelling radiation in these pixels. In addition, reflection off the ocean surface is small in the visible and NIR away from regions of sunglint. In the case of IR wavelengths, the desired quantity is the near-blackbody emission of the stratocumulus clouds. Since the emissivity (absorptivity) of these clouds is close to 1.0, the clouds effectively cancel any contribution from below the cloud layer.

The second term on the right hand side of Eq. 1 accounts for radiance sources and sinks in the path between the surface and the satellite. If it is assumed that the transmissivity between the stratocumulus cloud top and the satellite is 1.0 (no additional clouds or scattering/absorbing media above the stratocumulus cloud top), then this term includes radiant energy scattered out of, and into, the sensed path by elements within the cloud, absorption in the cloud which removes radiation from the sensed path, and cloud droplet emission into the path. The assumption of perfect transmissivity above the clouds is valid since the attenuation contribution of aerosols above the MABL is small. Also, water vapor content falls off sharply above the MABL, especially in the cases during FIRE IFO 1987 where the region remained under the influence of strong, drying subsidence. This, in conjunction with the fact that channels 1 and 3 are in atmospheric "window" regions, minimizes the effect of water vapor on transmissivity. These same assumptions are deemed valid by Bell and Wong (1981) when describing the NIR radiation received by satellite sensors.

With the above assumptions in effect, Eq. 1 may be simplified to the form

$$L_r(\lambda, \theta, \phi) = \varepsilon(\lambda)B(\lambda, T) + \gamma_r(\lambda, \theta_0, \theta, \phi)L \cos \theta_0, \quad (5)$$

where $\gamma_r(\lambda, \theta_0, \theta, \phi)$ is the directional reflectance of the cloud surface received by the satellite. The first term on the right hand side of Eq. 5 is the contribution to measured

radiance due to thermal emission as determined by the Planck function (B) and the emissivity (ϵ) of the cloud surface. The Planck function relates emitted monochromatic intensity with wavelength and cloud surface absolute temperature as follows:

$$B(\lambda, T) = \frac{2hc^2}{\lambda^5 e^{(hc/\lambda kT)} - 1}, \quad (6)$$

with

- h = Planck's constant ($6.6262(10^{-34})$ J sec),
- c = velocity of light ($2.998(10^8)$ m/sec),
- k = Boltzmann's constant ($1.3806(10^{-23})$ J/deg), and
- T = brightness temperature.

The second term on the right hand side of Eq. 5 is the contribution to the upwelling radiance due to solar reflection as determined by the incident solar radiation (L) weighted by the cosine of the solar zenith angle (θ_0) and the directional reflectance (γ_r). The directional reflectance describes reflected energy from some incident direction into a particular outward direction as defined by the solar zenith angle, the satellite zenith angle (θ), and the relative azimuth (ϕ). Relative azimuth is defined as the angle between the projection of the sun-to-pixel and satellite-to-pixel line segments on a horizontal plane.

2. Cloud Radiative Processes

a. Overview

Solar radiation which encounters atmospheric particulates (molecular constituents, aerosols, and cloud droplets or ice crystals) may be transmitted through the atmosphere, or may be absorbed or scattered by those particulates. If the scattering particles are much smaller than the wavelength of the radiant energy, the interactions are described by Rayleigh scattering. Rayleigh scattering efficiency is inversely proportional to the fourth power of wavelength and as such is not important for the wavelengths and droplet sizes of interest in this thesis. If the particle radius and wavelength are comparable, the scattering process is described by Mie theory (Liou, 1980). Under Mie theory, the volume scattering coefficient (σ_v), in units of inverse length, describes the total scattering in a thin horizontal section of the atmosphere and is defined as follows:

$$\sigma_s(\lambda) = \int_0^\infty \pi r^2 Q(\lambda, n, r) n(r) dr, \quad (7)$$

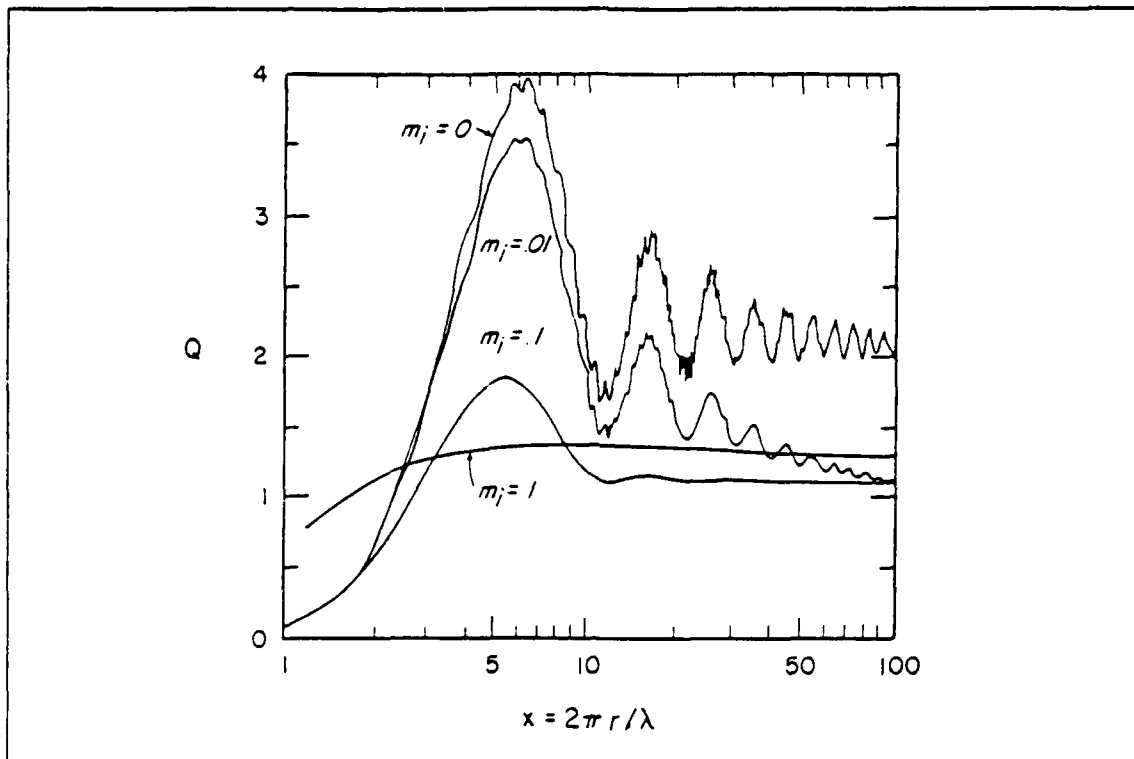


Fig. 5. Mie scattering efficiency factor (Q): Illustrated as a function of the size parameter $x = 2\pi r/\lambda$. The real refractive index is 1.33, with results shown for four values of the imaginary part of the refractive index (after Hansen and Travis, 1974).

where m is the index of refraction. The Mie scattering efficiency factor (Q) is illustrated in Fig. 5 for variable indices of refraction. The real part of the complex index of refraction for pure water is 1.33, while the imaginary part ranges from 0 for a perfect reflector to positive numbers less than unity for absorbing media. The major maxima and minima in the curves are due to interference of radiant energy diffracted and transmitted by a particle, while the rapid fluctuations result from radiant paths which graze the edge of the particle. Note that the Mie scattering efficiency asymptotically approaches a value of 2 for relatively large particle sizes. Thus, geometric optics, which describe scattering mechanisms where the particles are much larger than the wavelength, define a cross sectional area approximately twice that of a spherical particle (from Liou, 1980) within which scattering will occur. Using Eq. 7 to describe the scattering processes within a cloud, it is clear that the effects of cloud droplets, being much larger than their associated CCN, dominate the radiative scattering. The volume scattering coefficient

may typically be as much as 100 times as large for cloud droplets as for the CCN based on their comparative sizes. This fact allows the contribution from CCN scattering to the total cloud reflectance to be ignored.

Reflectance from a cloud for the wavelengths of interest depends upon these Mie scattering mechanisms. The scattering optical depth (δ_s) provides a measure of the scattering based upon the physical depth of the scattering layer (e.g., in this thesis, the stratocumulus cloud thickness) as follows:

$$\delta_s = \int_0^\infty \sigma_s(\lambda) dz. \quad (8)$$

Cloud reflectivity is also a function of the angular variation of scattering for each single scattering event. This variation is the scattering phase function ($P(\psi_s)$) and is used to describe tendencies toward directionally dependent scattering. Mie scattering phase functions are dominant in the forward direction (i.e., more radiance is scattered in the direction of the original ray than in the reverse direction), while Rayleigh scattering is nearly the same forward and back. The properties vary with wavelength and particle/droplet size. In the case of Mie scattering, as the particles or droplets increase in size, more forward scattering occurs. Hunt (1972) illustrates phase function diagrams for size distributions of cloud droplets and ice crystals found in various cloud types, and confirms that a decrease in cloud droplet modal radius results in greater back-scattering of radiation by the droplets. While the reflectance from a cloud is dependent on the nature of single scattering characteristics, it must be remembered that radiant energy from a cloud source at visible wavelengths will have been scattered many times, effectively smoothing out the complex angular patterns observed in single scattering events. In the NIR, the probability of absorption limits the number of individual scattering events so that more of the directional scattering defined by the phase function is maintained.

The ratio of the volume scattering coefficient to the beam attenuation coefficient (σ_s/σ_t) is called the single scattering albedo (ω_0) and describes the probability of scatter for a single interaction between radiant energy and a particle or droplet. The single scattering albedo varies with wavelength and particle/droplet composition.

As illustrated by Hunt (1972), changes in cloud radiative properties for the wavelengths of interest are consistent with changes in cloud droplet size distribution and concentration, and scattering optical depth which is a function of cloud thickness. It

was shown in a previous section that the cloud droplet distribution depends upon the initial distribution of CCN present in the air mass. It follows logically that changes in the reflective properties of clouds may be due to variations in aerosol, CCN distribution. This relationship is illustrated by Twomey and Cocks (1982) and discussed by Coakley *et al.* (1987) and Wetzzel and Vonder Haar (1986). Twomey (1977) observed that in most clouds the injection of an additional source of small CCN will increase the cloud reflectivity. Hansen and Pollack (1970) found that the volume extinction coefficient, the single scattering albedo, the shape of the phase function, and the asymmetry factor (i.e., the first moment of the phase function; in Mie scattering it denotes the relative strength of forward scattering) all depend mainly on cloud droplet modal radius and not on variations in the shape of the size distribution. Cloud reflectance will also increase if its scattering optical depth increases without a compensating gain in absorptivity. Such an effect occurs when there is an increase in EQLWC, although the effect varies with wavelength and cloud thickness as will be discussed in the next section.

b. Spectral Variations

Channel 1 radiance is composed of reflected solar radiation. Stratocumulus clouds in this channel will reflect 10 to 15 times as much radiation than the background ocean surface (discounting sunglint). Channel 3 radiance is composed of a combination of reflected and emitted radiant energy. According to Coakley *et al.* (1987) the scattering cross section of a cloud droplet at this wavelength is approximately proportional to its geometric cross section while the absorption cross section is approximately proportional to its volume. Thus the ratio of scattering to absorption increases as droplet radius decreases. The size dependence on absorption allows the volume absorption coefficient (σ_a) and droplet radius to be related to the single scattering albedo (from Twomey and Cocks (1982) by

$$1 - \omega_0 \propto \sigma_a r. \quad (9)$$

The radiative properties of stratocumulus clouds in channel 3 are sensitive to changes in cloud droplet radius. Coakley and Davies (1986) indicates that the sensitivity of reflectance to droplet size is greatest in channel 3 due to the absorption occurring at this wavelength. The additional scattering in conjunction with a decrease in droplet radii leads to increased cloud reflectivity. Thus, an injection of CCN-rich air into a particular cloud field and the associated increase in droplet concentration would be compensated by a shift toward smaller droplets if the EQLWC remains unchanged. Smaller cloud

droplet distributions show increased reflectance in channel 3 as a result of increased back-scattering, greater Mie scattering efficiency, and the change in the ratio of scattering to absorption. Higher droplet concentrations and increased back-scattering result in greater channel 1 reflectance. In cloud regions where the shift to smaller droplet size distribution is accompanied by a loss of EQLWC and/or optical depth, the increase in channel 3 reflectance remains prevalent while channel 1 reflectance may actually decrease. Arking and Childs (1985) demonstrates the ability to deduce general microphysical model parameters for cloud droplets from the total channel 3 radiance; however, the ability of this technique to resolve precise cloud droplet size distribution information is limited by the variable contribution of thermal emission in this channel. Hunt (1972) and Hansen and Pollack (1970) report values for solar reflectance for both visible and NIR wavelengths. These values show that in channel 1, reflectance is strongly dependent upon cloud thickness and to a lesser degree the EQLWC, the modal radius, and the solar zenith angle. In channel 3 the dependencies on EQLWC and cloud thickness are not as great as the dependence on solar zenith angle and modal radius. The single scattering albedo in channel 3 for stratocumulus cloud droplets has an average value near 0.89; therefore, there is a significant probability for absorption after relatively few scattering events. As a result, these clouds in channel 3 essentially have an infinite optical depth with a cloud thickness of just a few tens of meters. Increases in EQLWC for clouds of sufficient thickness do not affect the scattering optical depth, so there is no associated increase in reflectivity.

Essentially all of the radiant energy in channel 4, and the radiance in channel 3 which is not due to reflection, is emitted thermal radiation. Assuming that stratocumulus clouds are optically thick and reflectance is discounted, the emissivity in channel 3 can be determined by using the brightness temperature obtained from channel 4 measurements and the Planck function. The effects of solar reflection on brightness temperature can be neglected in channel 4 since the emissivity of stratocumulus clouds of applicable optical depth is very close to 1.0. With the contribution from reflectance removed from channel 3, the remainder of the upwelling radiance is thermal emission. As will be seen in Chapter III, clouds other than those which exist in the MABL will be identified utilizing channel 4 brightness temperature so that their more complex absorption, reflection characteristics are not a factor.

c. Anisotropy

Taylor and Stowe (1984) showed that hemispheric reflectance is related to the directional reflectance by the anisotropic reflectance factor (ξ_r) by

$$\rho(\lambda) = \frac{\gamma_r(\lambda, \theta_0, \theta, \phi)}{\xi_r}. \quad (10)$$

The dependence of reflectance on solar zenith angle, satellite zenith angle, and relative azimuth was observed by Ruff and Gruber (1983) by noting the variation in reflectance on an ocean surface at the same geographic point over subsequent satellite orbits. The anisotropic reflectance factors were derived by Taylor and Stowe (1984) from NIMBUS-7 Earth Radiation Budget sensor data and represent spectrally integrated albedo between $0.2\mu\text{m}$ and $50\mu\text{m}$. They are categorized into discrete angular bins, each of which span approximately 12-15 degrees of satellite zenith angle and 10-20 degrees of relative azimuth. These bins are separated into ten categories of solar zenith angle with intervals of 6 to 25 degrees. Factors are listed for eight different surfaces: clear land, snow, ice, ocean, high ice clouds, and high, middle, and low water clouds.

The amount that the anisotropic reflectance factor is different from a value of 1.0 gives the relative importance of the factor in reflectance calculations. For example, a factor of 0.75 indicates that the directional reflectance is less than the isotropic reflectance by 25%. The factors for low water cloud (utilized in this thesis) range from about 0.5 to 2.5 for the range of applicable solar zenith angles (30-70 degrees). In general, low cloud surfaces appear brighter when viewed from overhead than when viewed from an angle near the horizon. The adaptation of anisotropic reflectance to the satellite data processing scheme will be discussed in Chapter III.

C. MODEL REFLECTANCE OF MARINE STRATOCUMULUS CLOUDS

1. Reflectance Calculations

To arrive at theoretical estimates of cloud reflectance, realistic cloud droplet distributions must be generated which represent anticipated conditions in the marine stratocumulus environment. Model cloud droplet distributions are generated using the *modified gamma distribution* (from Deirmendjian, 1969) as follows:

$$n(r) = Ar^2 \exp\left[-\frac{\alpha}{\gamma} (r/r_c)^\gamma\right], \quad (11)$$

where the parameters (A), (α), and (γ) are empirically derived constants. Values of A adjust the amplitude of each cloud droplet size distribution based upon specified modal radius and EQLWC, and do not affect distribution shape. Typical values for these constants are specified by Welch *et al.* (1980) and a summary of those utilized in this thesis are listed in Table 2.

Modal radii (r_c) of $4\mu\text{m}$ and $8\mu\text{m}$ were selected to represent realistic continental and marine air masses, respectively. Two typical levels of EQLWC were selected (0.4 g/m^3 and 0.8 g/m^3) to observe variations in reflectance based on this parameter. Values for the empirical constants were chosen so as to give a typical droplet size distribution for marine stratocumulus clouds near the cloud top. In addition, constants were selected for two other droplet size distributions, one strongly peaked at the modal radius and the other with a broad spread of droplet sizes in order to observe the effect of variations in droplet distribution on the calculated reflectance. The droplet size distribution curves for two combinations of modal radius and EQLWC are shown in Fig. 6.

TABLE 2
MODIFIED GAMMA DISTRIBUTION EMPIRICAL CONSTANTS

$r_c(\mu\text{m})$	EQLWC (g/m^3)	A	α	γ
4.0	0.8	29.7	2.0	1.19
4.0	0.8	6.17	5.0	2.41
4.0	0.8	17.0	5.0	1.30
4.0	0.4	14.9	2.0	1.19
4.0	0.4	3.09	5.0	2.41
4.0	0.4	8.52	5.0	1.30
8.0	0.8	0.465	2.0	1.19
8.0	0.8	0.012	5.0	2.41
8.0	0.8	0.033	5.0	1.30
8.0	0.4	0.232	2.0	1.19
8.0	0.4	0.006	5.0	2.41
8.0	0.4	0.017	5.0	1.30

Using the 12 resultant droplet size distributions, radiance characteristics for each distribution were calculated utilizing Mie code provided by Wiscombe (1980). Tables 3 and 4 list the results for each case. The three combinations of α and γ which describe distribution shape are labeled as:

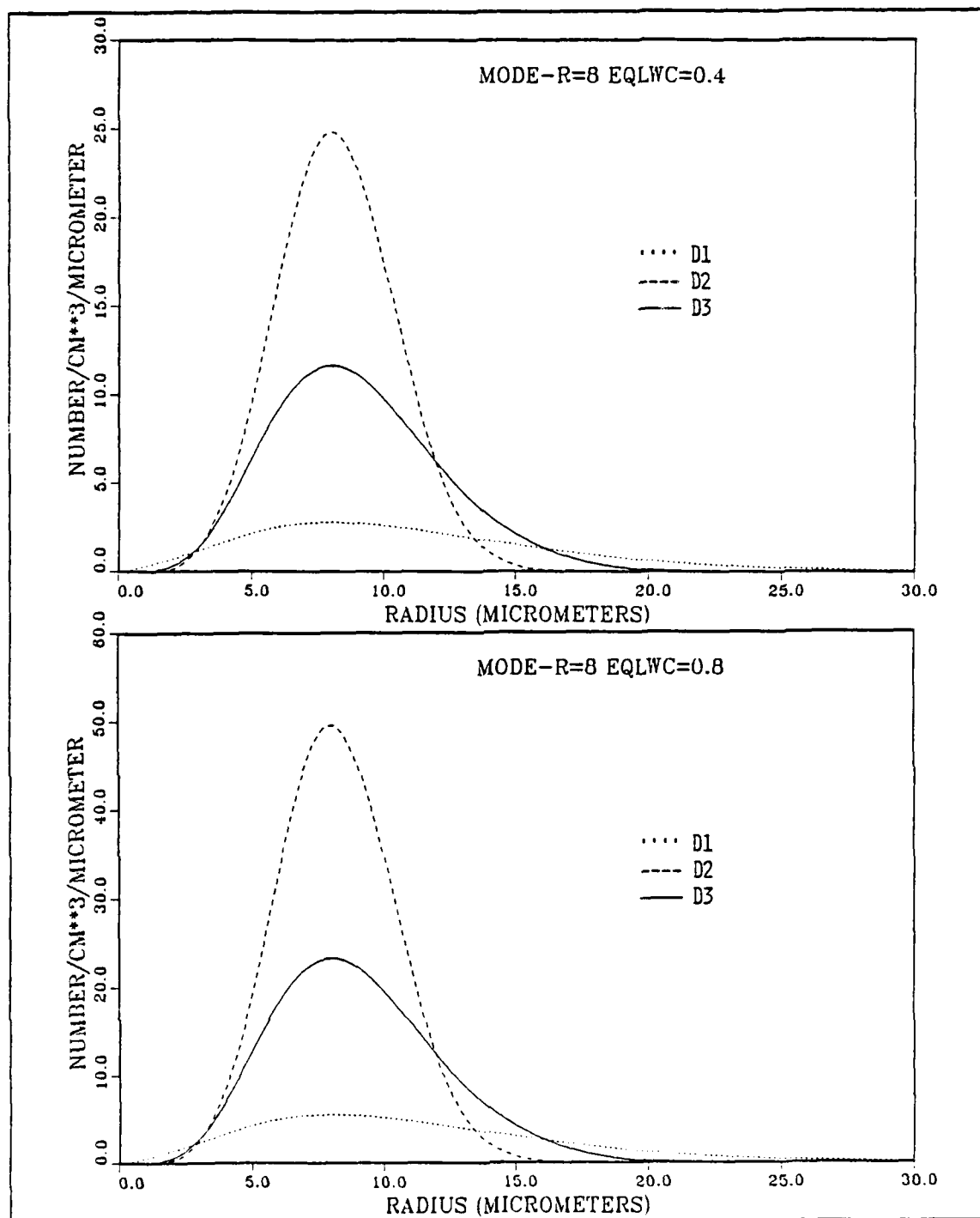


Fig. 6. Model Cloud Droplet Distributions: Modal radius = $8\mu\text{m}$, EQLWC = $0.4\text{g}/\text{m}^3$ (top) and $0.8\text{g}/\text{m}^3$ (bottom). D1, D2, and D3 are the three modified gamma distributions.

TABLE 3
MIE OUTPUT PARAMETERS FOR $0.63\mu m$

Distribution D1 $\Rightarrow \alpha = 2.0 \quad \gamma = 1.19$
 Distribution D2 $\Rightarrow \alpha = 5.0 \quad \gamma = 2.41$
 Distribution D3 $\Rightarrow \alpha = 5.0 \quad \gamma = 1.30$

z (m)	$r_c = 4.0\mu m$ $EQLWC = 0.8g/m^3$			$r_c = 4.0\mu m$ $EQLWC = 0.4g/m^3$			$r_c = 8.0\mu m$ $EQLWC = 0.8g/m^3$			$r_c = 8.0\mu m$ $EQLWC = 0.4g/m^3$		
	D1	D2	D3	D1	D2	D3	D1	D2	D3	D1	D2	D3
Volume Scattering Coefficient (σ_s)												
	0.149	0.277	0.227	0.075	0.138	0.114	0.073	0.134	0.111	0.037	0.067	0.055
Scattering Optical Depth (δ_s)												
750	111.8	207.8	170.3	56.0	103.5	85.5	54.8	100.5	83.3	26.3	50.5	41.6
500	74.5	138.5	113.5	37.3	69.0	57.0	36.5	67.0	55.5	18.3	33.7	27.7
250	37.3	69.3	56.8	18.7	34.5	28.5	18.3	33.5	27.8	9.1	16.8	13.9
100	14.9	27.7	22.7	7.5	13.8	11.4	7.3	13.4	11.1	3.7	6.7	5.5
50	7.5	13.9	11.4	3.7	6.9	5.7	3.7	6.7	5.6	1.8	3.4	2.8
25	4.8	6.9	5.7	1.9	3.5	2.9	1.8	3.4	2.8	0.9	1.7	1.4
10	1.5	2.8	2.3	0.7	1.4	1.1	0.7	1.3	1.1	0.4	0.7	0.6
Single Scattering Albedo (ω_0)												
	1.0	1.0	1.0	1.0	1.0	1.0	1.0	1.0	1.0	1.0	1.0	1.0
Asymmetry Factor (g_r)												
	0.857	0.845	0.849	0.857	0.845	0.849	0.869	0.861	0.864	0.869	0.861	0.864

D1: ($\alpha = 2.0, \gamma = 1.19$),

D2: ($\alpha = 5.0, \gamma = 2.41$), and

D3: ($\alpha = 5.0, \gamma = 1.30$).

The *delta-Eddington* approximation for multiple scattering in clouds (from Joseph *et al.*, 1976) was applied at three representative solar zenith angles (30, 45, and 60 degrees) and cloud thickness ranging from 10 to 750 meters. The resulting reflectance values are listed in Tables 5 and 6.

TABLE 4
MIE OUTPUT PARAMETERS FOR $3.70\mu m$

Distribution D1 $\Rightarrow \alpha = 2.0 \quad \gamma = 1.19$
 Distribution D2 $\Rightarrow \alpha = 5.0 \quad \gamma = 2.41$
 Distribution D3 $\Rightarrow \alpha = 5.0 \quad \gamma = 1.30$

z (m)	$r_c = 4.0\mu m$ $EQLWC = 0.8g/m^3$			$r_c = 4.0\mu m$ $EQLWC = 0.4g/m^3$			$r_c = 8.0\mu m$ $EQLWC = 0.8g/m^3$			$r_c = 8.0\mu m$ $EQLWC = 0.4g/m^3$		
	D1	D2	D3	D1	D2	D3	D1	D2	D3	D1	D2	D3
Volume Scattering Coefficient (σ_v)												
	0.156	0.345	0.259	0.078	0.173	0.129	0.067	0.135	0.108	0.036	0.068	0.054
Scattering Optical Depth (δ_s)												
750	117.0	258.8	194.3	58.6	129.8	96.8	50.2	112.5	81.0	25.0	50.7	40.5
500	78.0	172.5	129.5	39.1	86.5	64.5	33.5	67.5	54.0	16.8	33.8	27.0
250	39.0	86.3	64.8	19.5	43.3	32.3	16.7	33.8	27.0	8.4	16.9	13.5
100	15.6	34.5	25.9	7.8	17.3	12.9	6.7	13.5	10.8	3.4	6.8	5.4
50	7.8	17.3	13.0	3.9	8.7	6.5	3.4	6.8	5.4	1.7	3.4	2.7
25	3.9	8.6	6.5	1.9	4.3	3.2	1.7	3.4	2.7	0.8	1.7	1.3
10	1.6	3.5	2.6	0.8	1.7	1.3	0.7	1.4	1.1	0.3	0.7	0.5
Single Scattering Albedo (ω_0)												
	0.911	0.954	0.940	0.911	0.954	0.940	0.845	0.899	0.883	0.845	0.899	0.883
Asymmetry Factor (g_r)												
	0.783	0.755	0.750	0.783	0.755	0.750	0.845	0.801	0.817	0.845	0.801	0.817

2. Reflectance Variability

Fig. 7 through 9 illustrate the dependency of reflectance on cloud droplet size distribution, EQLWC, and cloud thickness for the center wavelength of AVHRR channels 1 and 3 based on delta-Eddington calculations. The expected increase in reflectance for droplet distributions of smaller modal radius is shown in Fig. 7. The trends in reflectance support the connection of higher reflectances in both channels from clouds under the influence of higher CCN concentrations when the EQLWC and cloud thickness remains unchanged. Fig. 8 reveals the increase in channel 1 reflectance with increasing EQLWC while the channel 3 reflectance remains constant. The change in EQLWC at a constant modal radius changes the scattering optical depth of the cloud in

channel 1 and the related reflectance is modified. In contrast, the absorption by liquid water in channel 3 causes the scattering optical depth to appear infinite in clouds of appreciable thickness. At cloud thicknesses of approximately 50-100 meters or less, decreases in EQLWC and the associated loss in optical depth begin to dominate microphysical effects. The channel 3 reflectance ceases to be independent of changes in EQLWC for these cases. Fig. 9 shows reflectance dependence on cloud thickness. Channel 1 reflectances rise sharply in the first few hundred meters and then asymptotically approach a value of 1.0 with increasing cloud thickness. Channel 3 reflectances rise quickly at small cloud thicknesses and then remain constant beyond this initial rise. At the point where the reflectance becomes constant with increasing thickness, incident radiant energy has reached the deepest point in the cloud layer where it still may be scattered back out the cloud top. When channel 3 is analyzed, it must be remembered that the source of reflected radiant energy is confined to the upper-most regions of the cloud layer (approximately the top 50-100 meters). Also, reflectance variations in channel 3 will not display the large deviations expected in channel 1 which result from the complex changes in scattering optical depth over a finite horizontal distance in a cloud field. For constant EQLWC and solar zenith angle, reflectance variations in channel 3 should be directly attributable to changes in droplet size distribution. Reflectance in both channels increases with increasing solar zenith angle, with dependence on the changing angle greater in channel 3.

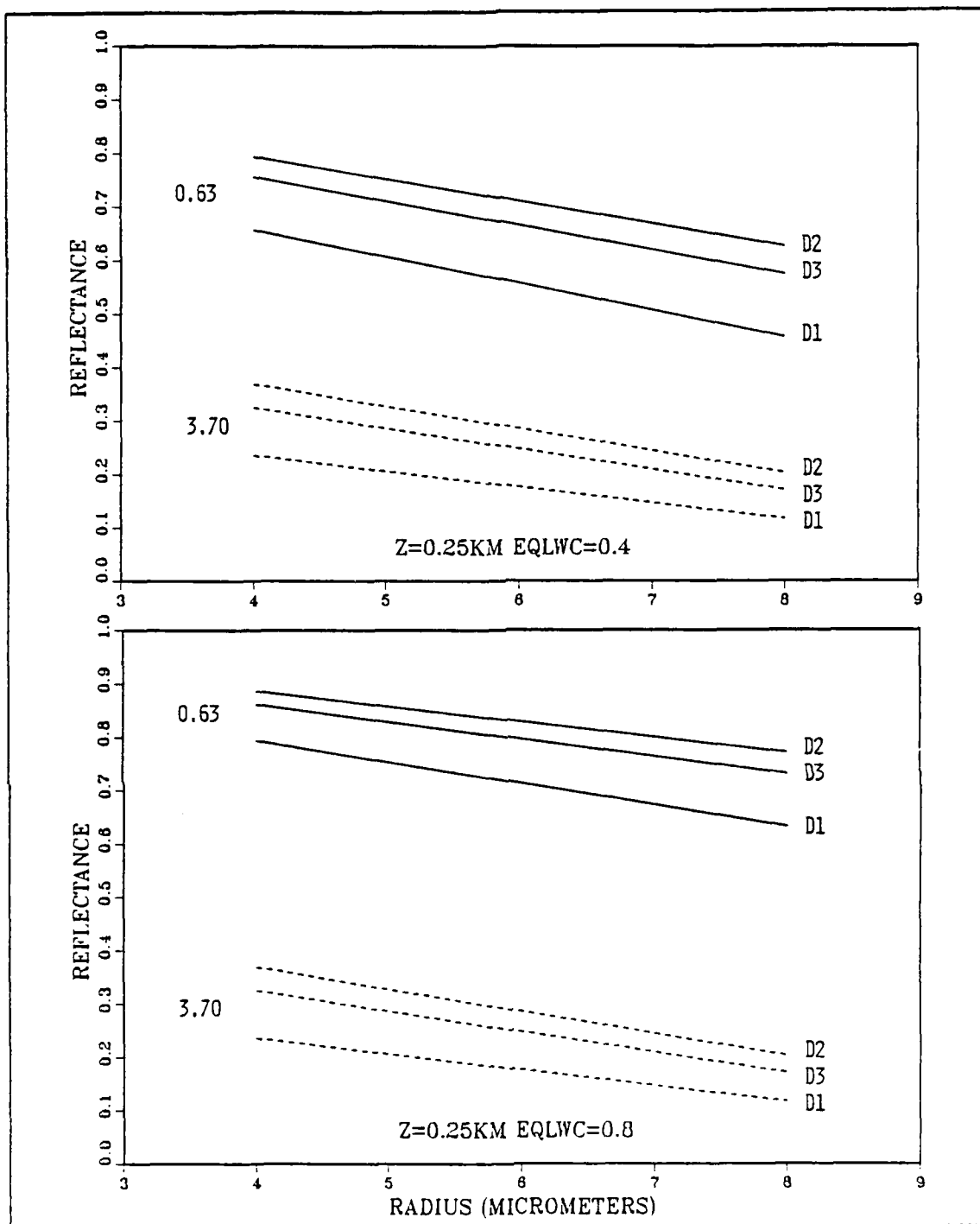


Fig. 7. Reflectance versus Droplet Radius for $z = 0.25$ km: $\theta_0 = 45^\circ$, EQLWC = $0.4g/m^3$ (top) and $0.8g/m^3$ (bottom). D1, D2, and D3 are the three modified gamma distributions.

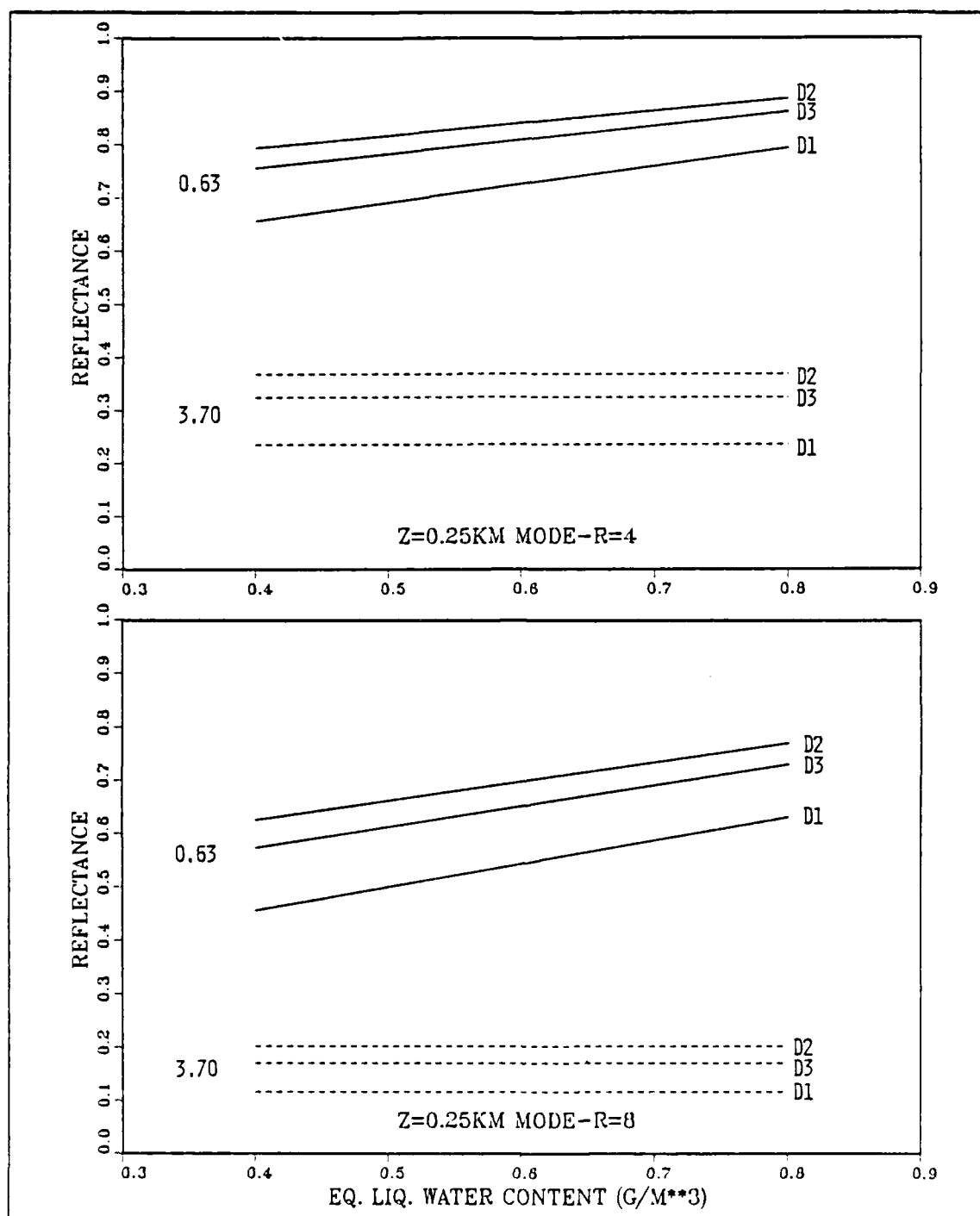


Fig. 8. Reflectance versus EQLWC for $z = 0.25$ km: $\theta_0 = 45^\circ$, modal radius = $4\mu\text{m}$ (top) and $8\mu\text{m}$ (bottom). D1, D2, and D3 are the three modified gamma distributions.

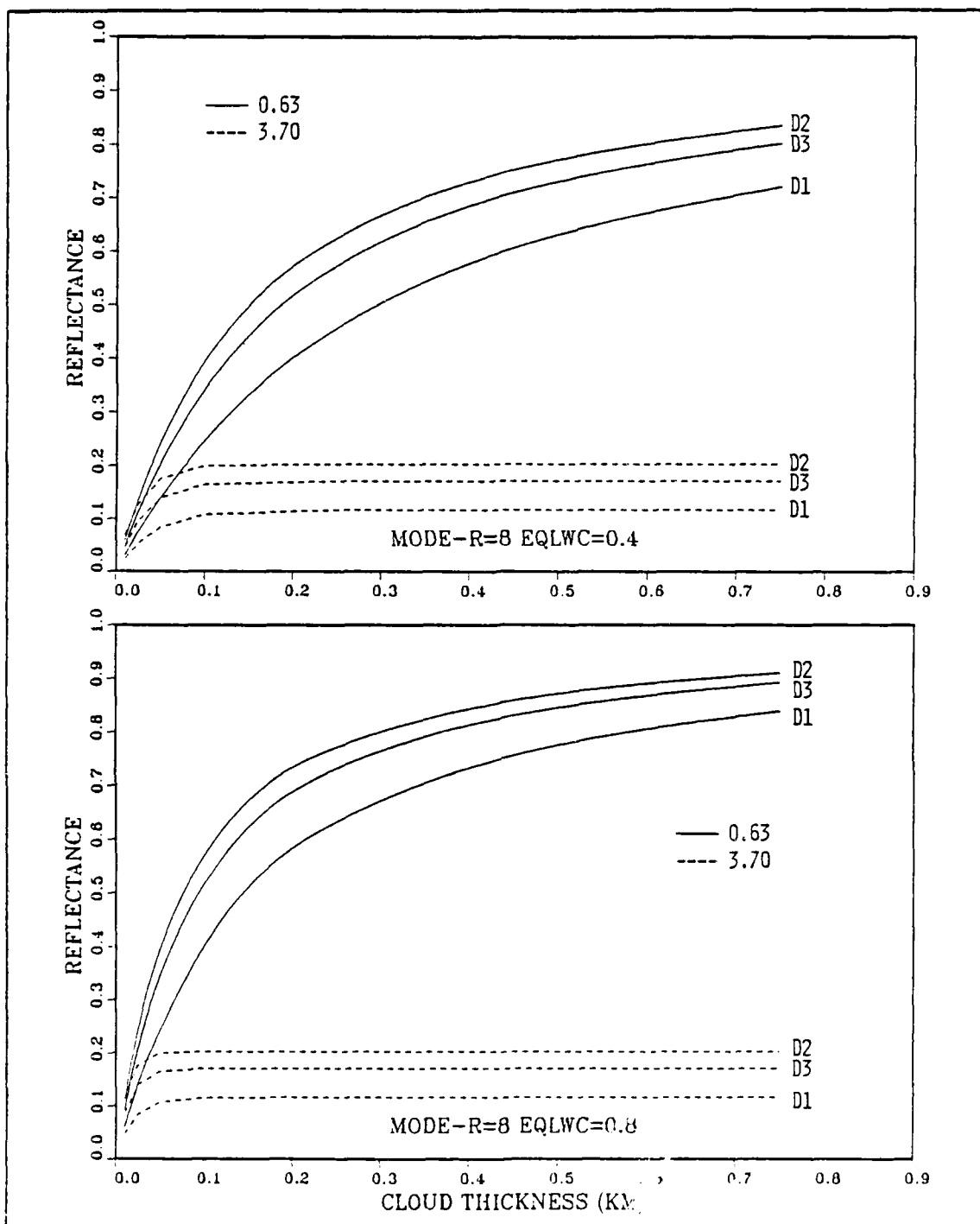


Fig. 9. Reflectance versus Cloud Thickness (z): $\theta_0 = 45^\circ$, modal radius = $8\mu\text{m}$, EQLWC = 0.4g/m^3 (top) and 0.8g/m^3 (bottom). D1, D2, and D3 are the three modified gamma distributions.

TABLE 5
DELTA-EDDINGTON REFLECTANCES FOR $0.63\mu m$

Distribution D1 $\Rightarrow \alpha = 2.0 \quad \gamma = 1.19$

Distribution D2 $\Rightarrow \alpha = 5.0 \quad \gamma = 2.41$

Distribution D3 $\Rightarrow \alpha = 5.0 \quad \gamma = 1.30$

z (m)	$r_c = 4.0\mu m$ $EQLWC = 0.8g/m^3$			$r_c = 4.0\mu m$ $EQLWC = 0.4g/m^3$			$r_c = 8.0\mu m$ $EQLWC = 0.8g/m^3$			$r_c = 8.0\mu m$ $EQLWC = 0.4g/m^3$		
	D1	D2	D3	D1	D2	D3	D1	D2	D3	D1	D2	D3
Reflectances for Solar Zenith Angle (θ_0) = 30°												
750	0.912	0.954	0.943	0.836	0.912	0.892	0.820	0.900	0.879	0.679	0.817	0.781
500	0.872	0.933	0.917	0.770	0.873	0.846	0.749	0.856	0.827	0.589	0.745	0.700
250	0.770	0.873	0.845	0.618	0.771	0.728	0.589	0.744	0.700	0.399	0.583	0.526
100	0.558	0.728	0.678	0.371	0.559	0.500	0.342	0.522	0.464	0.195	0.335	0.283
50	0.371	0.561	0.500	0.211	0.371	0.316	0.195	0.335	0.287	0.100	0.191	0.157
25	0.264	0.371	0.316	0.114	0.216	0.179	0.100	0.191	0.157	0.050	0.100	0.081
10	0.091	0.178	0.145	0.043	0.092	0.071	0.039	0.077	0.064	0.022	0.042	0.035
Reflectances for Solar Zenith Angle (θ_0) = 45°												
750	0.921	0.959	0.949	0.853	0.921	0.904	0.839	0.910	0.892	0.721	0.836	0.803
500	0.885	0.940	0.926	0.794	0.886	0.862	0.775	0.871	0.845	0.632	0.772	0.731
250	0.794	0.886	0.861	0.657	0.794	0.756	0.632	0.771	0.731	0.457	0.626	0.574
100	0.603	0.756	0.711	0.429	0.604	0.550	0.402	0.570	0.517	0.248	0.396	0.344
50	0.430	0.606	0.550	0.269	0.429	0.376	0.243	0.395	0.345	0.140	0.244	0.205
25	0.269	0.430	0.375	0.154	0.327	0.229	0.140	0.243	0.206	0.075	0.137	0.113
10	0.127	0.228	0.190	0.067	0.127	0.105	0.061	0.112	0.093	0.031	0.059	0.048
Reflectances for Solar Zenith Angle (θ_0) = 60°												
750	0.933	0.965	0.957	0.875	0.933	0.918	0.863	0.924	0.908	0.756	0.860	0.833
500	0.903	0.949	0.937	0.825	0.903	0.883	0.809	0.890	0.869	0.687	0.806	0.771
250	0.825	0.903	0.882	0.709	0.825	0.793	0.687	0.805	0.772	0.537	0.682	0.638
100	0.663	0.793	0.755	0.514	0.664	0.618	0.488	0.635	0.589	0.343	0.483	0.435
50	0.514	0.665	0.618	0.361	0.513	0.465	0.343	0.483	0.438	0.212	0.338	0.296
25	0.416	0.513	0.465	0.235	0.366	0.323	0.212	0.338	0.296	0.122	0.213	0.181
10	0.198	0.321	0.278	0.106	0.199	0.162	0.098	0.173	0.149	0.059	0.103	0.080

TABLE 6
DELTA-EDDINGTON REFLECTANCES FOR $3.70\mu m$

Distribution D1 $\Rightarrow \alpha = 2.0 \quad \gamma = 1.19$

Distribution D2 $\Rightarrow \alpha = 5.0 \quad \gamma = 2.41$

Distribution D3 $\Rightarrow \alpha = 5.0 \quad \gamma = 1.30$

z (m)	$r_c = 4.0\mu m$ $EQLWC = 0.8g/m^3$			$r_c = 4.0\mu m$ $EQLWC = 0.4g/m^3$			$r_c = 8.0\mu m$ $EQLWC = 0.8g/m^3$			$r_c = 8.0\mu m$ $EQLWC = 0.4g/m^3$		
	D1	D2	D3	D1	D2	D3	D1	D2	D3	D1	D2	D3
Reflectances for Solar Zenith Angle (θ_0) = 30°												
750	0.199	0.329	0.286	0.199	0.329	0.286	0.091	0.169	0.139	0.091	0.169	0.139
500	0.199	0.329	0.286	0.199	0.329	0.286	0.091	0.169	0.139	0.091	0.169	0.139
250	0.199	0.329	0.286	0.199	0.329	0.286	0.091	0.169	0.139	0.090	0.169	0.139
100	0.199	0.329	0.286	0.196	0.329	0.285	0.090	0.169	0.138	0.081	0.164	0.132
50	0.196	0.329	0.285	0.169	0.316	0.268	0.081	0.164	0.132	0.060	0.138	0.100
25	0.169	0.316	0.268	0.117	0.258	0.208	0.060	0.138	0.106	0.036	0.095	0.069
10	0.104	0.234	0.186	0.060	0.144	0.113	0.032	0.083	0.061	0.016	0.048	0.032
Reflectances for Solar Zenith Angle (θ_0) = 45°												
750	0.236	0.369	0.325	0.236	0.369	0.325	0.117	0.203	0.171	0.117	0.203	0.171
500	0.236	0.369	0.325	0.236	0.369	0.325	0.117	0.203	0.171	0.117	0.203	0.171
250	0.236	0.369	0.325	0.236	0.369	0.325	0.117	0.203	0.171	0.117	0.203	0.171
100	0.236	0.369	0.325	0.233	0.369	0.325	0.116	0.203	0.171	0.108	0.200	0.165
50	0.233	0.369	0.325	0.209	0.358	0.310	0.108	0.200	0.165	0.084	0.176	0.140
25	0.209	0.358	0.310	0.154	0.306	0.254	0.084	0.176	0.140	0.053	0.128	0.096
10	0.139	0.282	0.231	0.085	0.188	0.151	0.048	0.114	0.086	0.024	0.069	0.046
Reflectances for Solar Zenith Angle (θ_0) = 60°												
750	0.292	0.428	0.384	0.292	0.428	0.384	0.160	0.257	0.221	0.160	0.257	0.221
500	0.292	0.428	0.384	0.292	0.428	0.384	0.160	0.257	0.221	0.160	0.257	0.221
250	0.292	0.428	0.384	0.292	0.428	0.384	0.160	0.257	0.221	0.160	0.257	0.221
100	0.292	0.428	0.384	0.289	0.427	0.383	0.159	0.257	0.221	0.153	0.254	0.217
50	0.289	0.427	0.383	0.270	0.419	0.372	0.153	0.254	0.217	0.128	0.235	0.195
25	0.270	0.419	0.372	0.213	0.376	0.325	0.128	0.235	0.195	0.086	0.188	0.147
10	0.202	0.355	0.304	0.134	0.263	0.220	0.079	0.171	0.134	0.041	0.111	0.077

III. DATA ANALYSIS

A. SATELLITE DATA PROCESSING

This section discusses the methods by which the AVHRR satellite data are processed in order to derive the desired reflective and thermal properties and produce the associated images. Processing is performed at the U.S. Naval Postgraduate School's Interactive Digital Environmental Analysis (IDEA) Laboratory. The multichannel analysis routine utilized in this thesis is a FORTRAN software package run on a Digital Equipment Corporation VAX 8250 computer system. The Gould DeAnza image analysis workstation is hosted by a Gould IP8500 image processor and a 9 Mb microVAX-II computer tied to the VAX 8250 system. Each case study analysis in this thesis consists of the channel 1 radiance corrected for anisotropy, channel 3 reflectance corrected for anisotropy, and channel 4 brightness temperature. Each analysis requires approximately 45 minutes processing time (15 minutes for channel 1, 25 for channel 3 and 5 for channel 4). In comparison, processing time for any single raw AVHRR channel takes about 5 minutes. The processing time includes reading the raw IIRPT data from tape, calculating the corrected and scaled pixel values, and generating the image for each channel. A composite image is constructed by overlaying data from the three channels. Each image consists of a 512 by 512 pixel, full resolution subscene located at geographic coordinates specified by an initial satellite overview analysis. Satellite ephemeris data and subscene quality are examined to ensure the effects of sunglint are minimized at specific regions of interest.

1. Channel 1

The measured radiance in channel 1 is calibrated in terms of albedo. The directional reflectance measured by the satellite is converted to isotropic reflectance by weighting each pixel value by the cosine of the solar zenith angle and the anisotropic reflectance factor discussed in Chapter II. The resulting reflectance values are linearly scaled from 20 to 100 percent for pixel values from 0 to 255. This scaling ensures that there is no reflectance contribution from the ocean surface. The scaling also excludes cloudy pixels of minimal scattering optical depth and pixels with an insufficient cloud cover fraction within the field of view, and enhances the contrast between stratocumulus cloud tops of variable reflectance.

Allen (1987) utilized anisotropic reflectance factors in determining reflectance in channels 1 and 3 by selecting the appropriate bin from the data compiled by Taylor and Stowe (1984) that encompassed the satellite zenith angle, solar zenith angle, and relative azimuth for each pixel in a subscene. This created problems at bin boundaries where discontinuities in anisotropic reflectance factors and in the associated images were observed. For channel 1 (and channel 3) in this thesis, these discrete factors are smoothed by entering them into a three-dimensional matrix and applying a moving least-squares fit. The resulting anisotropic reflectance factors are described by basis functions whose polynomial coefficients are the matrix solution vector. The smoothing routine can incorporate the factors designated for the specific surface type being processed, in this case low level water clouds. Utilizing the smoothed anisotropic reflectance factors, resultant isotropic reflectance values are more accurate at bin boundaries by as much as 50 percent of the difference in reflectance between adjacent bins when no smoothing is applied. Discontinuities in the images due to varying anisotropic reflectance factors are eliminated. There is some concern that this polynomial method may become unstable in certain situations; however, no significant instabilities are observed in the analyses contained in this thesis. In addition, variations in anisotropic reflectance as a function of wavelength must be ignored since the values provided by Taylor and Stowe (1984) are spectrally integrated values. The smoothing routine adds approximately four minutes to subscene processing time.

2. Channel 3

Radiance in channel 3, comprised of both reflected and emitted radiant energy, is calibrated in units of $\text{mW}/\text{m}^2\text{-sr-cm}^{-1}$. The thermally emitted portion is removed from the total radiance using a method utilized by Allen (1987). This method uses the brightness temperature from channel 4 to solve for the thermal emission in channel 3. Utilizing Eq. 5, the thermal emission in channel 3 is estimated by solving for the Planck function based upon the channel 4 measured radiance as follows:

$$B(T)_{(CH4)} = \frac{L_{\lambda(CH4)}}{\epsilon_{(CH4)}} \quad (12)$$

The temperature is found by manipulating the Planck function and is used in Eq. 6 to deduce the thermal emission in channel 3. The emittance in channel 3 is related to reflectance by

$$\epsilon_{(CH3)} = 1 - \rho_{(CH3)} \quad (13)$$

The fact that the combination of thermal emission and reflection describes the total radiance in channel 3 and that the emissivity in channel 4 is close to 1.0 increases the validity of the estimation of the emissivity in channel 3. Combining Eq. 5, 10, and 13 reveals:

$$L_{r(CH3)} = B(T)_{(CH3)}[1 - \rho_{(CH3)}] + \xi_r \rho_{(CH3)}[L_{(CH3)} \cos \theta_0]. \quad (14)$$

The reflectance in channel 3 is now available utilizing

$$\rho_{(CH3)} = \frac{L_{r(CH3)} - B(T)_{(CH3)}}{\xi_r [L_{(CH3)} \cos \theta_0] - B(T)_{(CH3)}}, \quad (15)$$

which is the relationship used in the analysis code. The anisotropic reflectance factors in channel 3 are the same smoothed function values used in channel 1 and discussed in the previous section. Reflectance values of 0.0 to 0.45 are scaled to pixel values of 0 to 255 in the analysis. In deriving reflectances from pixel values, a count of 0 in channel 3 is assumed at any pixel where the associated channel 1 reflectance is below 20 percent (i.e., scaled to 0) since the optically thin clouds in these pixels are discounted.

All channel 3 images are slightly degraded by instrument noise internal to the satellite sensor. This noise appears in each image as faint vertical bands of sinusoidally varying amplitude in the horizontal. Since all of the images analyzed in conjunction with this thesis are daytime passes, the effect of the interference is minimized.

3. Channel 4

Radiance values in channel 4 are calibrated in units of $\text{mW}/\text{m}^2\text{-sr-cm}^{-1}$. Corrections provided by Lauritson *et al.* (1979) to convert from radiance to temperature in the NOAA-9/10 AVHRR sensors are incorporated into the processing scheme. A temperature in the range of 200-320 K is assigned to each pixel based on the associated radiance value. The temperature values are used to determine and subtract the contribution of emitted radiance in channel 3 as discussed above. In addition, a threshold temperature of 273.15 K is set for image generation, so pixels that identify below-freezing temperatures are assigned a value of 255 while all others are assigned a value of 0. The resultant image highlights regions where cold clouds above the MABL may be contributing to the radiative characteristics.

4. Composite Images

Upon completion of image generation for each of the three individual channels, a red-green-blue (RGB) composite image is produced by assigning channel 3 reflectance

to red, channel 4 threshold temperature highlighting to green, and channel 1 radiance to blue; and then overlaying the three images. Pixel values from the individual analyses are preserved.

The resultant RGB image may provide a quick, general indication of the nature and variability of possible cloud droplet distribution spectra within the stratocumulus clouds. In regions where the image appears blue, channel 1 radiance is dominating the channel 3 reflectance. The relative reflectance values may be indicating a droplet size distribution composed of relatively large droplets. Color changes to violet and then to red indicate increasing reflectance in channel 3 and/or decreasing reflectance in channel 1. The percentage change in reflectance in channel 1 for stratocumulus cloud fields of significant optical depth is much less than the percentage change observed in channel 3; therefore, changes in channel 1 reflectance (blue) due to variations in optical depth within the stratocumulus cloud field are dominated by changes in channel 3 reflectance (red), possibly due to variations in the microphysical properties of the clouds. Changes from blue to red result from a decrease in channel 1 reflectance due to a loss of optical depth and/or an increase in channel 3 reflectance which may indicate a shift in the droplet size distribution spectra toward smaller droplets. Green or greenish-white areas in the RGB image indicate locations where cold clouds exist. The location of these cold clouds are regions where the scattering mechanisms illustrated in Chapter II become more complex. In addition, these clouds are not found in the MABL along with the stratocumulus clouds upon which the analysis is focused. The highlighted green areas of the composite image allow these areas to be avoided. In addition, the ice cloud masking assists in indicating where cloud shadows are modifying the reflectance in the visible and NIR. The ocean background appears black with the exception of isolated cases of sunglint, where the ocean appears as a homogenous red due to the contribution from channel 3.

The major mechanisms responsible for the variations in droplet size distribution spectra observed throughout the composite images for the case studies in this thesis are discussed in the next chapter.

B. AIRCRAFT DATA

This section describes data acquired by the NCAR Electra for missions coincident with the case studies in this thesis. The aircraft data are processed by NCAR and made available in the form of time-series plots, tabular listings, and one-minute interval histograms on 35 mm microfiche, accompanied by an applicable data quality report.

The data were interpreted using guidelines for standard output data provided by Miller and Friesen (1987). Aircraft instruments and their functions are as follows:

APN-159 Geometric (Radar) Altitude.

Corrected Particle Measuring Systems (PMS)-King Probe EQLWC,

PMS Forward Scattering Spectrometer Probe (FSSP) Mean Cloud Droplet Diameter,

PMS FSSP Cloud Droplet Concentration,

PMS Active Scattering Aerosol Spectrometer Probe (ASASP) Mean Aerosol Diameter, and

PMS ASASP Aerosol Concentration.

All PMS data in this thesis are from one-dimensional probes operated at a sampling rate of one sample per second. Reflectance data used in comparison with aircraft measurements are from NOAA-9/10 overpasses utilized in respective case studies and are sampled along the approximate coordinates of aircraft mission tracks. The PMS data displayed in Chapter IV are from representative positions along the aircraft sampling track, and are interpreted in the context of data in adjacent time intervals in order to reduce the errors in data interpretation caused by instrument noise. It should be noted that, with the exception of the 14 July data, reflectance cross-sections coincident with aircraft data are taken from a single AVHRR swath, resulting in a small difference in azimuth angle between the path of a particular cross-section and the associated aircraft mission leg. Additionally, there may be several hours time difference between aircraft sampling time and satellite overpass. Due to the priority in selecting case study sub-scenes (e.g., avoiding broad areas of sunglint) and the difficulty involved in correlating reflectance and microphysical data sampled at separate times for individual, non-stationary cloud elements, the 18 July subscene encompasses a region north of the aircraft mission track; however, the images show conditions analogous to those along the aircraft mission track where actual reflectance sampling is performed. The PMS ASASP aerosol probe was not mounted on the aircraft during the 29 and 30 June missions.

IV. CASE STUDY RESULTS AND EVALUATION

This chapter describes the four FIRE IFO 1987 case studies utilized in this thesis. Their selection was made based upon the availability of stratocumulus clouds of adequate horizontal extent, sufficient satellite coverage, and coincidence with FIRE aircraft operations. They are delineated as follows:

Case Study 1 (CS1): 28-30 June

Case Study 2 (CS2): 13-14 July

Case Study 3 (CS3): 6 July

Case Study 4 (CS4): 18 July

For each case study, synoptic/mesoscale weather features are identified to locate general advection patterns. Trajectory analyses are included where a more detailed flow description is appropriate. Satellite images are illustrated, and cross-sections of reflectance are provided to assist in describing significant features. The satellite images in this chapter consist of channel 1 and 3 reflectances; refer to the Appendix for associated RGB composite images. Each satellite image contains line segments or rectangles labeled with single capital letters. These line segments identify the location of image cross-sections from which quantitative reflectance data are retrieved and analyzed. Aircraft data from the NCAR Electra are used to relate cloud reflectances obtained from selected image cross-sections to the cloud microphysical properties discussed in Chapter II. All times are given in universal time coordinates (UTC).

A. FIRE IFO 1987 CASE STUDIES

1. CS1 (28-30 June)

a. Synoptic Summary

The conditions off the west coast of the U.S. for the week preceeding CS1 are dominated by offshore flow over the Pacific Northwest as a result of an inland incursion of the subtropical high. These conditions evolve toward a more climatological northwesterly flow during CS1. On 28 June, the subtropical high extends into southern Alaska and is centered at 44°N 139°W. Weak flow exists at 500 mb over the operating area. A weak trough at 500 mb forms over the northern California coast on the 29th, with an associated weak (1009 mb) surface trough appearing as an extension of the persistent thermal low, as shown in Fig. 10. This upper-level trough intensifies on 30

June and moves to a position centered at 35°N 128°W, revealed in Fig. 11. The center of the subtropical high shifts westward to 150°W, with an accompanying ridge extending towards Baja California. The surface trough merges with inland thermal troughing and extends to Oregon. The combination of subtropical high and thermal low maintained westerly to northwesterly surface winds in the operating area over the period. The San Nicolas Island rawinsonde soundings shown in Fig. 12 illustrate the maintenance of a strong subsidence inversion at the top of the MABL and the associated dry air at middle and high levels.

Observing the synoptic history for this period, it is obvious that there must be some offshore influence on the MABL due to continental air. This is confirmed by the NORAPS trajectory analyses displayed in Figs. 13 and 14. The 925 and 850 mb trajectories near northern California and Oregon continue to reflect offshore flow, even though the ridge driving the offshore flow is much weaker than during the previous week. The trajectories for 30 June, shown in Figs. 15 and 16, reflect the weakening of the offshore flow regime. They also suggest that the continentally influenced air which exists over the ocean is being advected south and east as the low-level winds become more westerly over the southern portion of the operating area.

The trajectory data in CS1 (and CS2) are representative of the lowest layers in the NORAPS model. Nearly all of the trajectories reflect subsidence as a result of the influence of the subtropical high to the west of the operating area. Since the pressure changes for intermediate trajectory locations include the effect of the forecast model levels changing with time, no attempt is made to trace the vertical position of the air parcels. The pressure level given in the applicable figures corresponds to the 24-hour forecast position. The trajectory data are also compared to synoptic analyses corresponding to the NORAPS 24-hour forecast period to ensure that NORAPS forecasts verify with actual synoptic conditions. The NORAPS forecasts are considered valid if forecast winds are in reasonable agreement with verification analyses.

b. AVHRR Subscenes

The satellite subscenes utilized in the CS1 analysis are listed in Table 7. The coordinates for each subscene were selected during processing in an attempt to highlight cloud microphysical gradients, encompass NCAR Electra sampling legs where applicable, and avoid sunglint.

Figs. 17 and 18 illustrate channel 1 and channel 3 reflectance for the 28 June NOAA-10 satellite subscene. The visible image reveals a broad, relatively homogenous

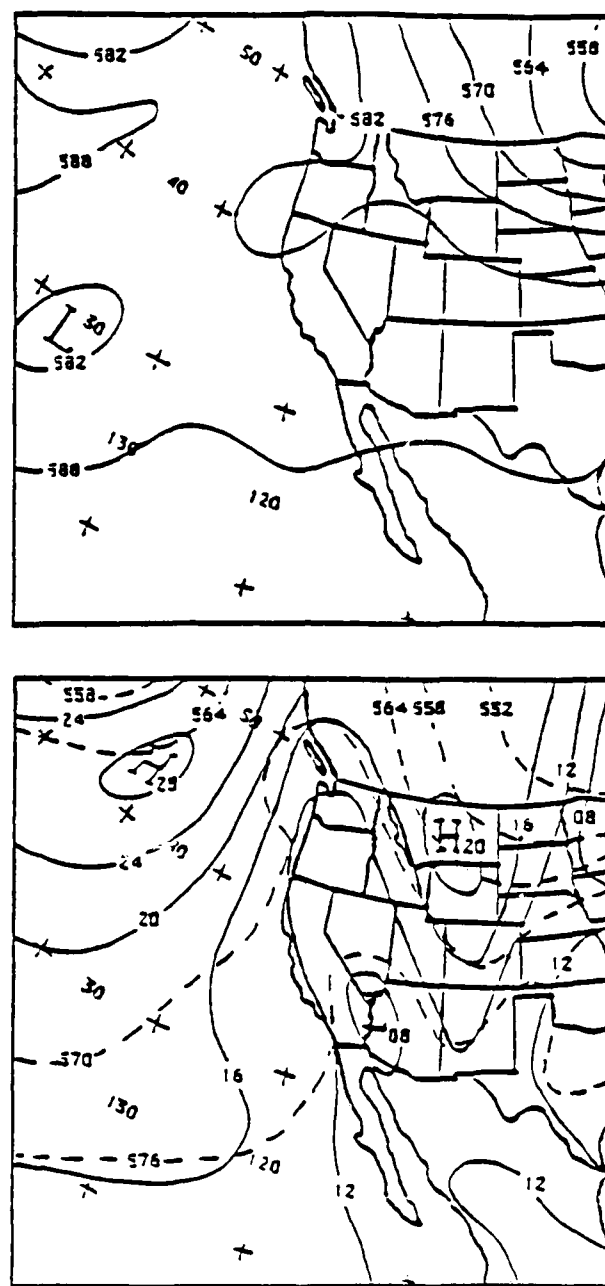


Fig. 10. 29 June 1987 12 UTC Regional OI Analysis: 500 mb heights (top) and surface pressure/1000-500 mb thickness (bottom).

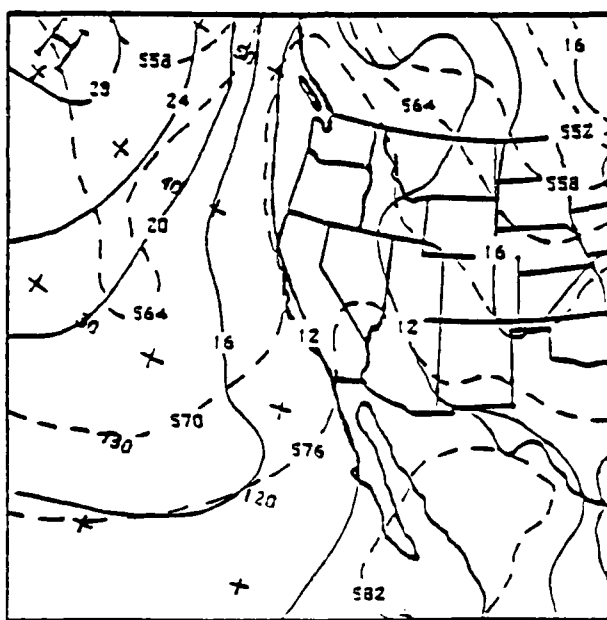
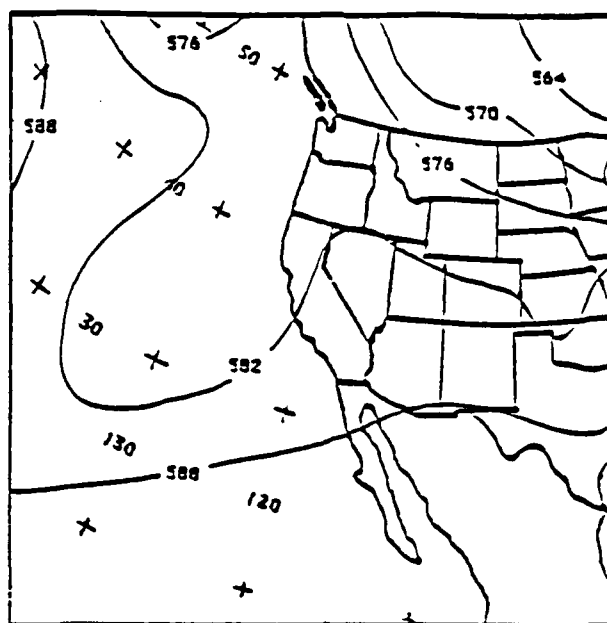


Fig. 11. 30 June 1987 12 UTC Regional OI Analysis: 500 mb heights (top) and surface pressure/1000-500 mb thickness (bottom).

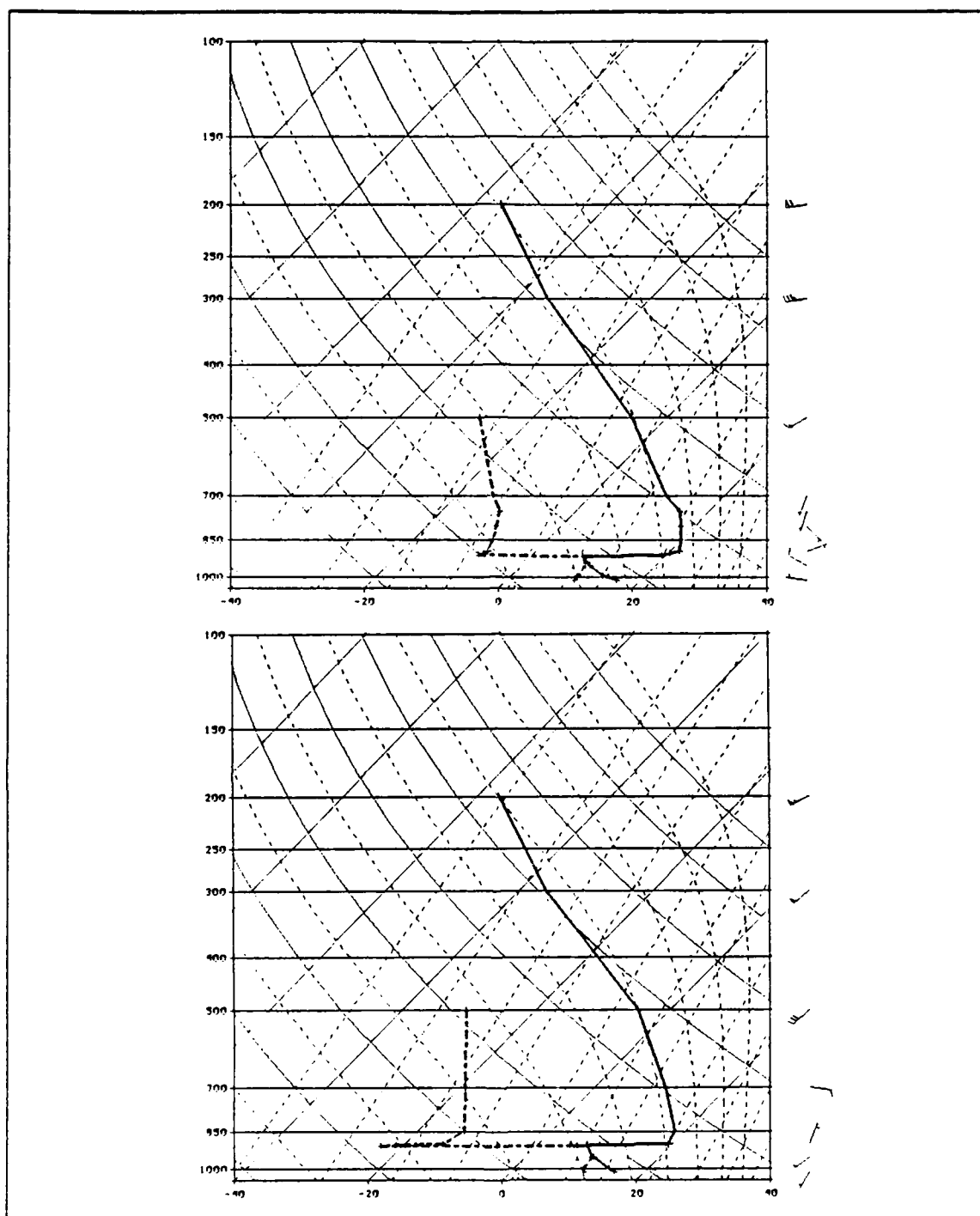


Fig. 12. San Nicolas Island Rawinsonde Sounding: 29 June 1987 1601 UTC (top) and 30 June 1987 1345 UTC (bottom).

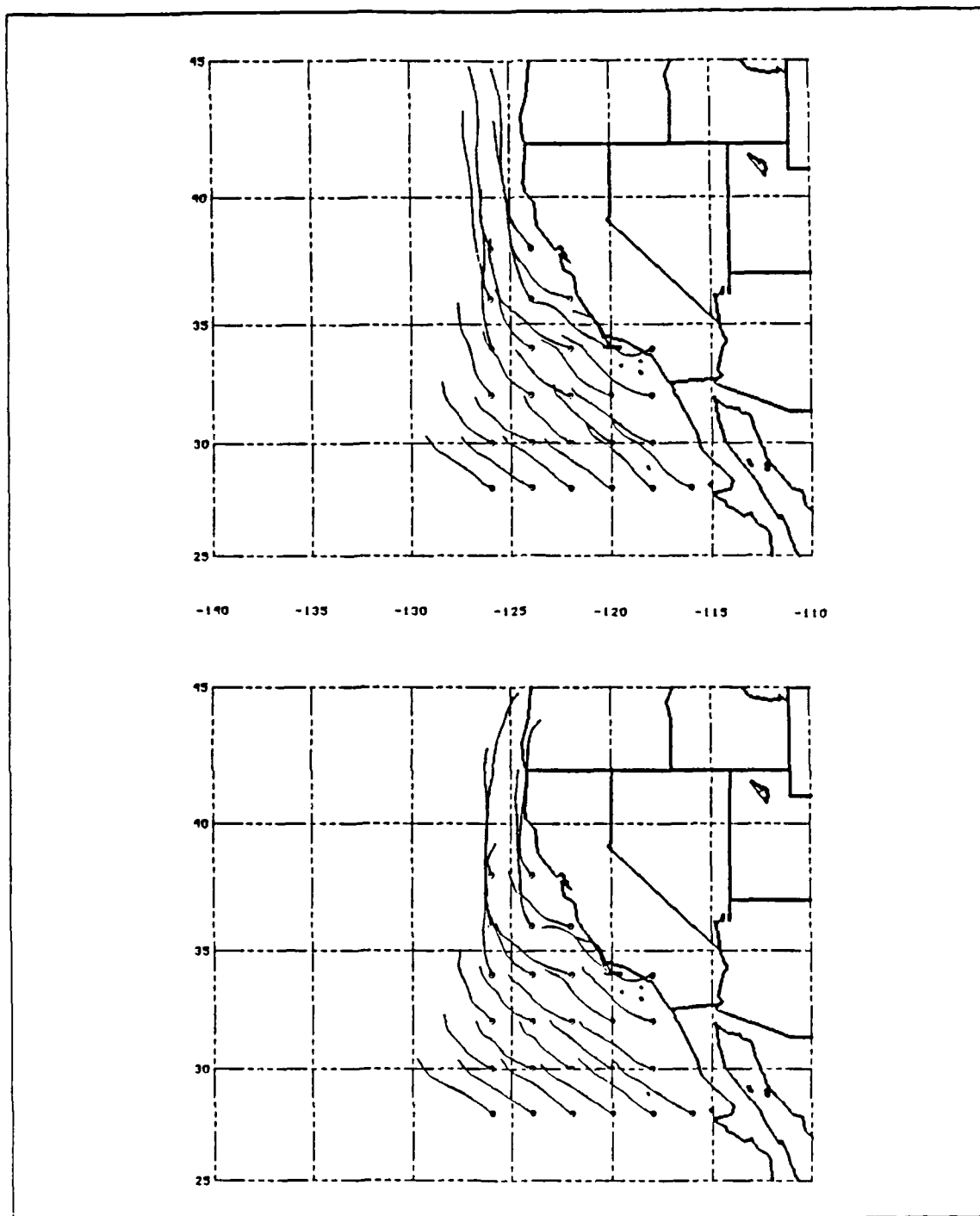


Fig. 13. NORAPS 29 June 1987 00-24 UTC Parcel Trajectories: 1000 mb pressure at 24 UTC (top) and 925 mb pressure at 24 UTC (bottom), circle indicates 24 UTC position.

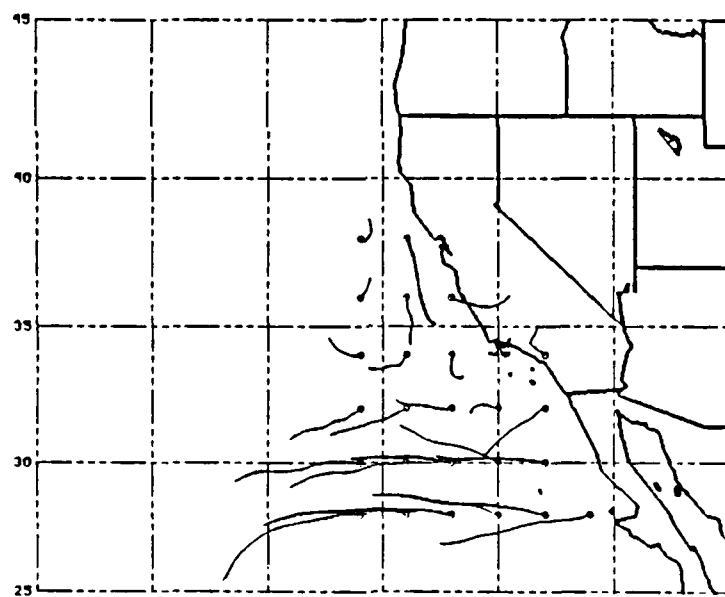
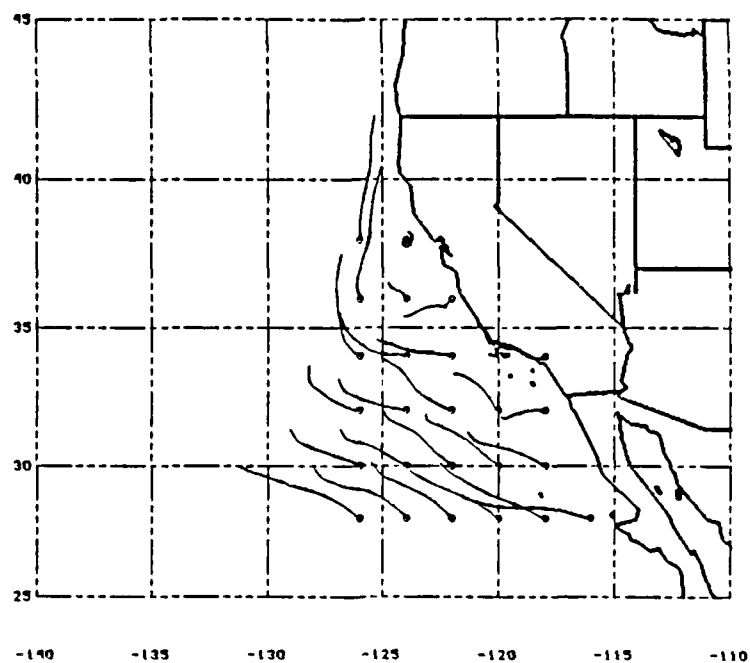


Fig. 14. NORAPS 29 June 1987 00-24 UTC Parcel Trajectories: 850 mb pressure at 24 UTC (top) and 700 mb pressure at 24 UTC (bottom), circle indicates 24 UTC position.

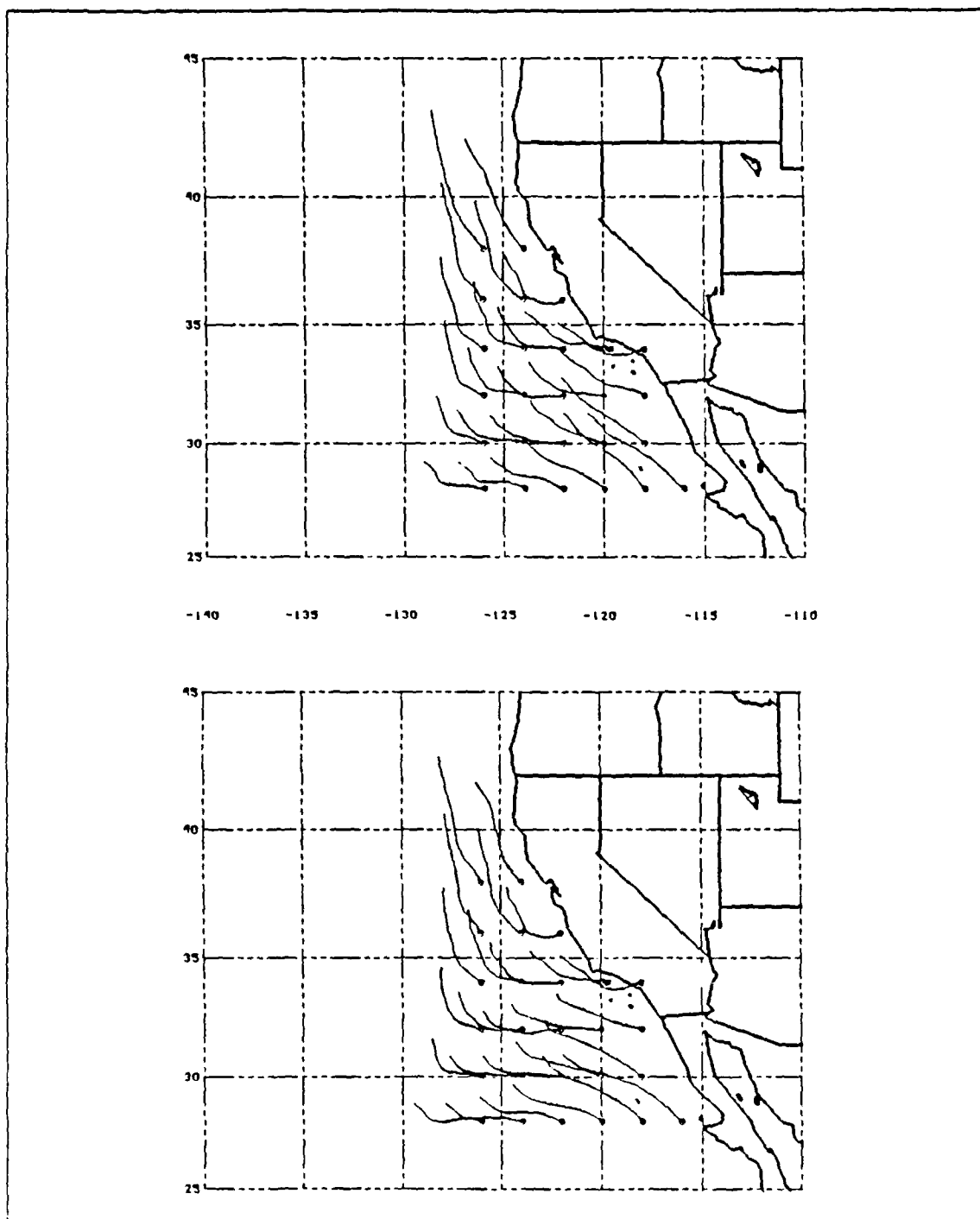


Fig. 15. NORAPS 30 June 1987 00-24 UTC Parcel Trajectories: 1000 mb pressure at 24 UTC (top) and 925 mb pressure at 24 UTC (bottom), circle indicates 24 UTC position.

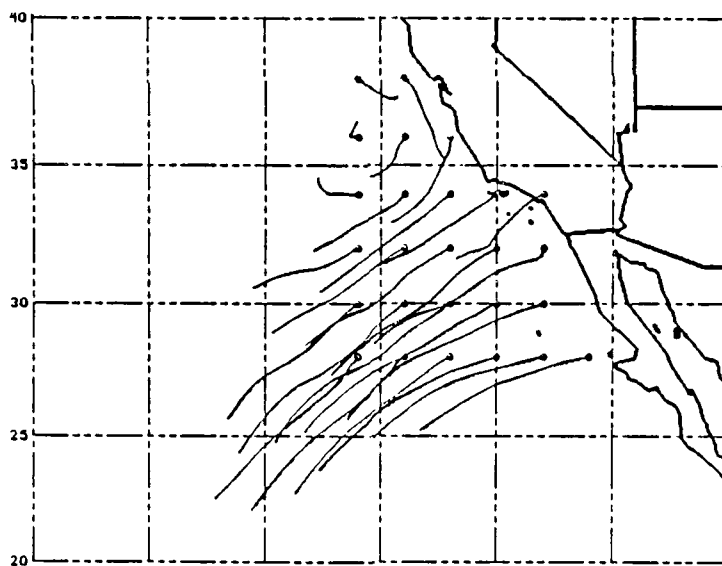
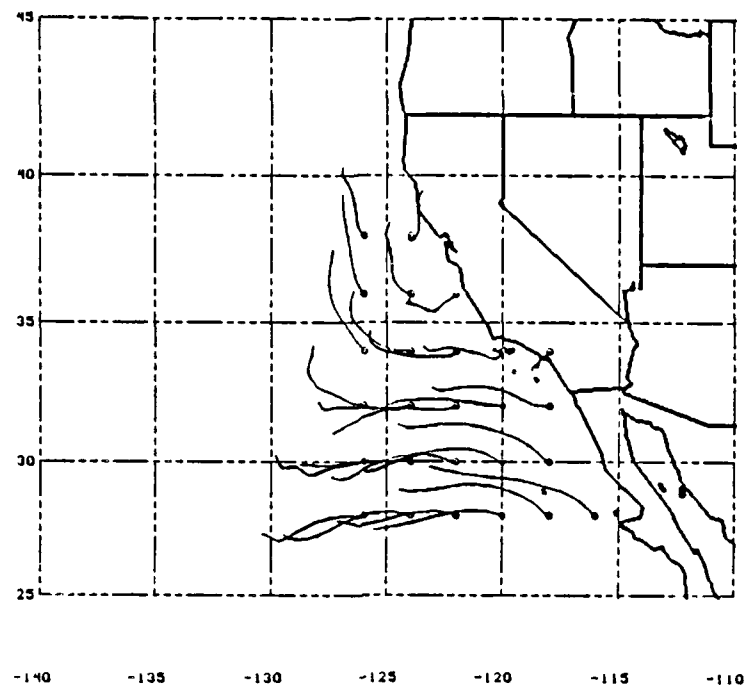


Fig. 16. NORAPS 30 June 1987 00-24 UTC Parcel Trajectories: 850 mb pressure at 24 UTC (top) and 700 mb pressure at 24 UTC (bottom), circle indicates 24 UTC position.

stratocumulus cloud field over the southwestern half of the subscene. To the northwest of subscene center, a band of solid stratocumulus is followed by a band of widely scattered cumulus. Finally, the northwest corner of the subscene is encompassed by another solid stratocumulus field.

The channel 3 image reveals several features consistent with changes in cloud droplet size distribution within the various cloud fields. There is a marked boundary from southwest to northeast which appears to define the extent of the continental air mass influence. Based on the reflectance differences illustrated in Chapter II, the continental region should appear significantly brighter than the marine regime. The stratocumulus in the immediate vicinity of the coast, as well as the stratus which appears inland over the Salinas valley, is heavily influenced by continental CCN and has the brightest reflectance in the image. In addition, a ship track appears in the upper left portion of the image (coincident with cross-section C). These tracks, as discussed in detail by Coakley *et al.* (1987), may be the result of the injection of CCN-rich ship stack exhaust into the cloud layer. The additional CCN modify the cloud droplet size distribution, creating a much higher concentration of smaller droplets. As the CCN and modified droplets are mixed to the upper levels of the cloud layer, these regions can be identified by observing the higher reflectance in channel 3. Actually, the reflectance in channel 1 also increases (as first reported by Coakley *et al.* (1987) and shown in the delta-Eddington model cloud reflectances), but the effect is usually masked by optical depth variations in the vicinity of the ship track resulting from EQLWC and cloud thickness variations.

TABLE 7
CSI SATELLITE SUBSCENES

DATE	PLATFORM	LATITUDE 35°N CROSSING TIME	SUBSCENE CENTER COORDINATES	FIGURE
28 June	NOAA-10	16:38:50 UTC	34°31.1'N 123°42.6'W	17-18
29 June	NOAA-9	22:29:40 UTC	31°26.0'N 124°0.7'W	19-20
30 June	NOAA-10	15:54:55 UTC	31°54.7'N 120°42.4'W	21-22

Figs. 19 and 20 show channel 1 and channel 3 reflectance, respectively, for the 29 June NOAA-9 overpass. The location is near the western edge of the satellite's field of view, causing the resolution of the image on the west edge to be degraded. The



Fig. 17. NOAA-10 AVHRR 1639 UTC 28 June 1987 Channel 1: Line segments indicate reflectance cross-sections A, B, and C. Center coordinates 34°31.1'N 123°42.6'W.



Fig. 18. NOAA-10 AVHRR 1639 UTC 28 June 1987 Channel 3
Reflectance: Line segments indicate reflectance cross-sections A, B, and
C. Center coordinates $34^{\circ}31.1'N$ $123^{\circ}42.6'W$.



Fig. 19. NOAA-9 AVHRR 2230 UTC 29 June 1987 Channel 1: Line segments indicate reflectance cross-sections D and E. Center coordinates $31^{\circ}26.0'N$ $124^{\circ}0.7'W$.

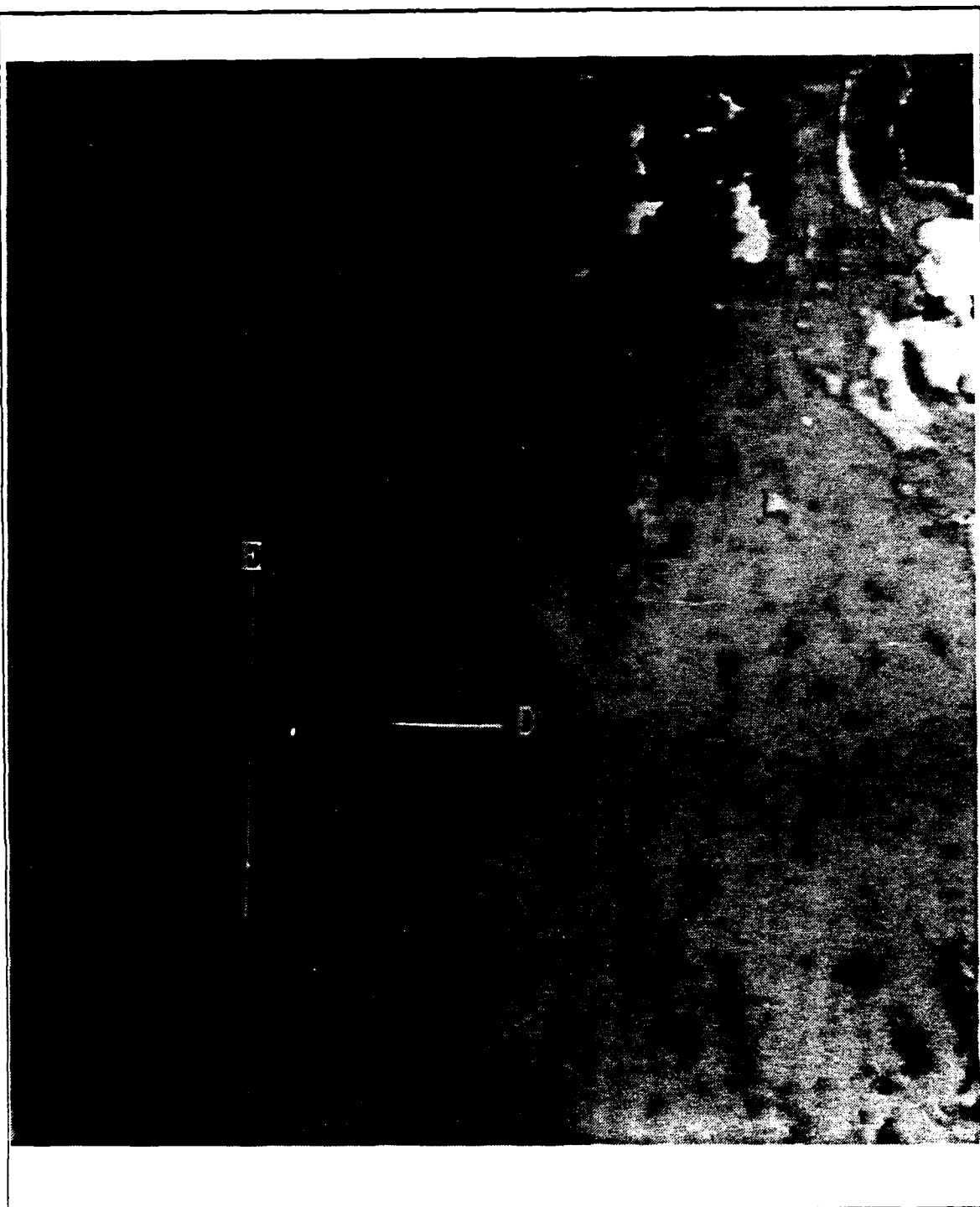


Fig. 20. NOAA-9 AVHRR 2230 UTC 29 June 1987 Channel 3 Reflectance: Line segments indicate reflectance cross-sections D and E. Center coordinates $31^{\circ}26.0'N$ $124^{\circ}0.7'W$.



Fig. 21. NOAA-10 AVHRR 1555 UTC 30 June 1987 Channel 1: Line segments indicate reflectance cross-sections F, G, and H. Center coordinates $31^{\circ}54.7'N$ $120^{\circ}42.4'W$.

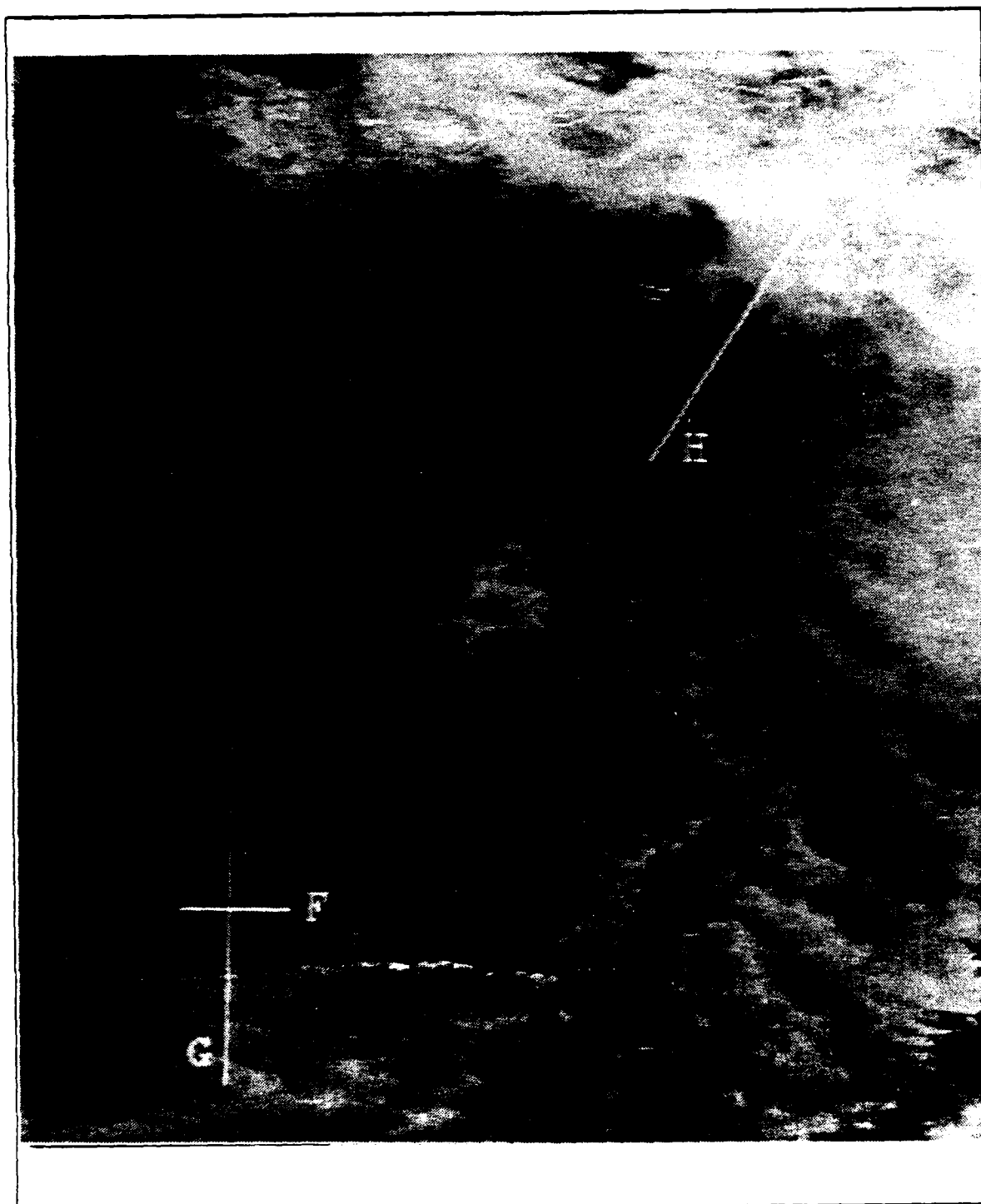


Fig. 22. NOAA-10 AVHRR 1555 UTC 30 June 1987 Channel 3
Reflectance: Line segments indicate reflectance cross-sections F, G, and
H. Center coordinates $31^{\circ}54.7'N$ $120^{\circ}42.4'W$.

channel 1 image reveals that the subscene is mostly dominated by scattered and broken, optically thin stratocumulus clouds. The clouds appear slightly more broken in this image since some of the optically thin clouds and partially cloudy pixels of a reflectance less than 20 percent are scaled to zero by the processing technique. However, there are large clear areas in the southwest portion of the subscene. The northwest corner of the image shows an encroaching stratocumulus field of a more homogenous nature. Point Conception is visible in the upper right.

The brightness contrast in the channel 3 image, in conjunction with the continental/marine interface observed in the 28 June subscene, continues to be apparent. The boundary extends from the left center of the subscene through the center and up to the northeast corner. The shift from marine to continental regime is associated with an increase in the density of cloud coverage. The bright areas south and west of Point Conception are the result of sunglint from the ocean surface.

Images for the 30 June NOAA-10 overpass appear in Figs. 21 and 22. Channel 1 reveals extensive stratocumulus cloud coverage, becoming more broken towards the northwest. The cloud field in the northeast corner has been modified by offshore flow into complex variations of optical depth. The offshore flow is a combination of northwesterly flow east of Point Conception, and the morning extent of the land breeze off the Los Angeles basin. The numerous dark spots over the southeast portion of the image are due to cirrus shadows (these can be categorized by reviewing the composite image for 30 June (Fig. 78) in the Appendix).

The continental/marine boundary is still apparent in the channel 3 image for 30 June. Again, the boundary is also associated with a shift towards more dense cloud coverage in the continental air. As expected, the region under the influence of offshore flow, being rich in continental CCN, shows considerable reflectance at this wavelength. The bright spots in the extreme northeast corner of the subscene are over the Los Angeles basin and are most likely due to industrial sources of CCN in convective plumes being mixed to the top of the cloud layer. Another interesting feature in the marine regime are the thin bands of higher reflectivity around individual cloud cells. This suggests support for the interpretations made by Coakley and Davies (1986) that increased channel 3 reflectivity at cloud edges should be expected from the decrease in EQLWC and cloud droplet size distribution at the cloud edge where the greatest entrainment of sub-saturated ambient air is occurring. This effect is discussed in CS4 where it is the focus of the case study.

Fig. 23 shows the progression of the continental/marine interface over the 3-day period constituting CS1 as determined from satellite data. The geographic shift in the boundary is consistent in direction with the NORAPS trajectories; however, the interface advects at a slightly slower rate than the wind field suggesting that continental aerosol is being freely mixed into the encroaching marine air. This also supports the conclusion of Hindman *et al.* (1977) that an increase in the concentration of marine CCN will not significantly affect the cloud droplet size distribution if a sufficient quantity of small (i.e., continental) CCN remain in the region. The additional possibility that some continental aerosols may be entrained into the MABL from above the subsidence inversion through turbulent processes cannot be discounted.

c. Reflectance Cross-Sections

Channel 1 and 3 reflectance values for cross-sections A and B are displayed in Fig. 24. The pixel-to-pixel variability in channel 1 is expected due to the dependence of reflectivity in this channel to variations in cloud thickness. There is a general decreasing trend in channel 1 reflectance values towards continentally influenced air, from approximately 0.95 to 0.75 over the 150 pixel section. This effect is the opposite of that expected solely due to changes in cloud droplet size distribution. A trend towards decreasing EQLWC and/or cloud thickness in the continental regime must exist to account for the reflectance variation in channel 1.

The channel 3 reflectance values increase from the marine to the continentally influenced air, from 0.1 to 0.17 for cross-section A and from 0.1 to 0.23 for cross-section B, consistent with the anticipated shift to smaller cloud droplet sizes. Most of the change in reflectance occurs over a 50 pixel span. Based upon model reflectances, a change in cloud droplet modal radius of about 2 to 3 μm exists across the continental/marine interface.

Cross-section C, shown in Fig. 25, highlights the reflective properties of a ship track. The track is not detectable in channel 1 due to the brightness of the surrounding stratocumulus cloud field. In channel 3 there is a well-defined increase in reflectance, from an ambient value of approximately 0.10 to a peak value of 0.145 at the twelfth pixel. Coakley *et al.* (1987) report differences in total channel 3 radiance (including the emitted portion) of 0.05 to 0.15 $\text{mW} \cdot \text{m}^2 \cdot \text{sr} \cdot \text{cm}^{-1}$. Assuming no variability in emission, these values are consistent with those observed in CS1 (as well as the other case studies in this thesis). This difference represents a decrease in cloud droplet size distribution modal radius of about 1.5 μm based on model cloud reflectance relationships.

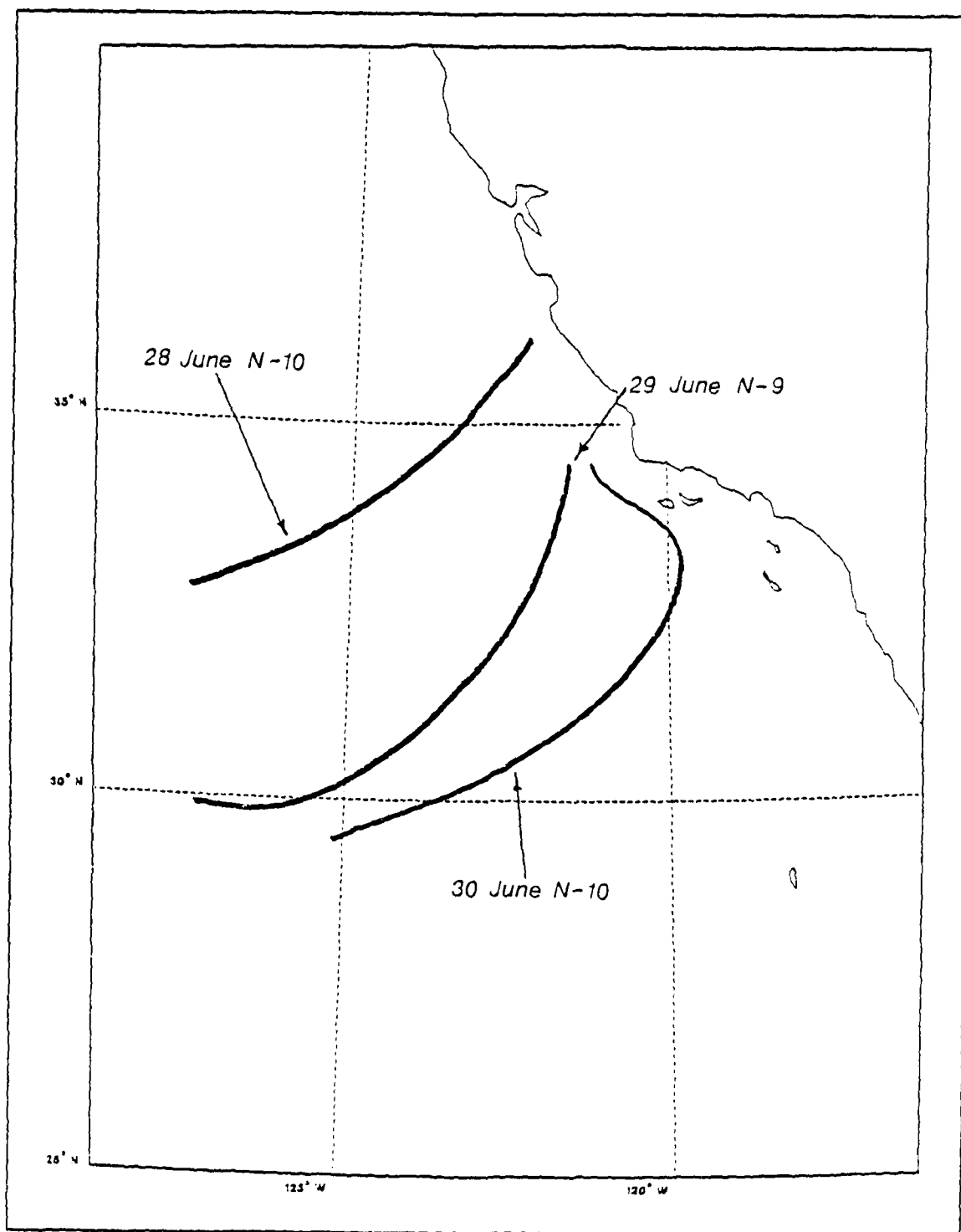


Fig. 23. CS1 Continental/Marine Air Mass Interface: Identified utilizing channel 3 reflectance from CS1 subscenes.

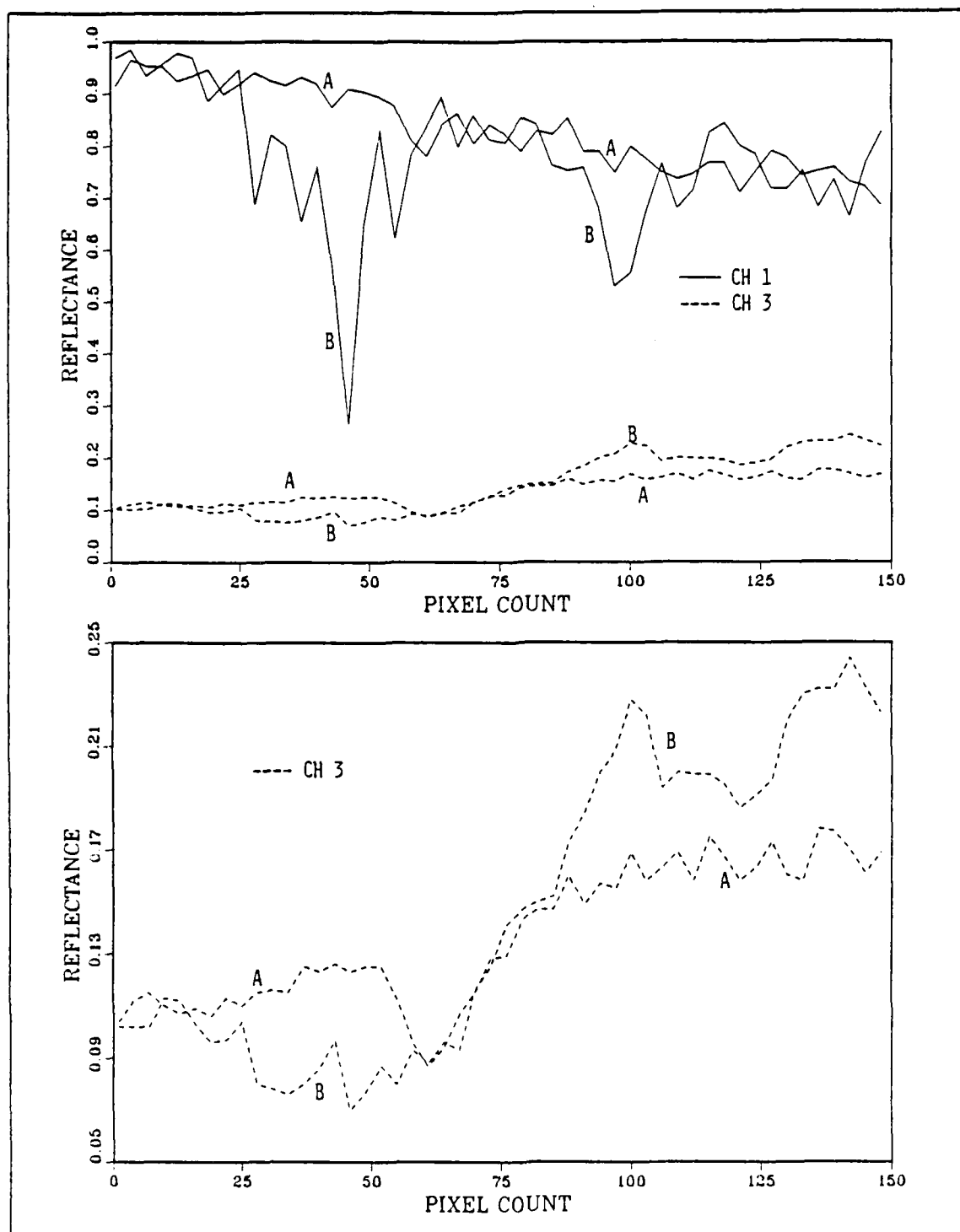


Fig. 24. Reflectance Cross-Sections A and B: Cross-section A sampled west to east; B sampled north to south.

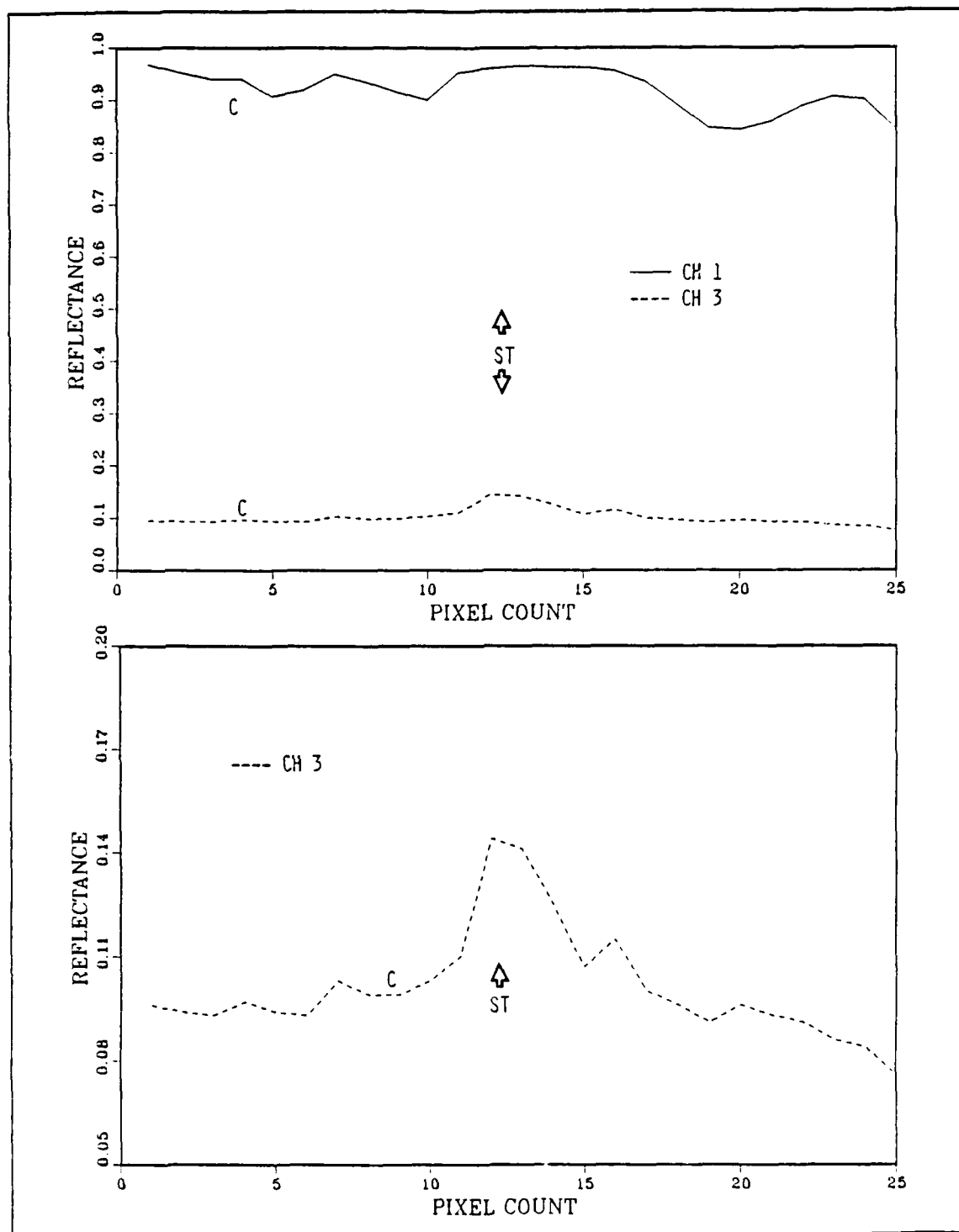


Fig. 25. Reflectance Cross-Section C: Sampled north to south; ST denotes position of ship track.

Cross-section D, displayed in Fig. 26, is coincident with the region of the NCAR Electra mission of 29 June. The relatively thin cloud field seen in the satellite subscene is reflected in the lower channel 1 reflectance values along the sampled path (0.33 average). Channel 3 reflectance increases slightly, from an average of 0.15 to 0.17. This variation seems to indicate that, with decreasing distance to the landmass, there are increases in continental CCN within the air mass, but the weaker droplet size distribution gradient makes this variance less noticeable than the obvious continental/marine air mass interface just to the northwest of the cross-section. Another interesting feature is the channel 3 reflectance decrease associated with peaks in the channel 1 reflectance. This may be due to the fact that the peaks in channel 1 indicate the center of stratocumulus cloud cells. Values of EQLWC at cloud cell centers are higher than the values found near cloud edges where subsidence and entrainment mix sub-saturated air into the cloud from the overlying inversion. This mechanism changes the horizontal spectrum of cloud droplet sizes in the upper 50-100 meters of the cloud (which is the layer affecting the channel 3 reflectance) and creates the effect observed in the figure. This observation further supports the conclusions of Coakley and Davies (1986) concerning channel 3 reflectance increases near the cloud edge as a function of decreasing cloud droplet size distribution.

Reflectances across a broken stratocumulus cloud field are shown in cross-section E, found in Fig. 27. Again, there is an obvious variation in channel 3 reflectance towards the edges of the cloud fields. As the cross-section approaches a cloud edge, the channel 3 reflectance increases in conjunction with decreasing droplet size. There is usually a slight decrease in reflectivity at the immediate edge, since the clouds at this point are reaching a sufficiently thin optical depth and no longer appear infinitely thick to channel 3. Further decreases in cloud thickness cause decreases in channel 3 due to the diminishing number of cloud droplets available to scatter the incident radiation. Recall that the image processing technique drives the channel 3 reflectance value to zero where the associated channel 1 value has been scaled to zero. In reality, there may be a small contribution to channel 3 between the cloud regions, but it is from the ocean surface and hinders the ability to analyze the clouds.

Satellite-aircraft geographic coincidence occurs again on 30 June. The reflectance is shown in Fig. 28 as cross-section F. Channel 1 decreases towards the continental air to the east, from an average reflectance of 0.85 to 0.80. Channel 3

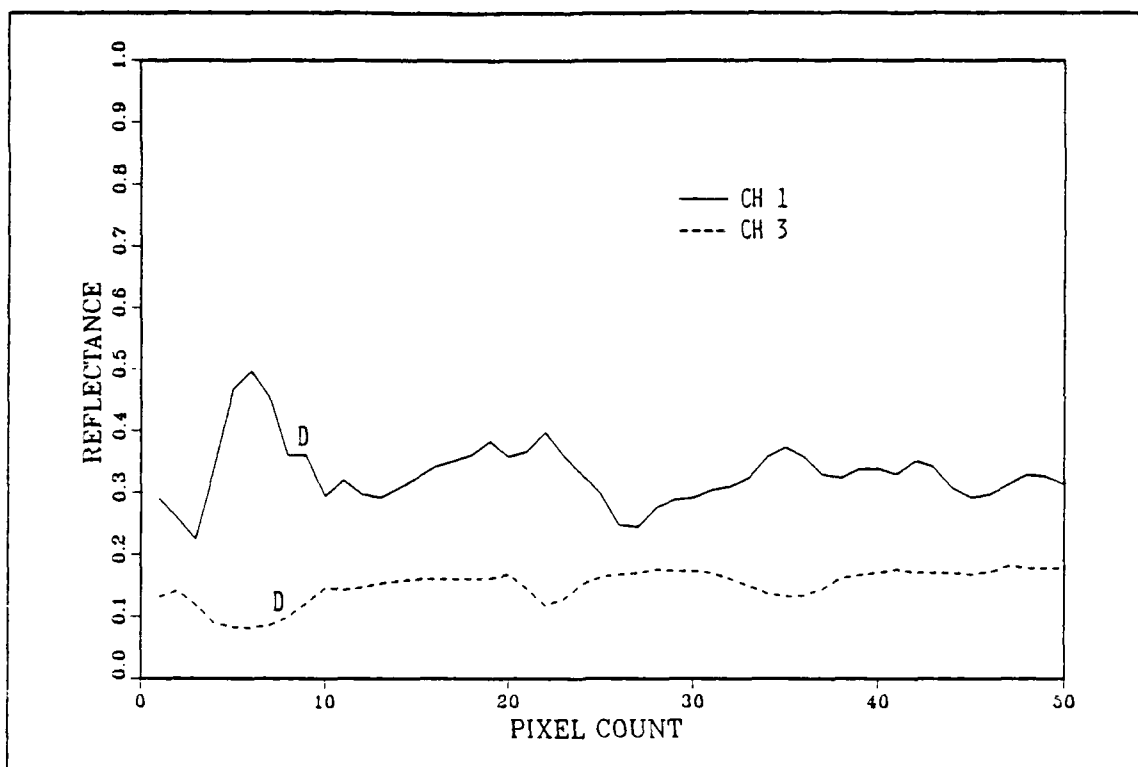


Fig. 26. Reflectance Cross-Section D: Sampled west to east; coincides with location of 29 June NCAR Electra mission.

reflectance increases from 0.08 to 0.14 across the sampled path, representing a change in droplet size distribution modal radius of approximately $1.5\mu\text{m}$.

Cross-section G is illustrated in Fig. 29 and is a good example of the different effect in the two channels resulting from cloud optical depth variations. Large excursions in channel 1 reflectance result from the sensitivity of this channel to variations in cloud thickness. The associated channel 3 values remain relatively immune to these variations, but appear slightly more variable than previous examples in conjunction with cloud microphysical fluctuations in the horizontal. Channel 3 reflectance increases from an average of 0.08 to 0.16 from north to south along the cross-section.

The final reflectance cross-section for CS1 is labeled H and is shown in Fig. 30. This track illustrates the effects of offshore flow in the immediate vicinity of the Los Angeles basin. The influence of a substantial source of CCN of urban/industrial origin is readily apparent in both channels. The channel 1 profile indicates a 0.2 drop in reflectance at the extent of the strong continental influence from the loss of optical depth

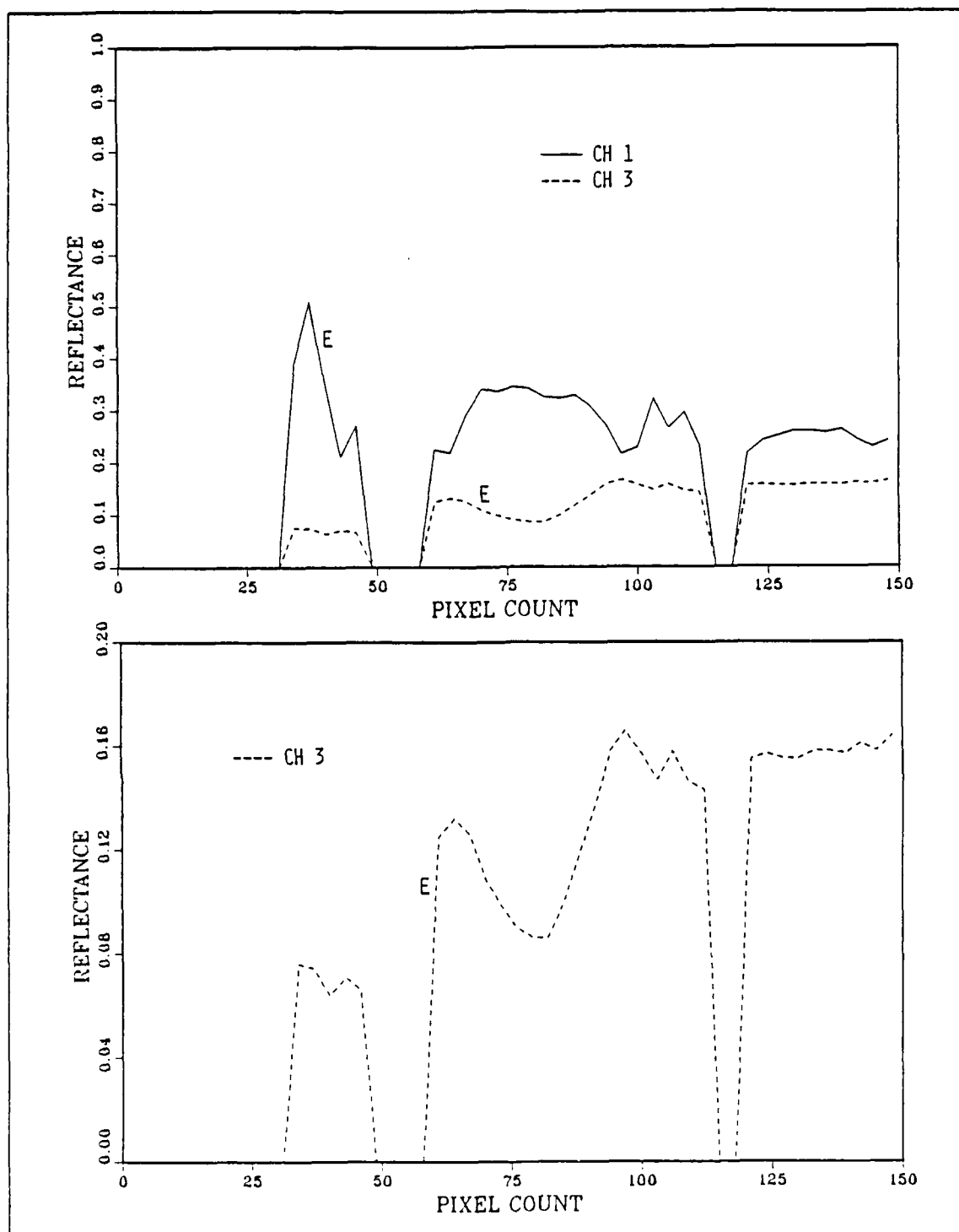


Fig. 27. Reflectance Cross-Section E: Sampled north to south.

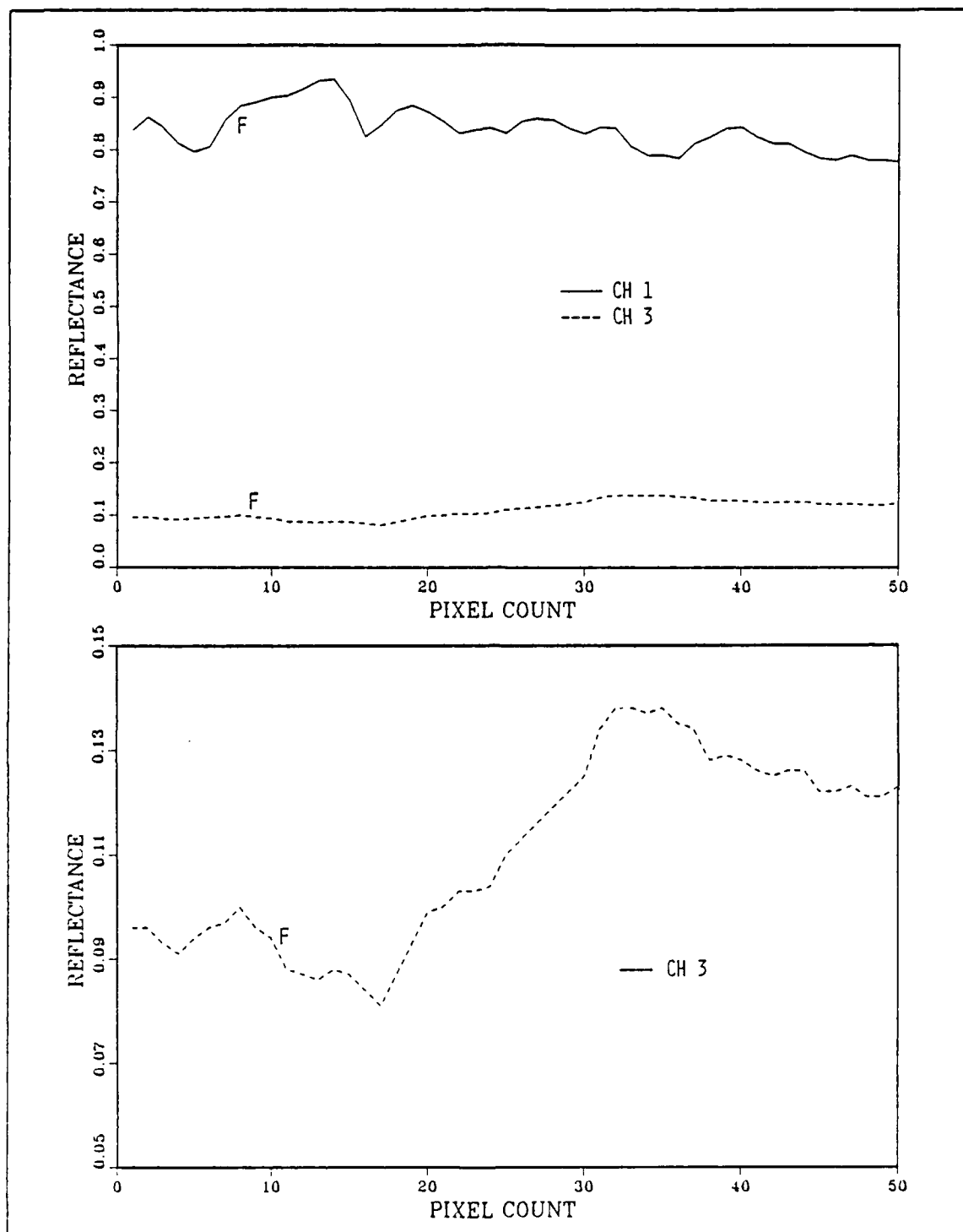


Fig. 28. Reflectance Cross-Section F: Sampled west to east; coincides with location of 30 June NCAR Electra mission.

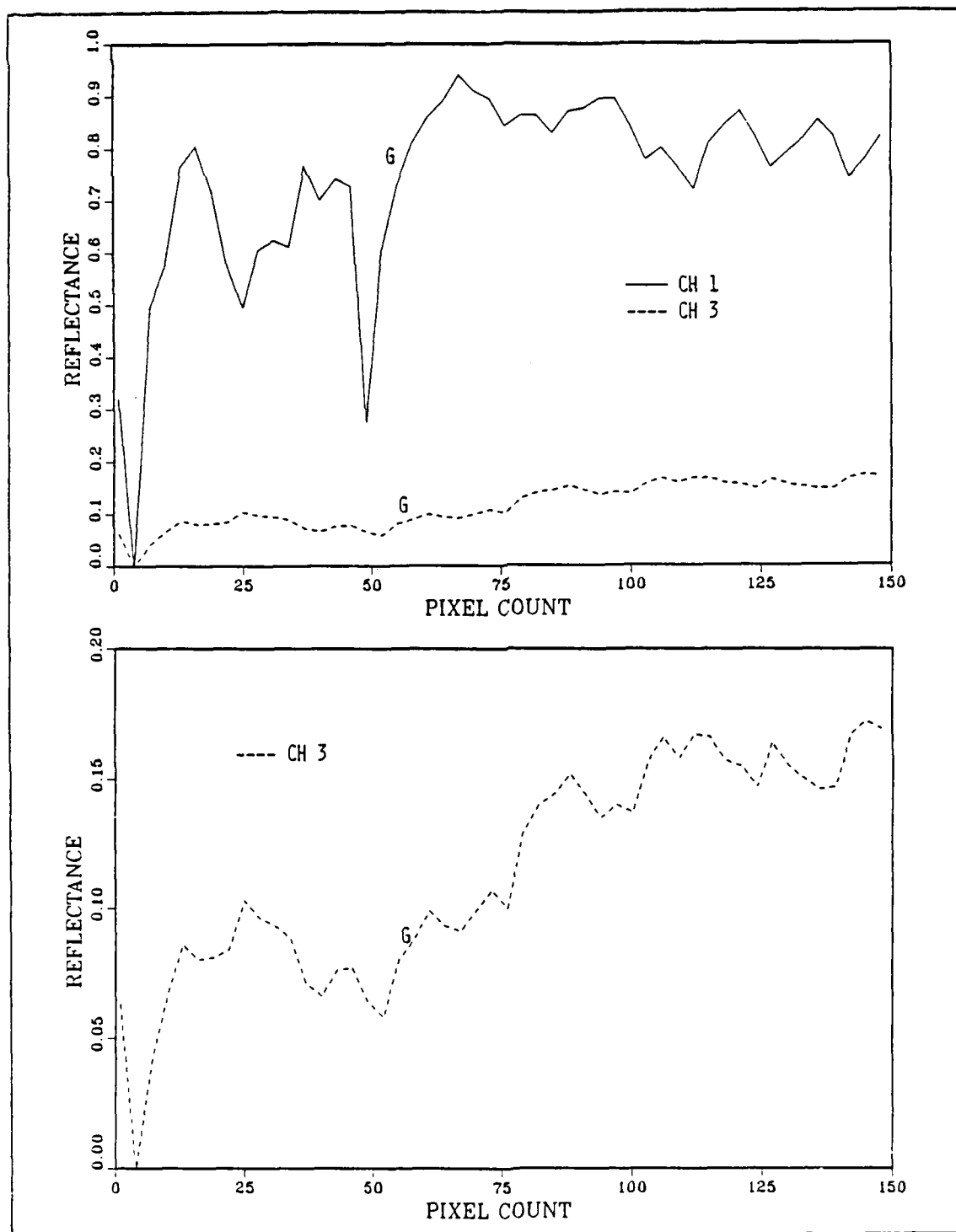


Fig. 29. Reflectance Cross-Section G: Sampled north to south.

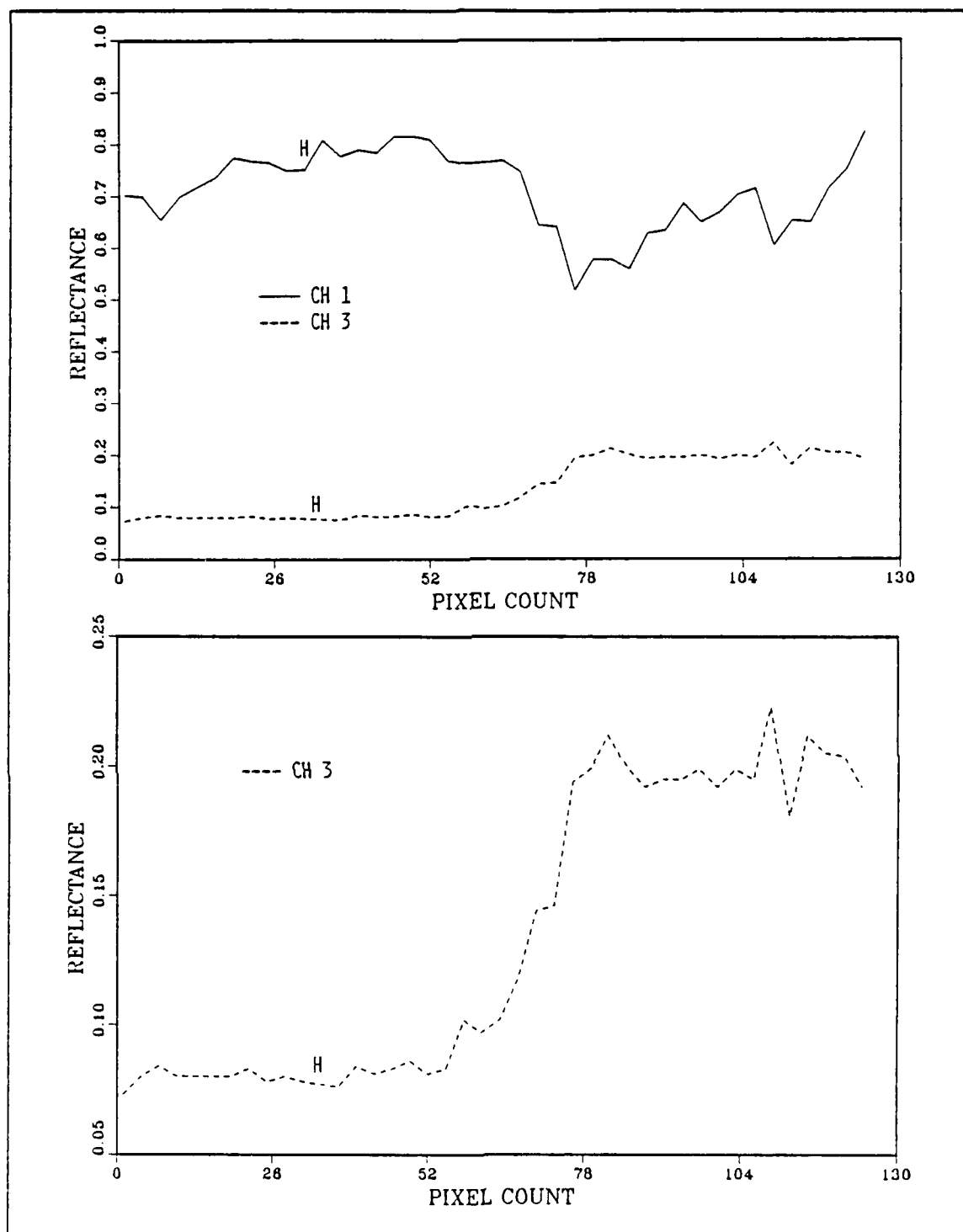


Fig. 30. Reflectance Cross-Section H: Sampled southwest to northeast.

associated with air of less EQLWC. Channel 3 rises sharply at the interface, from an average reflectance of 0.08 to 0.2. More complex circulation patterns within this region of influence and the accompanying variations in cloud microphysical properties add considerable structure to the channel 3 reflectance. The reflectance gradient suggests a change in cloud droplet modal radius of approximately $3\mu\text{m}$.

d. Aircraft Data

(1) *29 June 1987.* The mission track for the NCAR Electra on 29 June is shown in Fig. 31, with the track segment from point C to point B corresponding with satellite reflectance cross-section D from Fig. 26. The Electra data are taken from 2115-2120 UTC while the aircraft maintained a posture just below the cloud top, ascending from 1040 meters at time 2115 UTC to the approximate location of the cloud top (1065 meters) at time 2120 UTC. This corresponds to the center half of the point C to point B mission leg. PMS data for 29 June are displayed in Table 8. Although the aircraft track does not cross any significant continental/marine gradient, a general trend towards higher droplet concentration and smaller cloud droplet mean radius is observed as the aircraft passes from west to east. This is consistent with the gradual increase in reflectance illustrated in cross-section D.

TABLE 8
SELECTED NCAR ELECTRA DATA FOR 29 JUNE 1987

Time (UTC) ($\pm 20\text{sec}$)	APN-159 Altitude (m)	PMS-King EQLWC (g/m^3)	ASASP conc. (N/cm^3)	ASASP mean radius (μm)	FSSP conc. (N/cm^3)	FSSP mean radius (μm)
2115	1010	0.31	N/A	N/A	48	9.3
2116	1035	0.32	N/A	N/A	54	8.8
2117	1040	0.30	N/A	N/A	55	8.5
2118	1055	0.29	N/A	N/A	68	8.4
2119	1050	0.29	N/A	N/A	58	8.5

(2) *30 June 1987.* The NCAR Electra mission track on 30 June is illustrated in Fig. 32; the track segment from B to A corresponding with reflectance cross-section F found in Fig. 28. The aircraft data are taken from two cloud sounding passes, from 2032-2042 UTC (B to A) and from 2306-2316 UTC (A to B). In these sounding runs, the aircraft "porpoises" between cloud base and the clear air in the inversion above

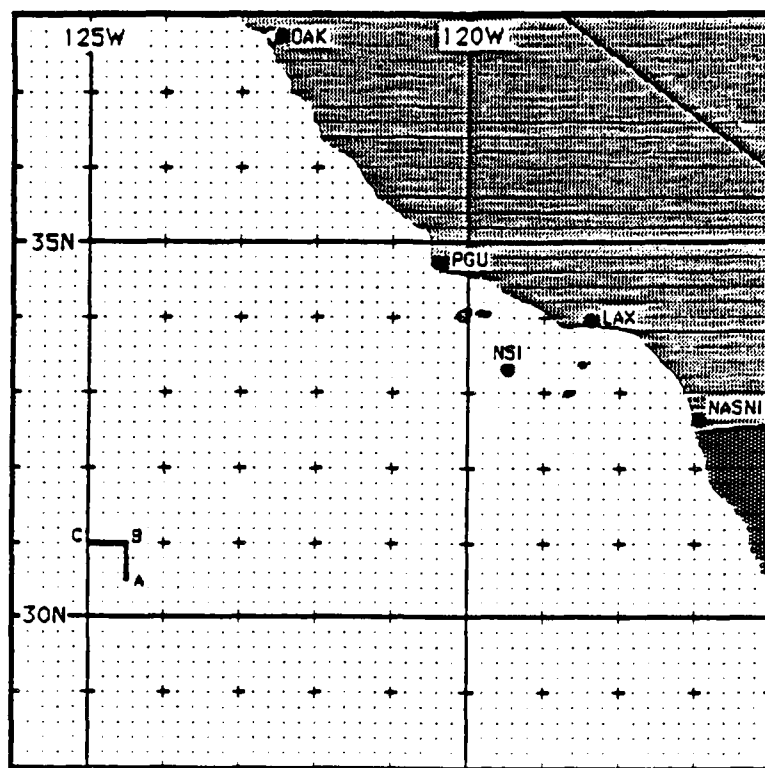


Fig. 31. NCAR Electra Flight Track, 29 June 1987: (from Kloesel *et al.*, 1988).

the cloud top. This flight profile is especially useful in defining the cloud microphysical structure near the cloud top, being the source of channel 3 reflectance; however, it limits the data describing horizontal variations at any one level. In the first sounding leg, the aircraft climbs through the cloud top at 20:33:20, 20:38:30 and at 20:41:05 UTC; descends into the cloud top at 20:35:40 and at 20:38:30 UTC, and dips slightly below the cloud base at 20:36:30 and at 20:40:20 UTC. In the second sounding run, the aircraft exits cloud top near 23:07:50 and 23:13:00 UTC; descends into the cloud at 23:10:15 and 23:15:15 UTC; and is at the cloud base at 23:06:55, 23:11:55, and 23:17:05 UTC. PMS data for both sounding legs are shown in Table 9.

In both aircraft sampling legs, there are indications of a shift toward higher droplet concentrations and smaller droplet radius at the eastern end of the track.

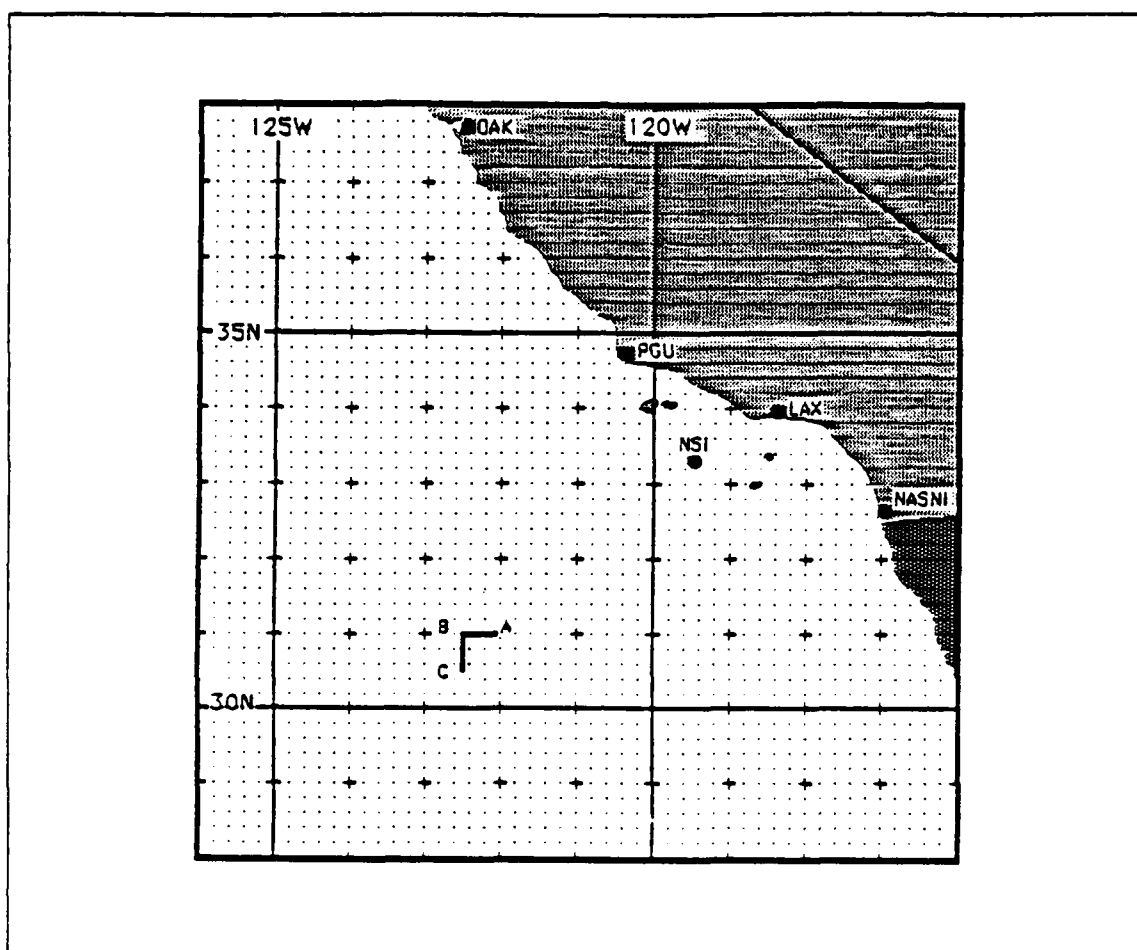


Fig. 32. NCAR Electra Flight Track, 30 June 1987: (from Kloesel *et al.*, 1988).

This is consistent with the trend expected from a review of cross-section F. Fig. 33 shows droplet size distribution histograms at one sample per second averaged over one minute for the cloud samples closest to the aircraft track endpoints in both aircraft sampling runs. In both cases, the distribution nearer to point A is shifted towards a smaller droplet modal radius and the concentration of large droplets decreases.

2. CS2 (13-14 July)

a. Synoptic Summary

A general transition from trough to ridge at the level of non-divergence characterizes the synoptic evolution during CS2. On 12 July a 500 mb trough exists over the Rocky Mountains and continues its movement to the east through the period. A ridge begins to gradually build at 136°W, impinging on the coast near Washington and

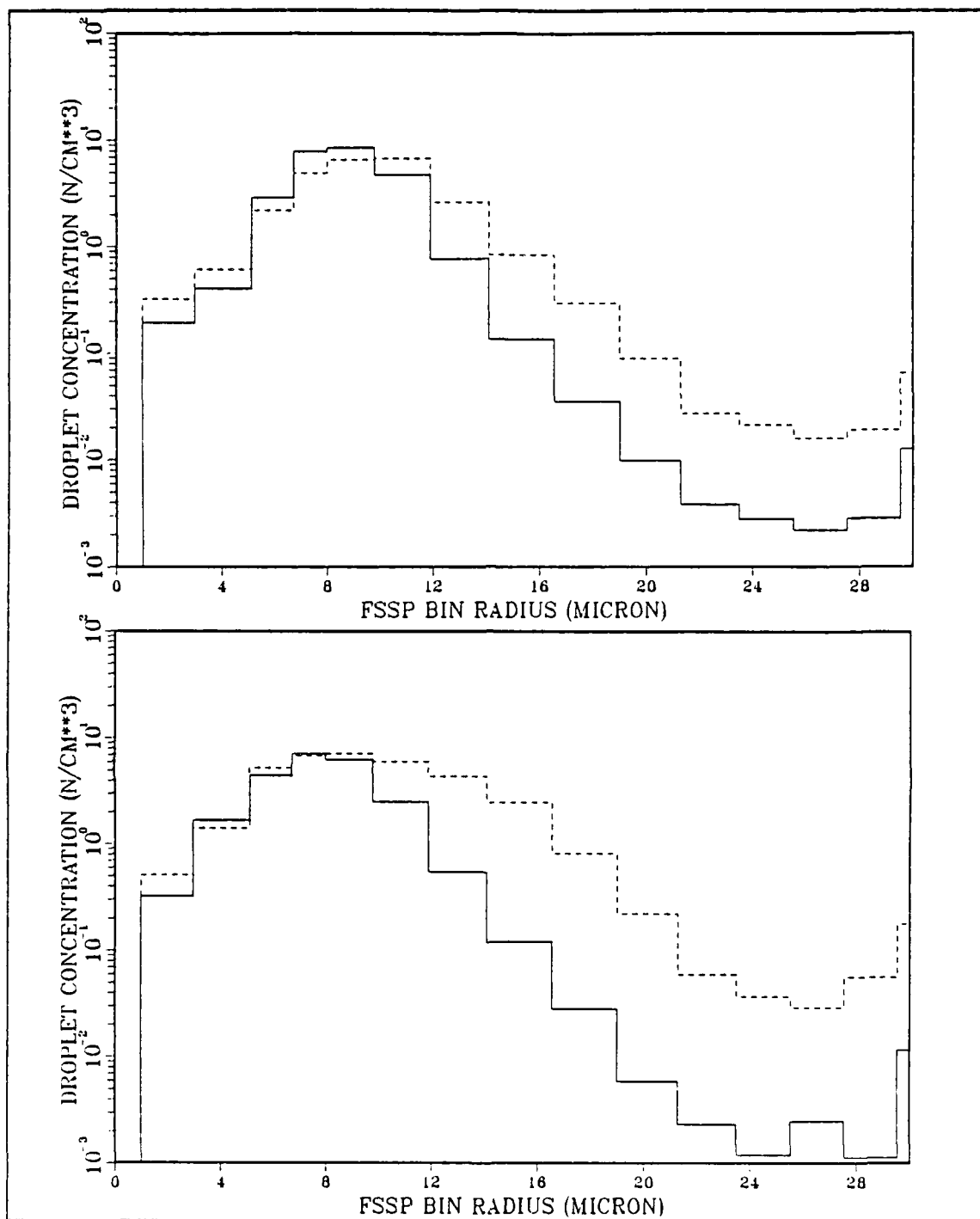


Fig. 33. FSSP Probe Droplet Size Distribution Histograms for 30 June 1987: First leg (top) and second leg (bottom). Dashed lines are cloud samples near point B, solid lines represent point A.

TABLE 9
SELECTED NCAR ELECTRA DATA FOR 30 JUNE 1987

Time (UTC) (± 20 sec)	APN-159 Altitude (m)	PMS-King EQLWC (g/m ³)	ASASP conc. (N/cm ³)	ASASP mean radius (μ m)	FSSP conc. (N/cm ³)	FSSP mean radius (μ m)
2033	870	0.29	N/A	N/A	30	10.5
2036	810	0.26	N/A	N/A	30	10.0
2037	870	0.28	N/A	N/A	38	11.0
2039	900	0.29	N/A	N/A	55	10.0
2041	840	0.23	N/A	N/A	33	9.0
2308	900	0.31	N/A	N/A	37	9.0
2310	940	0.31	N/A	N/A	39	10.3
2313	930	0.28	N/A	N/A	32	10.8
2316	920	0.32	N/A	N/A	30	10.5

British Columbia. The center of the subtropical high is located at 39°N 142°W, with a lobe of the high reaching the IFO operating area. The 1010 mb central pressure of the thermal trough is several millibars higher than the previous day, resulting in light, northwesterly surface winds over the region of interest. Significant offshore flow exists from northern California to Washington that decays in strength as the day progresses. The 500 mb ridge builds to 5940 meters on 13 July and moves over the coast, as the surface high builds in toward Canada as shown in Fig. 34. Also, the thermal trough strengthens to 1009 mb causing an increase in the strength of northwesterly winds off the southern California coast. Continued strengthening of the subtropical high and the thermal trough (to 1007 mb) on 14 July, illustrated in Fig. 35, results in strong northwesterly winds over the operating area. The 500 mb pressure gradients are quite weak. Rawinsonde soundings taken from the research vessel POINT SUR, operating just upwind from San Nicolas Island, are displayed in Fig. 36. The soundings confirm the presence of strong subsidence and vertical decoupling across the stable inversion allowing the shallow thermal trough to build the surface winds.

In a situation similar to CSI, the NORAPS trajectory analyses shown in Figs. 37 through 40 reveal a source of continental air being advected into the IFO operating area. Strong offshore flow exists over northern California on 12 July at 925 mb up through and including the 700 mb level. A shear zone exists near 125°W at all levels,

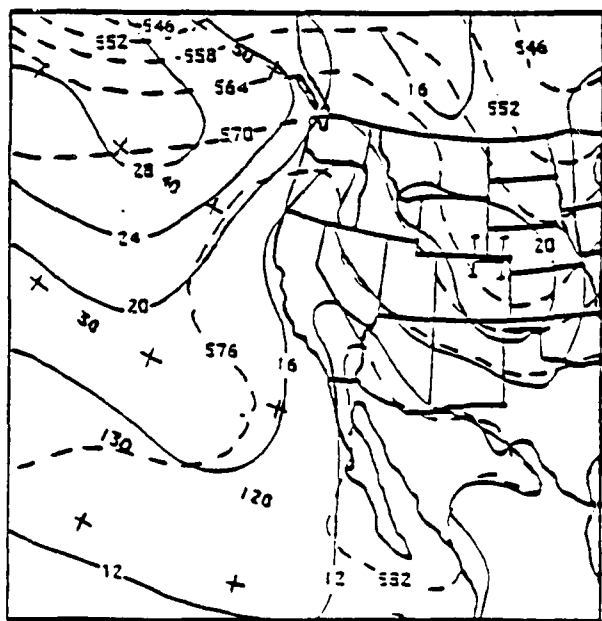
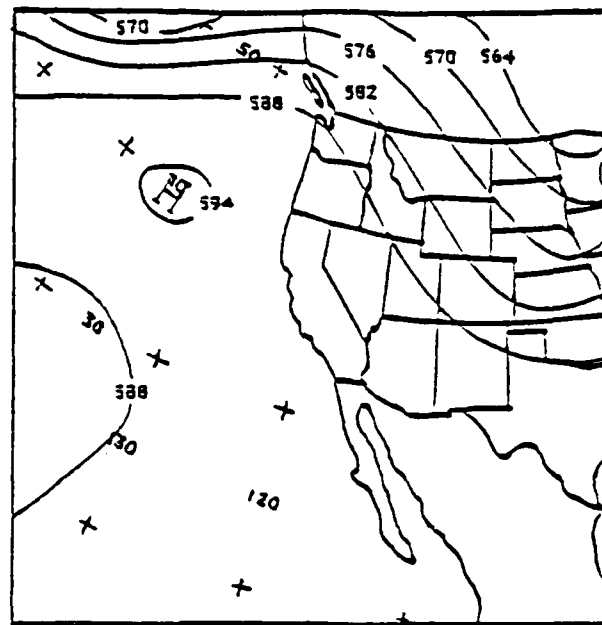
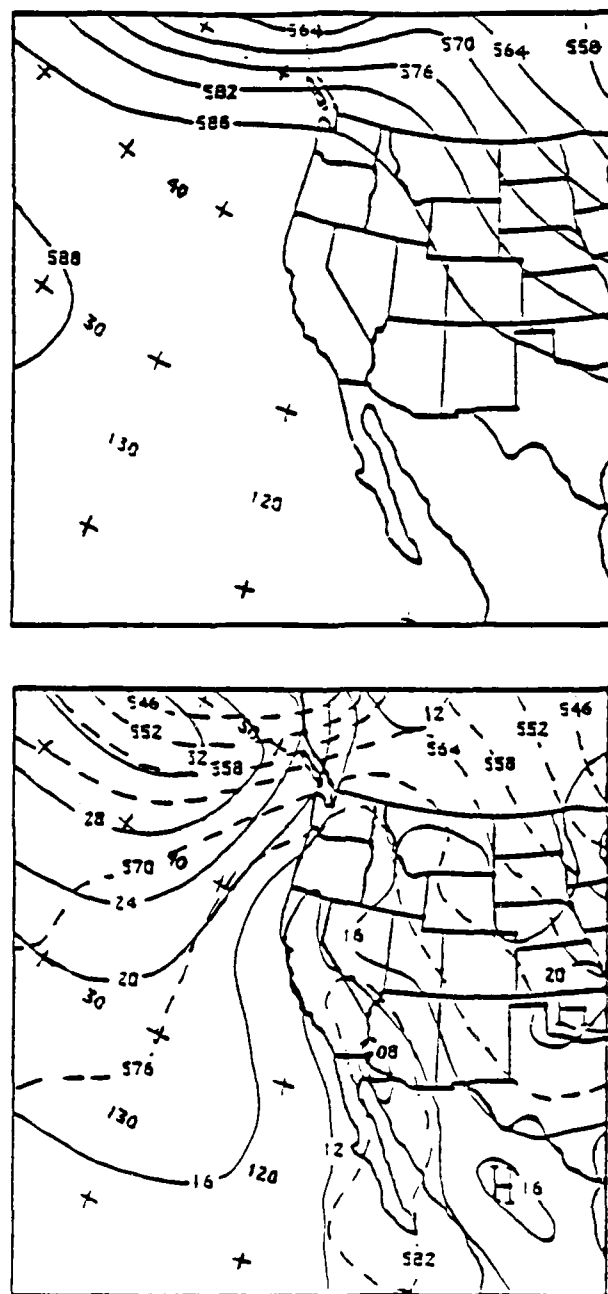


Fig. 34. 13 July 1987 12 UTC Regional OI Analysis: 500 mb heights (top) and surface pressure/1000-500 mb thickness (bottom).



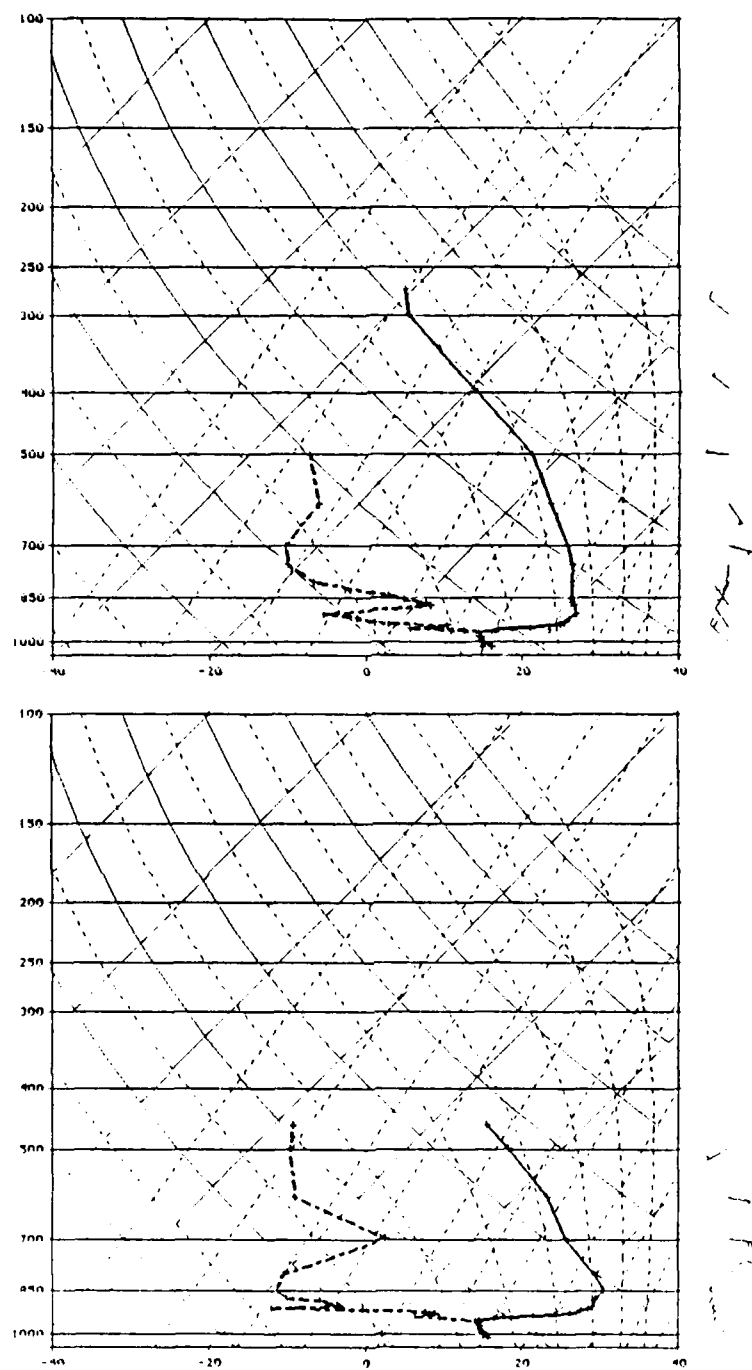


Fig. 36. Research Vessel POINT SUR Rawinsonde Soundings: 13 July 1987 1758 UTC (top) and 14 July 1987 1802 UTC (bottom), station location 33.5°N 120°W.

but especially at 850 and 700 mb where a weak trough is driving southerly flow near the coast. As the surface pressure gradient builds on 13 July, strong northwesterly flow becomes apparent at 1000 mb, advecting air of a continental nature into the operating area. This shift in the flow pattern is consistent with the replacement of continentally influenced air off the northern California coast with marine air from the northwest. Offshore winds are still providing a source of continental CCN both above and below the subsidence inversion over northern California in the early stages of the case study period. The evolving flow pattern is of a nature that should confine continentally influenced air nearer to the coastline with decreasing latitude.

b. AVHRR Subscenes

Satellite subscenes found in CS2 are listed in Table 10. As in CS1, the priority for subscene location is the location of cloud field reflectance gradients indicating differences in air mass qualities.

TABLE 10 CS2 SATELLITE SUBSCENES				
DATE	PLATFORM	LATITUDE 35°N CROSSING TIME	SUBSCENE CENTER COORDINATES	FIGURE
13 July	NOAA-10	16:12:55 UTC	32°48.7'N 120°29.7'W	41/42
13 July	NOAA-9	23:20:35 UTC	33°57.8'N 123°30.1'W	43/44
14 July	NOAA-10	15:51:00 UTC	34°59.8'N 124°16.9'W	45/46
14 July	NOAA-9	23:09:40 UTC	32°33.7'N 121°48.8'W	47/48

The channel 1 and 3 reflectance patterns for the morning of 13 July are illustrated in Figs. 41 and 42. The visible image indicates mixing of the dry air above the inversion into the MABL downwind of the coastal boundary east of Point Conception and the Channel Islands due to the strong northwesterly surface winds. The stratocumulus cells are aligned in streets parallel to the flow, with larger individual cells apparent in the western extreme of the image. The stratocumulus field is slightly less reflective near the coast north of Point Conception. The channel 3 image shows an unmistakable contrast between the continental and marine air masses. The brighter region is broader to the north where it is closer to the origin of the offshore flow, and confined near the coast by the advection pattern further to the south. Even brighter regions are found against the coast where the continental CCN influence is greatest.

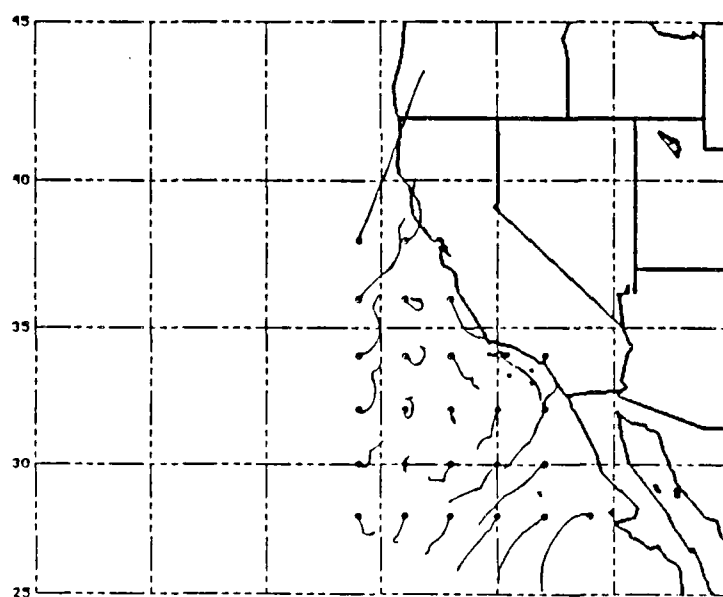
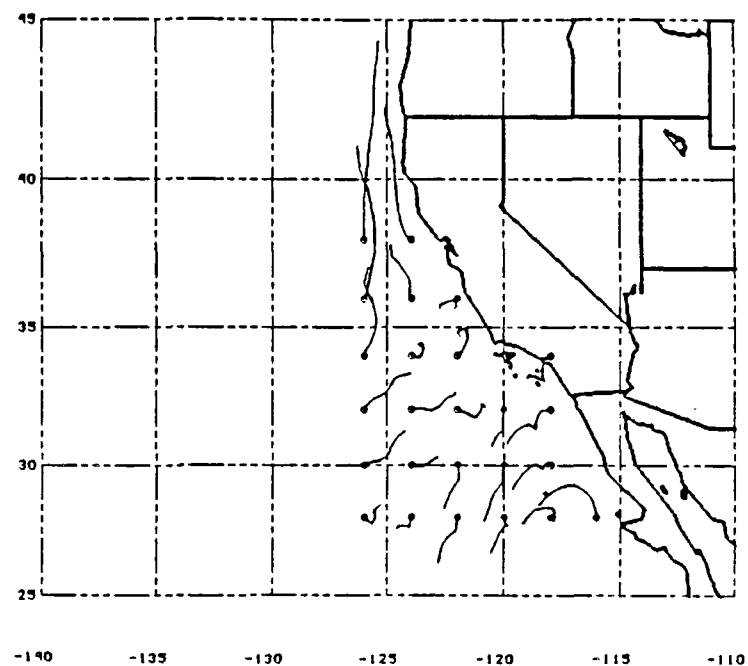


Fig. 37. NORAPS 12 July 1987 00-24 UTC Parcel Trajectories: 1000 mb pressure at 24 UTC (top) and 925 mb pressure at 24 UTC (bottom), circle indicates 24 UTC position.

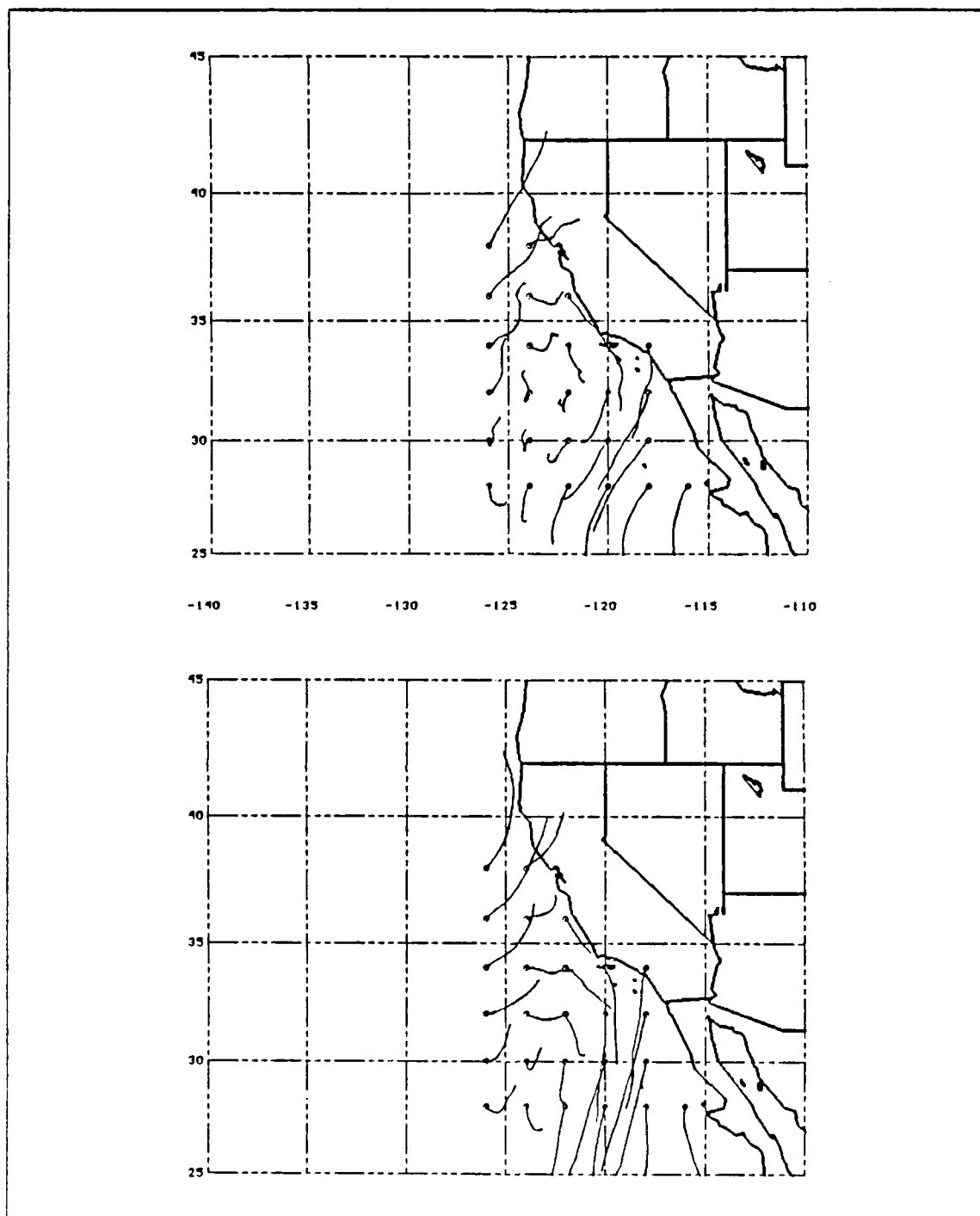


Fig. 38. NORAPS 12 July 1987 00-24 UTC Parcel Trajectories: 850 mb pressure at 24 UTC (top) and 700 mb pressure at 24 UTC (bottom), circle indicates 24 UTC position.

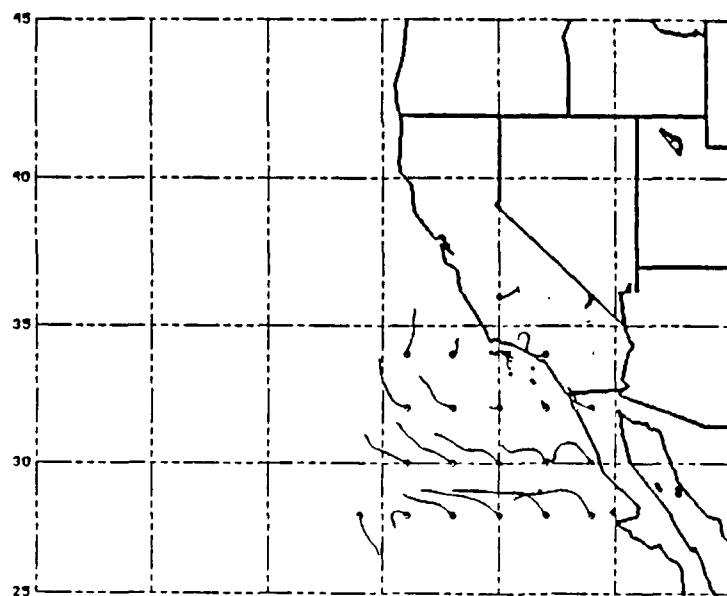
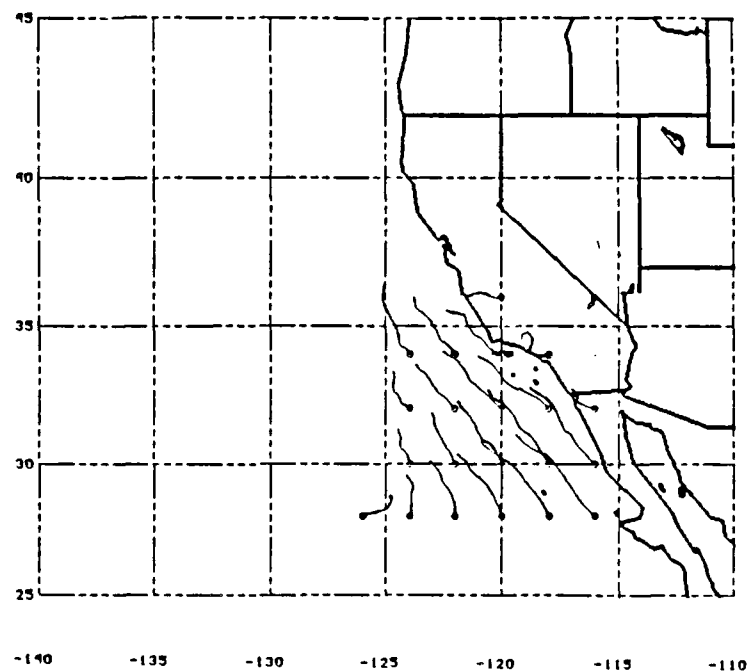


Fig. 39. NORAPS 13 July 1987 00-24 UTC Parcel Trajectories: 1000 mb pressure at 24 UTC (top) and 925 mb pressure at 24 UTC (bottom), circle indicates 24 UTC position.

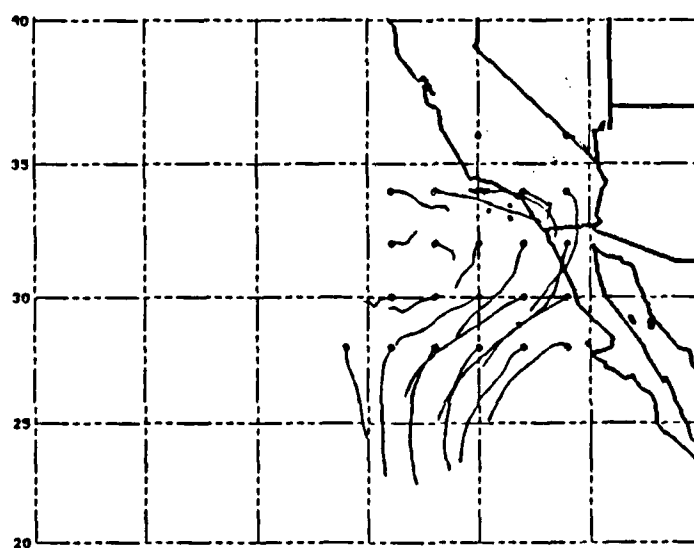
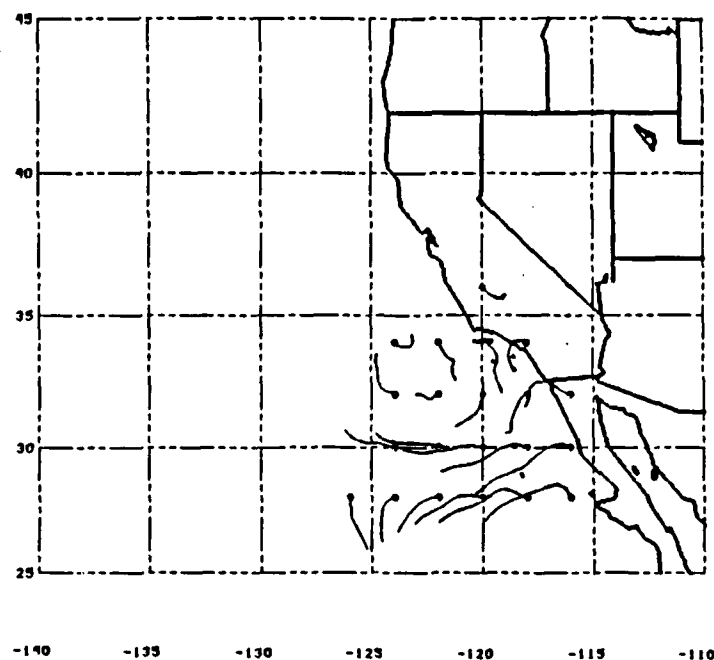


Fig. 40. NORAPS 13 July 1987 00-24 UTC Parcel Trajectories: 850 mb pressure at 24 UTC (top) and 700 mb pressure at 24 UTC (bottom), circle indicates 24 UTC position.



Fig. 41. NOAA-10 AVHRR 1613 UTC 13 July 1987 Channel 1: Line segments indicate reflectance cross-sections M and N. Center coordinates $32^{\circ}48.7'N$ $120^{\circ}29.7'W$.



Fig. 42. NOAA-10 AVHRR 1613 UTC July 1987 Channel 3 Reflectance: Line segments indicate reflectance cross-sections M and N. Center coordinates $32^{\circ}48.7'N$ $120^{\circ}29.7'W$.

The subscene images from the NOAA-9 afternoon pass, shown in Figs. 43 and 44, are centered further north in the operating area off the south-central California coast. Channel 1 reveals a relatively uniform stratocumulus cloud field over the region. The clouds in the northwest half of the image show more of a cellular structure, with the cell centers appearing the brightest. The clouds closer to land are also structured, but are more uniform in brightness. The high reflectance in channel 3 near the coast is a result of the subscene being near the source of offshore flow on 13 July. The center of the image displays a north-south reflectance band which is not as bright as the air nearer to the coast under the immediate influence of continental aerosols, but is brighter than the marine air which appears further to the west. The clouds of intermediate brightness in this image are most likely the result of air which was advected offshore further north. The clouds within this air mass may be under the influence of CCN of different composition and concentration than the air mass closer to the coast. In addition, microphysical modifications to CCN content during the time the air mass is advected over the ocean may create a small difference in radiative properties by the time these parcels reach the operating area. As discussed by Noonkester (1984), continental air existing over the ocean is continually being modified by the aerosol loss processes described in Chapter II. Note that this region of intermediate brightness has a similar channel 3 reflectance to the continental regime observed further south during the morning.

The channel 1 image for the morning of 14 July, found in Fig. 45, shows a continuous and uniform stratocumulus cloud field, slightly less bright in the eastern third of the subscene. The eddies which appear in the cloud topography over Monterey Bay and to the south along the coast indicate that surface winds are still relatively strong, and are in a direction along the coast. There are several interesting features in the channel 3 image, displayed in Fig. 46. The most prominent is the lower brightness near the coast within the region of continental influence. The clouds near the coast are brighter than the marine air to the southwest, as expected; but are not as bright as the clouds near the center of the image. The strong northwesterly flow has replaced the continental air mass near the coast with a surge of marine air from the northwest. The sequence of images seems to indicate that the region of high channel 3 reflectivity apparent in the 13 July NOAA-9 overpass has been advected rapidly southward by the strong ambient flow. The brighter region near the center of the image is most likely the result of a supply of continental air advected offshore over Oregon, Washington, and Canada.



Fig. 43. NOAA-9 AVHRR 2321 UTC 13 July 1987 Channel 1: Line segments indicate reflectance cross-sections O and P. Center coordinates $33^{\circ}57.8'N$ $123^{\circ}30.1'W$.

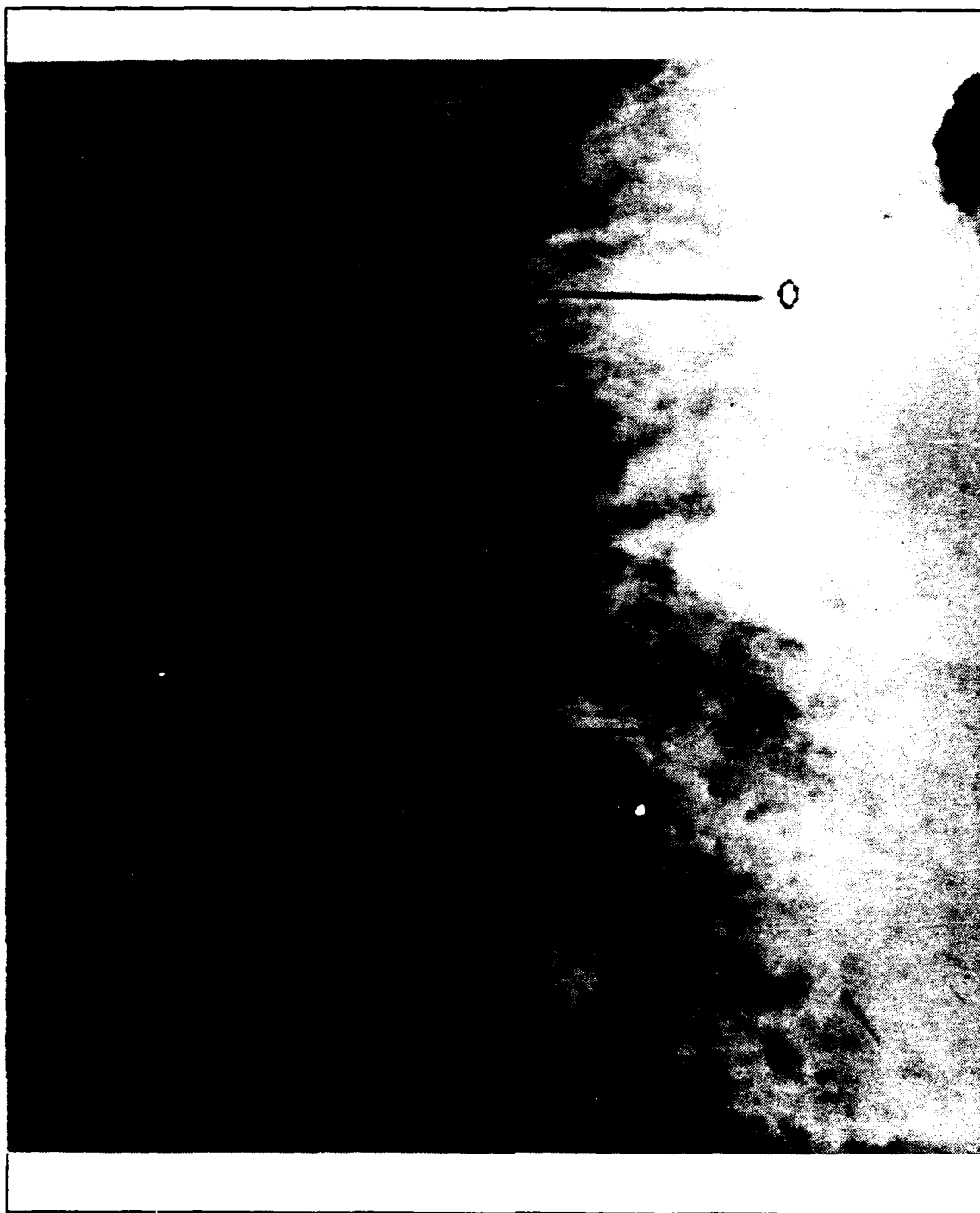


Fig. 44. NOAA-9 AVHRR 2321 UTC 13 July 1987 Channel 3 Reflectance: Line segments indicate reflectance cross-sections O and P. Center coordinates $33^{\circ}57.8'N$ $123^{\circ}30.1'W$.

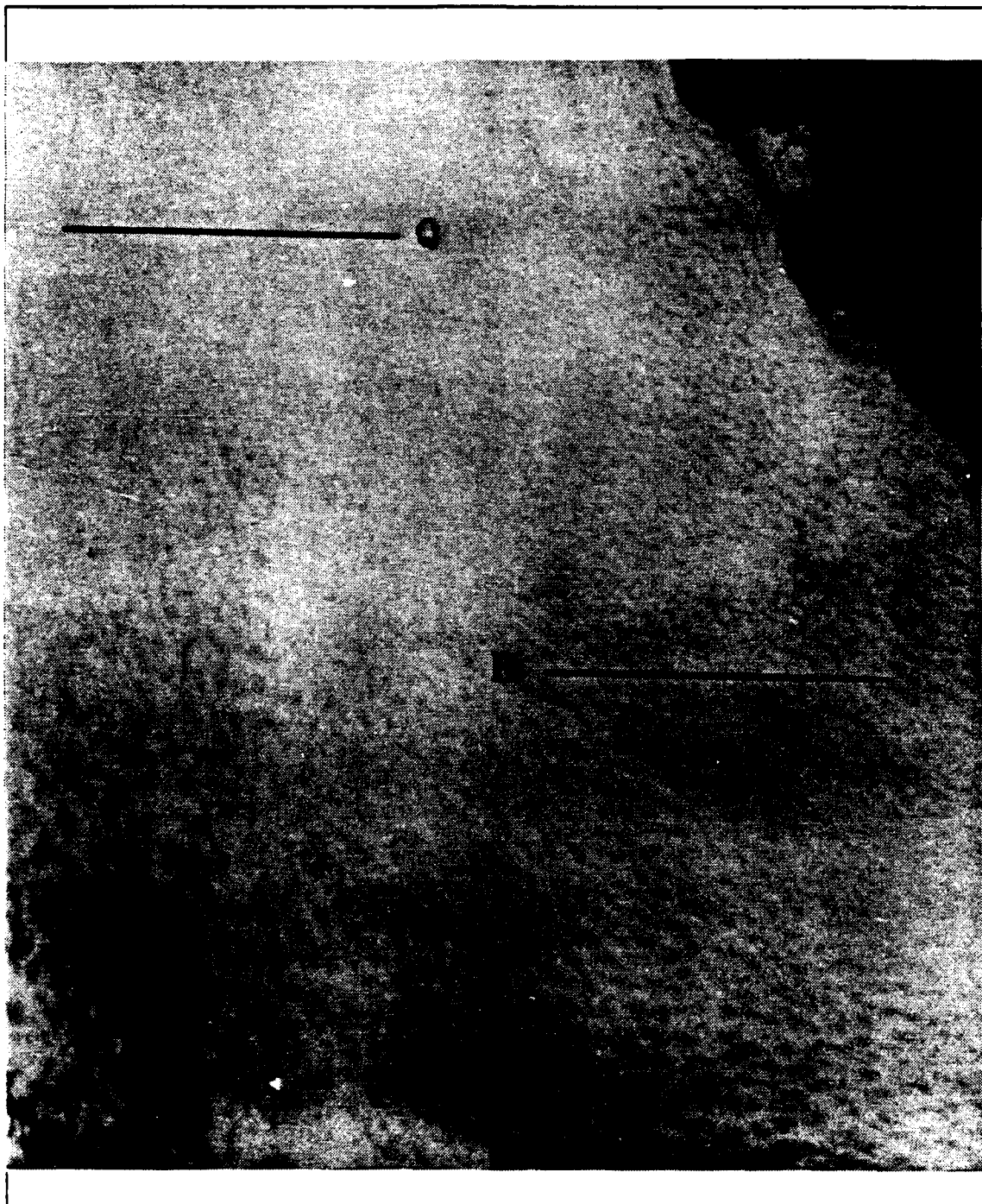


Fig. 45. NOAA-10 AVHRR 1551 UTC 14 July 1987 Channel 1: Line segments indicate reflectance cross-sections Q and R. Center coordinates 34°59.8'N 124°16.9'W.



Fig. 46. NOAA-10 AVHRR 1551 UTC 14 July 1987 Channel 3 Reflectance: Line segments indicate reflectance cross-sections Q and R. Center coordinates $34^{\circ}59.8'N$ $124^{\circ}16.9'W$.

The continental/marine interface observed on 13 July is along a north-south line left of the subscene center. The smaller cloud droplet size distribution associated with the thin stratus of the Salinas valley and within the small eddy south of Monterey are characteristically brighter than surrounding clouds. In addition, two ship tracks are highlighted, one in the northwest corner of the subscene and one near the subscene center.

Figs. 47 and 48 display channel 1 and 3 reflectance for the NOAA-9 afternoon pass on 14 July. The visible channel reveals the maintenance of continuous stratocumulus clouds, with the exception of the region of the Channel Islands. The southwestern third of the image appears more cellular in nature than the cloud field closer to the continent with the stratocumulus becoming more broken in the extreme southwest. A mesoscale gravity wave appears as a line of discontinuity along the coast north of Point Conception. This wave can be tracked using geostationary satellite data and is observed to propagate northwest to its approximate position in Fig. 47/48 and then dissipates in the ambient flow. Low channel 1 reflectance due to lower EQLWC and optical depth caused by entrainment is readily apparent to the southeast of this feature. The channel 3 image shows several regions of variable reflectance. The cloud field is most bright south of Point Conception and decreases in brightness towards the northwest across three diffuse boundaries of reflectance magnitude. A bright band extends northwest to southeast in the lower left quadrant of the subscene, with dark (marine influenced) reflectance to the south of this band. This feature is intersected by the NCAR Electra mission track for 14 July. As expected, the region southeast of the wave feature is brighter than the air mass north of the line of discontinuity.

The continental/marine interfaces in CS2 fluctuate longitudinally in relation to the wind field, as shown in Fig. 49. The history of continental surges of air is more complex in this case study since the surface winds are relatively strong and the surges of continental air are advected rapidly to the south. The positions of the continental/marine interfaces in Fig. 49 suggest that the strength of offshore flow and its north-south position along the coast determine the westward extent and the persistence of the continental influence.

c. Reflectance Cross-Sections

Channel 1 and 3 reflectance values for cross-sections M and N are displayed in Fig. 50. Again, the characteristic trend towards lower reflectance in continental air is seen in channel 1, with values decreasing from approximately 0.75-0.8 in the marine



Fig. 47. NOAA-9 AVHRR 2310 UTC 14 July 1987 Channel 1: Channel 1 (top) and channel 3 reflectance (bottom), with reflectance cross-sections S, T, and U. Center coordinates 32°33.7'N 121°48.8'W.

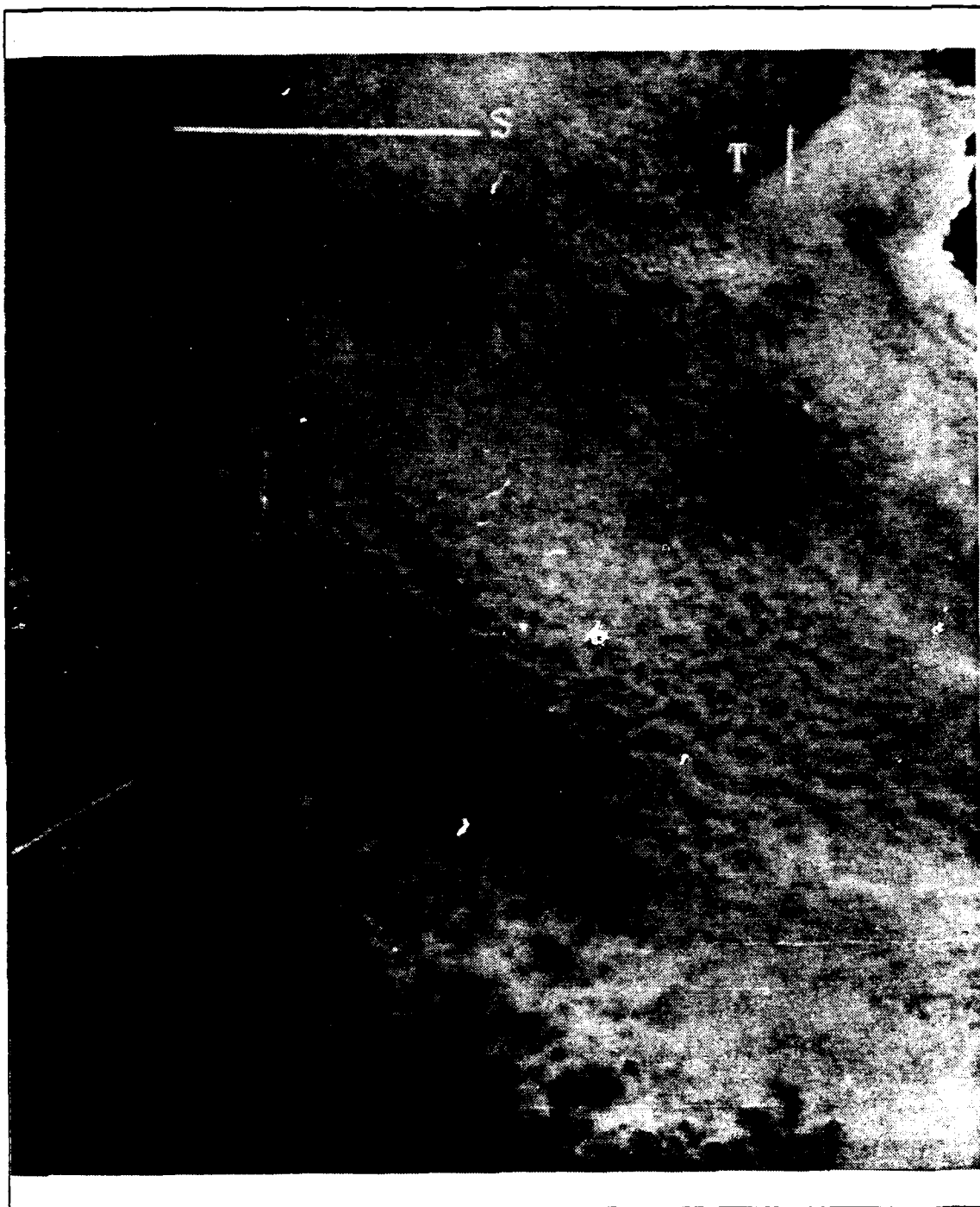


Fig. 48. NOAA-9 AVHRR 2310 UTC 14 July 1987 Channel 3 Reflectance: Line segments indicate reflectance cross-sections S, T, and U. Center coordinates $32^{\circ}33.7'N$ $121^{\circ}48.8'W$.

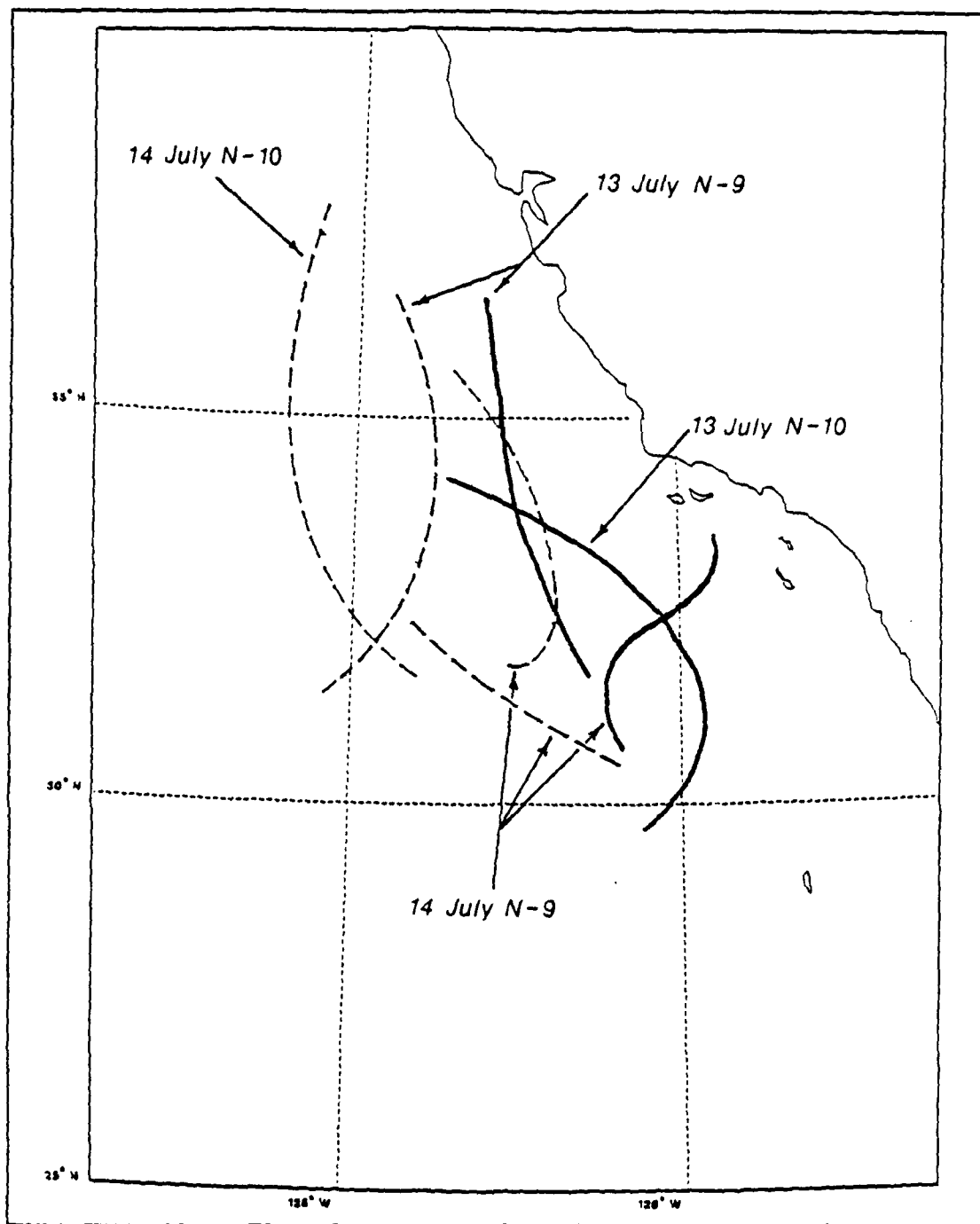


Fig. 49. CS2 Continental/Marine Air Mass Interface: Identified utilizing channel 3 reflectance from CS2 subscenes. Dashed lines indicate diffuse reflectance boundaries.

air to 0.7 across the boundary. The trend in channel 3 in the same direction is an increase from around 0.15 to 0.2, constituting a change in cloud droplet modal radius of approximately 1.5 to $2\mu\text{m}$ based on modal reflectance calculations. The channel 3 reflectance is somewhat more variable from pixel to pixel in this case, most likely due to droplet size distribution variations as a result of turbulent mixing from the strong surface wind conditions.

Fig. 51 shows cross-sections O and P from the 13 July NOAA-9 overpass. The decrease in channel 1 in the continental regime is again observed, and is much more evident in this figure. Channel 1 reflectance decreases from around 0.8 to 0.6 for cross-section O and from 0.75 to 0.5 for cross-section P. The gradient in channel 3 reflectance is also quite strong in this case, increasing approximately 0.2 for each case. The intermediate area of reflectance discussed in the previous section has a value near 0.21, similar to the reflectances obtained in the continental air mass from the morning NOAA-10 overpass. The area of "fresh" continental CCN near the coast displays some of the highest channel 3 reflectances (and the strongest trend toward low channel 1 reflectance) in this thesis. It can be expected that the cloud droplet size distribution within this region is strongly shifted toward the small end of the anticipated size spectrum.

Cross-sections Q and R, found in Fig. 52, show the conditions on the morning of 14 July. The channel 1 profiles show no significant trend, although they appear somewhat less variable due to the uniform nature of the stratocumulus cloud field. Cross-section Q in channel 3 shows a rise in reflectance from around 0.19 in the marine environment to 0.25 in continentally influenced conditions. The ship track at pixel 13 is clearly visible. Channel 3 cross-section R shows the decrease in reflectivity towards the coast, the source of which being the advection of marine air into the near-coastal environment due to the strong surface winds.

Cross-section S, shown in Fig. 53, displays the change in reflectance across a diffuse boundary of channel 3 reflectance intensity. Channel 1 reflectance is typically variable and remains near an average value of 0.7 over the cross-section. The associated channel 3 reflectance change is approximately 0.1 to 0.18 from marine to continental influence, corresponding to a model cloud droplet size distribution modal radius change of about $2\mu\text{m}$.

Fig. 54 displays a short, 25 pixel cross-section labeled as T, which traverses the wave feature seen in the 14 July NOAA-9 satellite data. The sharp decrease in channel 1 in conjunction with decreases in EQLWC and cloud optical depth dominate

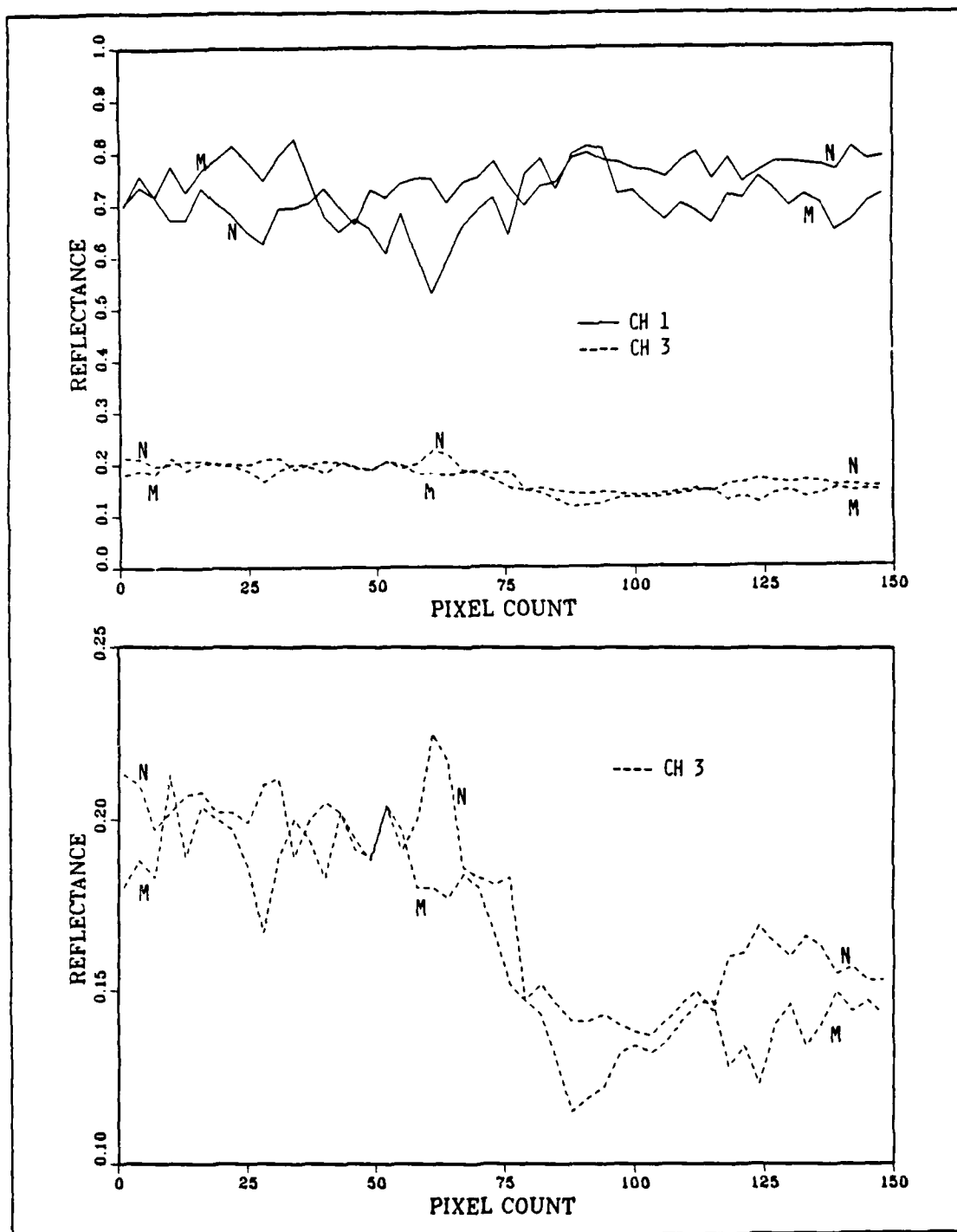


Fig. 50. Reflectance Cross-Sections M and N: Cross-section M sampled north to south; N sampled east to west.

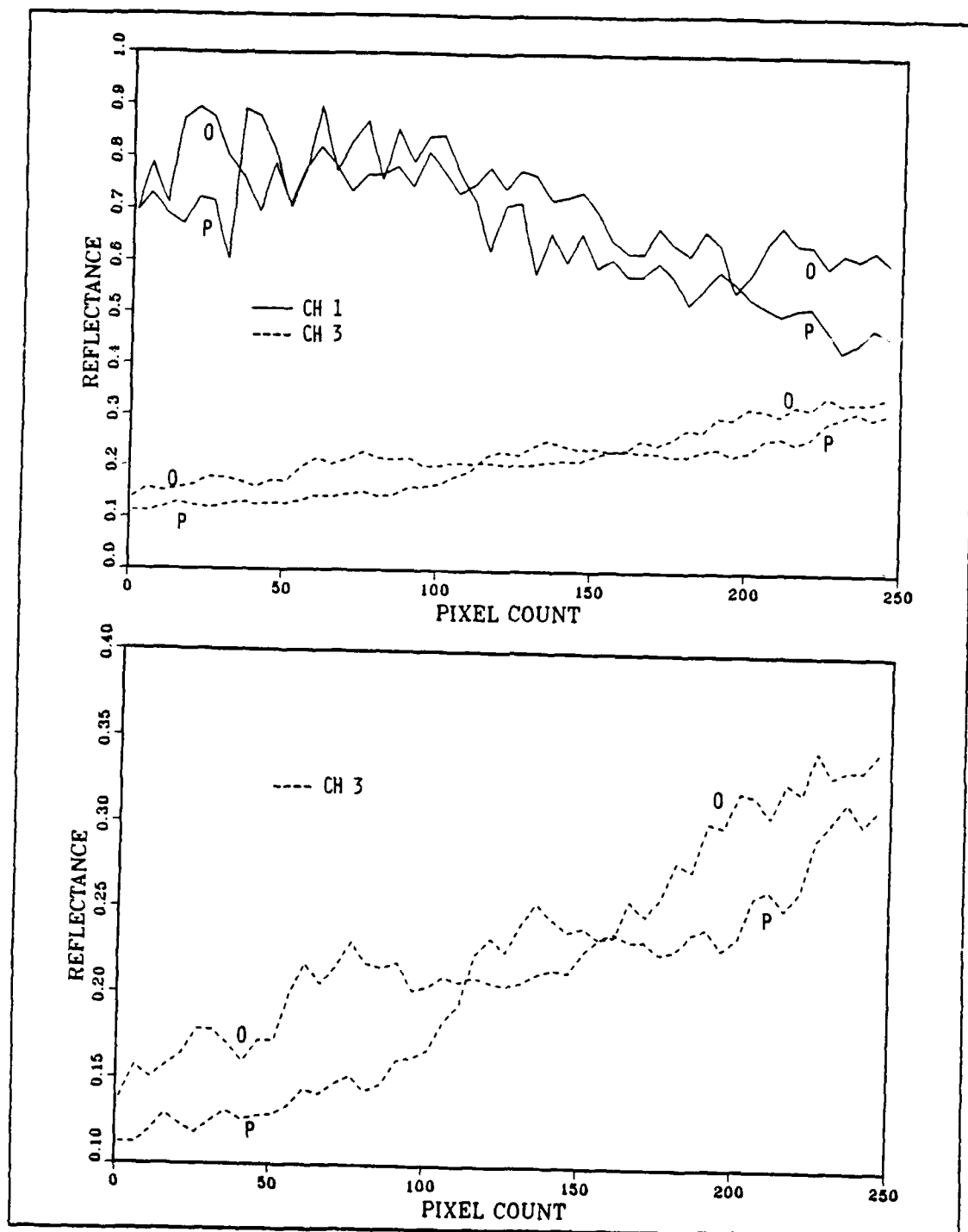


Fig. 51. Reflectance Cross-Sections O and P: Sampled west to east.

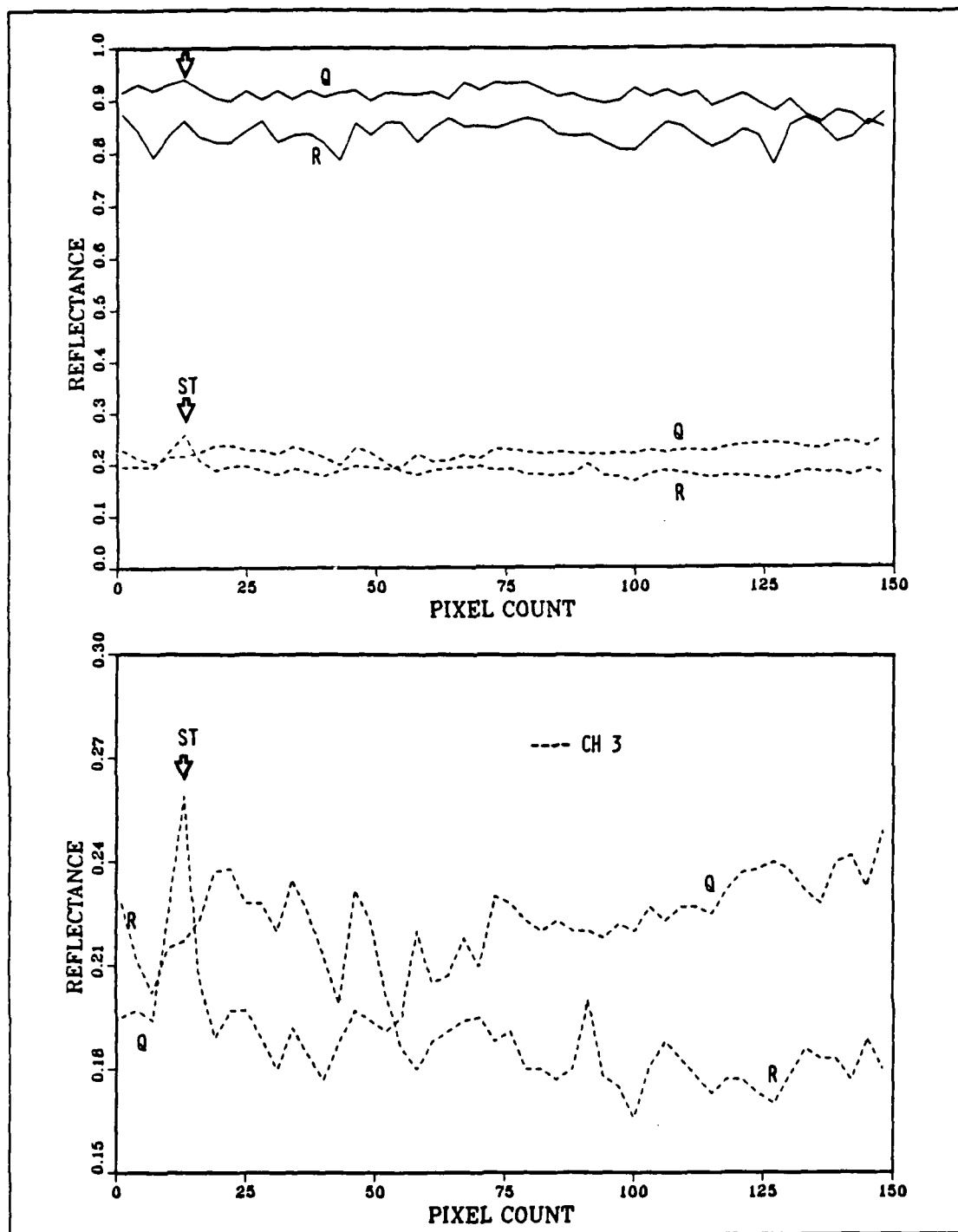


Fig. 52. Reflectance Cross-Sections Q and R: Sampled west to east; ST denotes position of ship track.

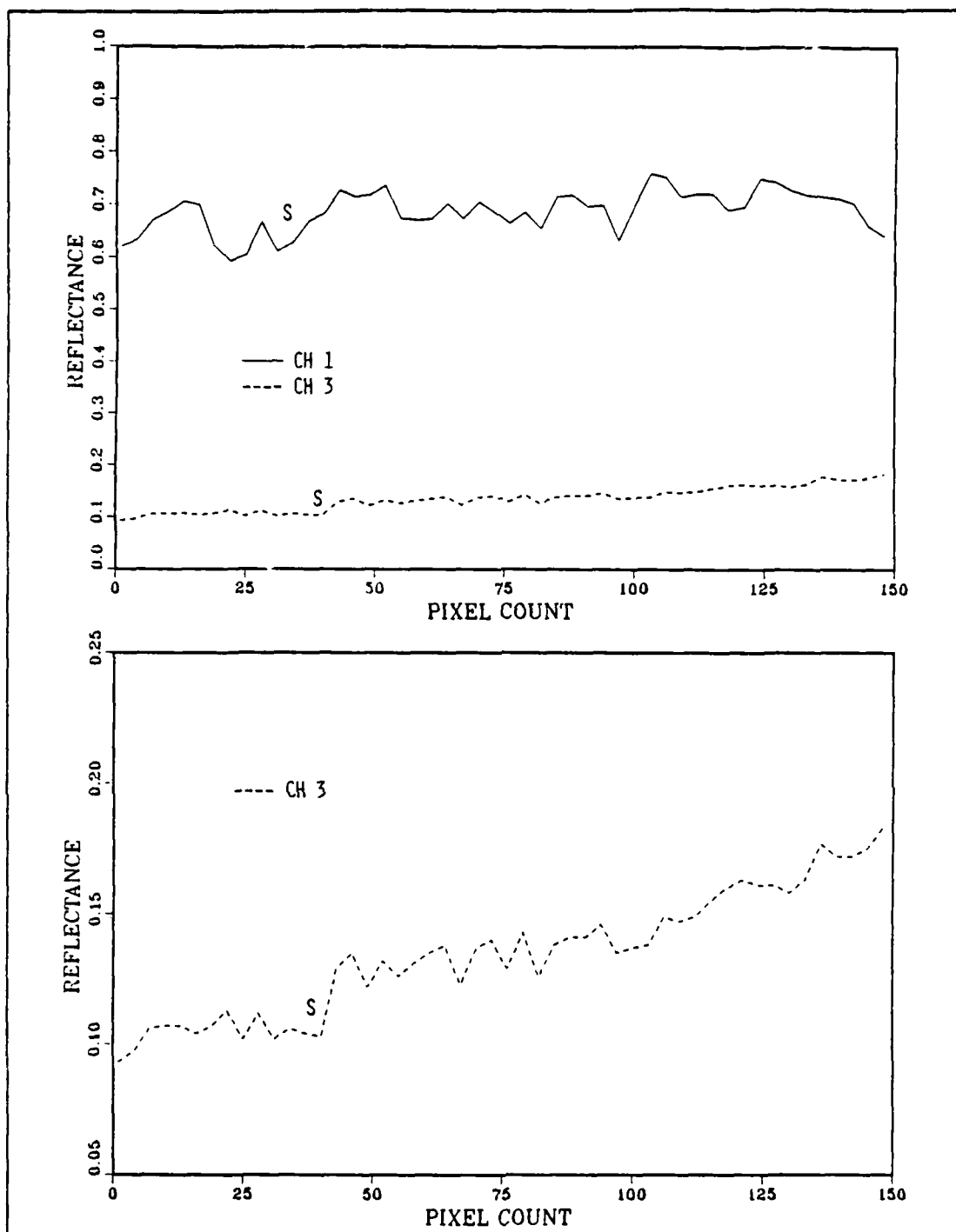


Fig. 53. Reflectance Cross-Section S: Sampled west to east.

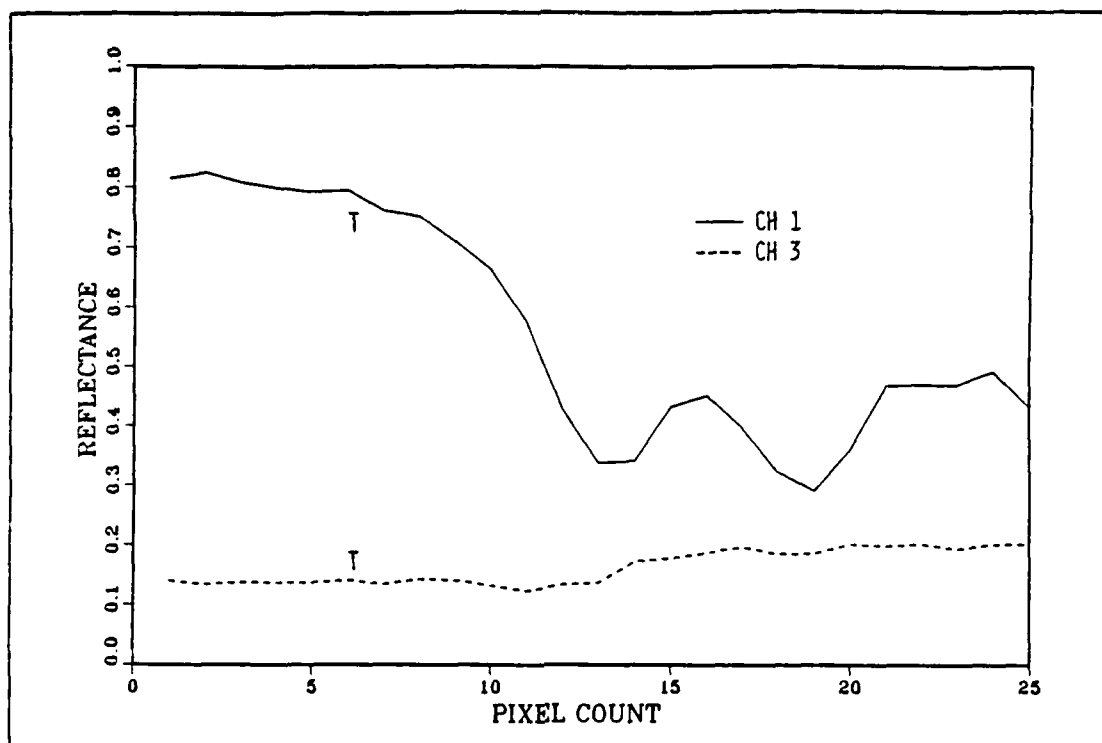


Fig. 54. Reflectance Cross-Section T: Sampled north to south.

this profile. Channel 3 reflectance rises due to the entrainment of sub-saturated air, from 0.12 to 0.2 across the boundary towards the south.

Reflectance cross-section U coincides with the location of the 14 July NCAR Electra mission and is shown in Fig. 55. This cross-section intersects a moderate channel 3 reflectance gradient (refer to Fig. 48). The cellular nature of the stratocumulus clouds in this region is graphically apparent in the channel 1 profile which fluctuates up to 30 percent within the sampled path. Channel 3 increases from an average value of 0.08 in the marine environment to approximately 0.12 across the reflectance boundary, representing a change in cloud droplet modal radius of approximately 1-1.5 μ m based on model cloud reflectance data. The gradient is within the first 30 pixels of the cross-section, with a slight decrease around the 40th pixel.

d. Aircraft Data

(1) *14 July 1987.* Fig. 56 shows the NCAR Electra flight track for the 14 July cloud sampling mission. This track corresponds to reflectance cross-section U, displayed in Fig. 55. The aircraft data are taken in a cloud sampling leg from 2127-2135

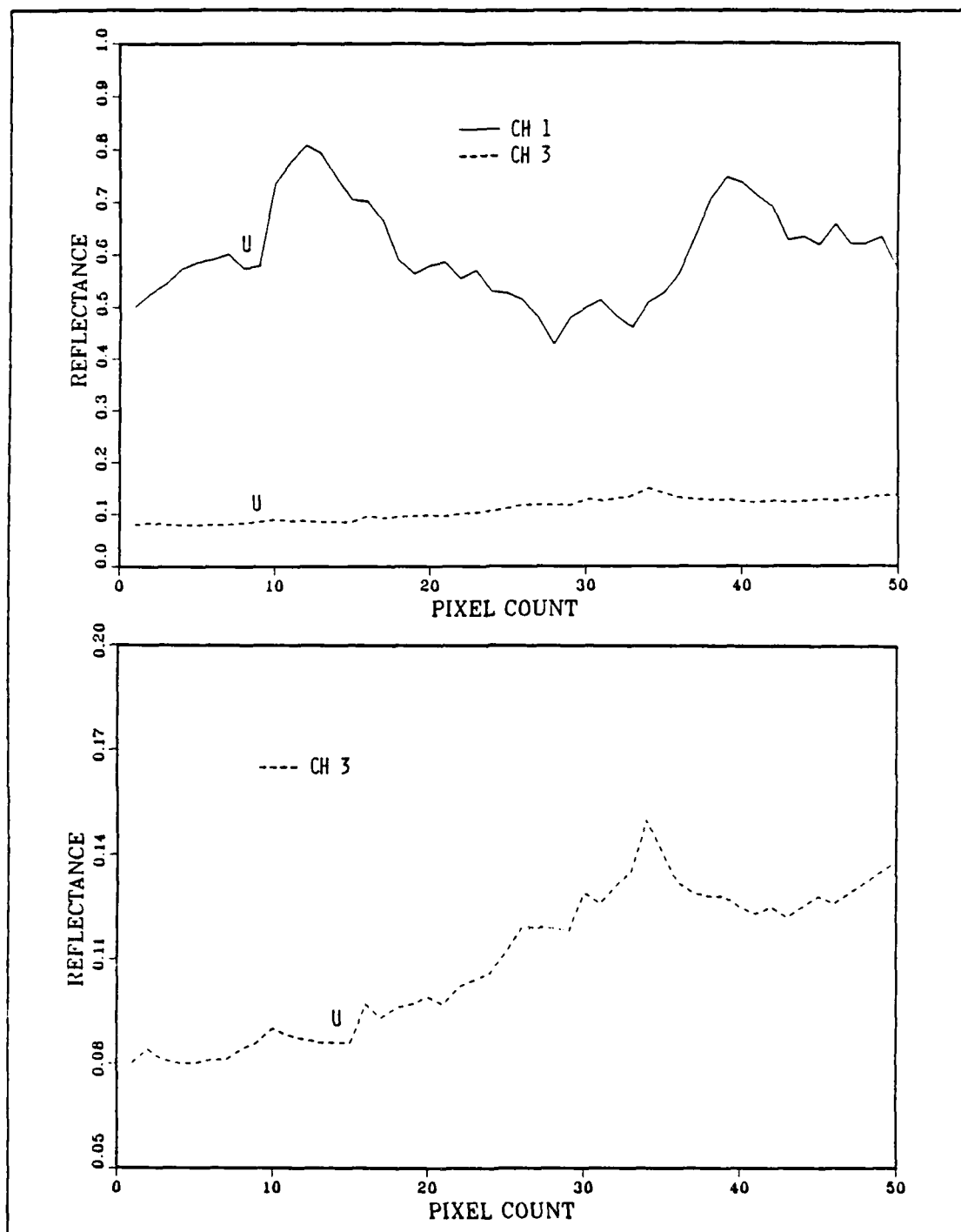


Fig. 55. Reflectance Cross-Section U: Sampled west to east; coincides with location of 14 July NCAR Electra mission.

UTC along a path from point K to point J. The mission was run in a solid stratocumulus cloud layer with the cloud base at 640 meters and the cloud top at an average height of 830 meters. The Electra remained in the upper half of the cloud layer during the sampling run, exiting and reentering the cloud top eleven times (one minute intervals starting at 21:27:20 UTC for three minutes, then eight excursions at approximately 35 second intervals) during the eight minute leg. Table 11 contains the aircraft microphysical data for this leg.

The aircraft measurements reveal a striking gradient in aerosol concentration, from 1550 to 155 per cm^3 . The mean aerosol radius increases in size to the west by $0.01\mu m$. Due to the higher concentration of CCN at point K, the cloud droplet concentration is two and one-half times as large (85 per cm^3) as the concentration at point J (34 per cm^3). The associated mean droplet radius increases toward the marine environment by $1.7\mu m$ within the track. This compares favorably with the reflectance gradient in cross-section U. Fig. 57 shows a comparison of the aircraft track endpoint histograms for cloud droplet and aerosol size distribution. The histograms reveal the change in concentration for both droplets and aerosols across the continental marine interface. The FSSP histogram representing the continental environment shows a higher concentration of small droplets and a smaller modal radius than in the marine regime. The ASASP histograms show the significant increase in small aerosol particles in the continental air at point K.

TABLE 11
SELECTED NCAR ELECTRA DATA FOR 14 JULY 1987

Time (UTC) (± 20 sec)	APN-159 Altitude (m)	PMS-King EQLWC (g/m^3)	ASASP conc. (N/cm^3)	ASASP mean radius (μm)	FSSP conc. (N/cm^3)	FSSP mean radius (μm)
2127	805	0.35	1550	0.105	85	9.9
2128	815	0.30	1050	0.102	62	10.8
2130	795	0.30	450	0.105	44	9.7
2131	825	0.34	270	0.105	61	9.8
2133	825	0.34	200	0.101	58	10.5
2134	820	0.30	175	0.096	40	11.0
2135	825	0.32	155	0.095	34	11.4

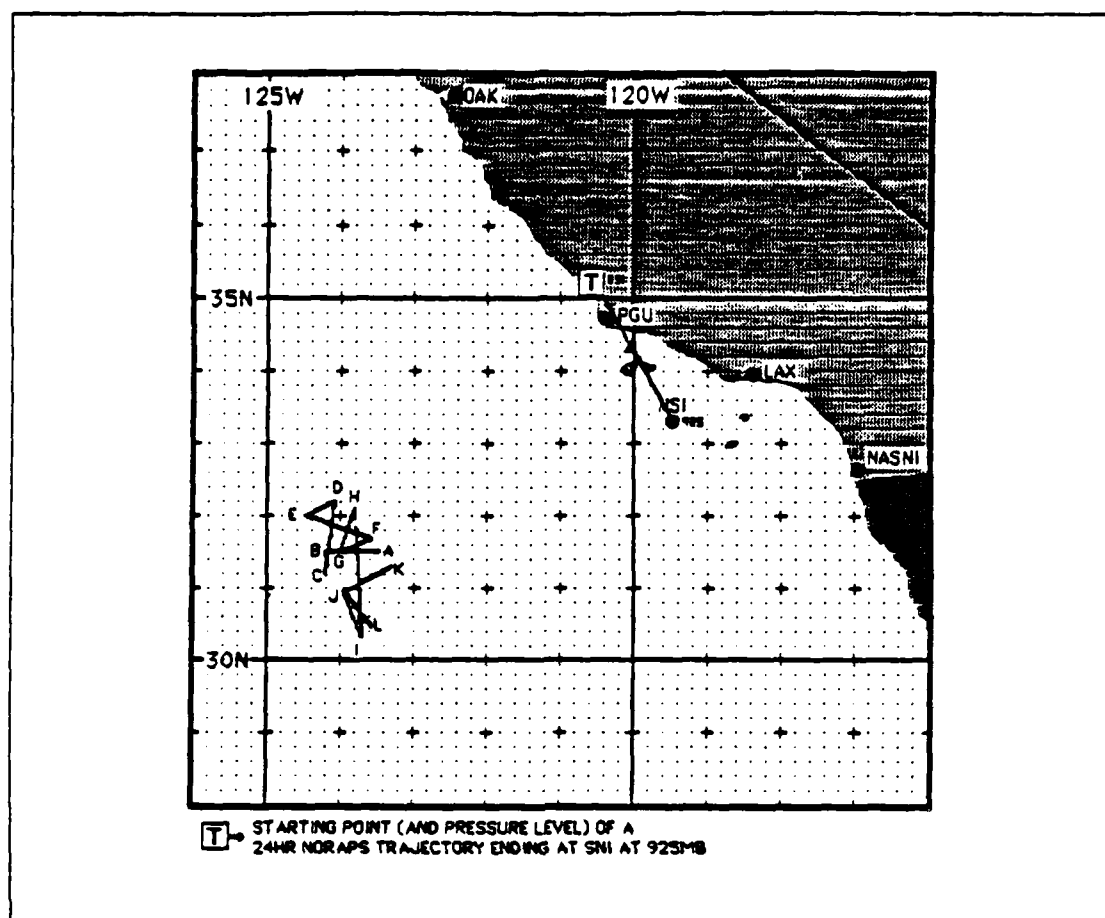


Fig. 56. NCAR Electra Flight Track, 14 July 1987: (from Kloesel *et al.*, 1988).

3. CS3 (6 July)

a. Synoptic Summary

The 500 mb pattern on 6 July, as shown in Fig. 58, is characterized by a weak wave over California imbedded in basically zonal flow. The subtropical high dominates the eastern Pacific with ridges extending into the northwestern U.S. and into the IFO operating area. The thermal trough is at 1007 mb, producing moderate winds out of the north over the CS3 region. A phenomena known as the Catalina Eddy (so called because it usually appears centered near Santa Catalina Island) persists from its formation on the previous day. As discussed by Wakimoto (1987), the cyclonic shear vorticity which appears downstream of the coastal mountains leads to subsidence south of Point Conception and Santa Barbara, while the southerly flow west of San Diego

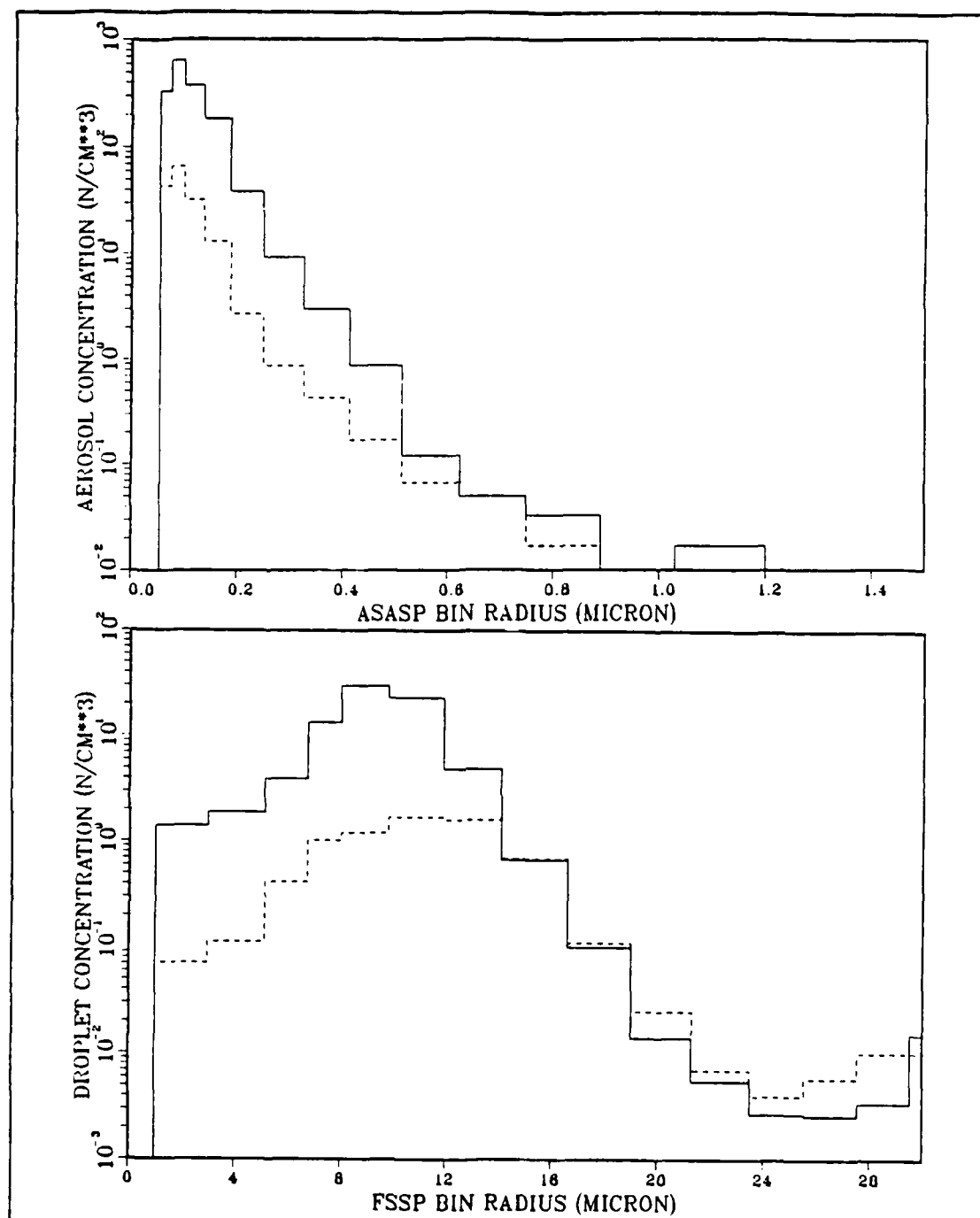


Fig. 57. Size Distribution Histograms for 14 July 1987: ASASP aerosol size distribution (top) and FSSP cloud droplet size distribution (bottom). Dashed lines indicate samples near point J, solid lines represent point K.

experiences convergence and lifting. The eddy has the tendency to ventilate the air in the urban environment over the Los Angeles basin. Fig. 59 shows the 1646 UTC San Nicolas Island rawinsonde sounding and confirms the conditions expected under the influence of subtropical high subsidence and the thermal trough.

b. AVHRR Subscene

A single satellite subscene is generated for CS3 on 6 July; the images are displayed in Figs. 60 and 61. The NOAA-10 satellite subscene has center coordinates of 32°35.2'N 122°33.4'W and crosses latitude 35°N at 15:24:20 UTC on a descending node. The channel 1 image clearly shows a spiral band of clearing south of Point Conception as a result of the subsidence and mixing associated with the Catalina Eddy. The stratocumulus cloud field is aligned in streets revealing the backing nature of the surface wind as it progresses around the west and south sides of the eddy. A tongue of clearing exists to the northwest, extending south and nearly reaching the region of thin stratocumulus seen in the southern extreme of the image. Another clear feature is a frontal zone indicating the morning extent of the diurnal land breeze. As the drier air from the continent meets the general flow over the ocean, upwelling in the MABL creates a line of brighter clouds with an adjacent strip of clouds of lower optical depth to the immediate west. Convergence of southwesterly flow with the frontal zone increases the brightness of the cloud field in the southeast corner of the image.

The channel 3 image reveals a myriad of interesting features. Four clear ship tracks appear in the image, with two more possible tracks just to the west of Point Conception. A double track is found passing through the center and to the southwest. Note that these tracks can still be traced through the more broken stratocumulus to the southwest. A ship appears to have altered course in one case; the right-angled track is found in the southeast portion of the subscene coincident with cross-section L. Areas that are expected to have smaller cloud droplet size distribution due to evaporation and dissipation appear bright, such as in the vicinity of clear areas within the eddy spiral band, around the edges of dry air intrusion in the northwest, and within the stratus deck over the Los Angeles basin. The complexity of the flow regime east of a line connecting San Miguel, San Nicolas, and San Clemente Islands due to the land breeze and the Catalina Eddy is very evident in the channel 3 image. The land breeze frontal zone appears as expected from an examination of the visual imagery. The upwelled areas may be darker as a result of larger cloud droplets, while the brighter region is consistent with

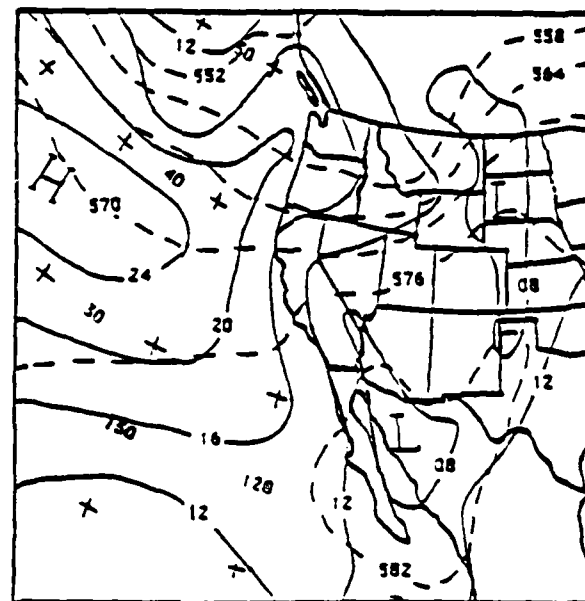
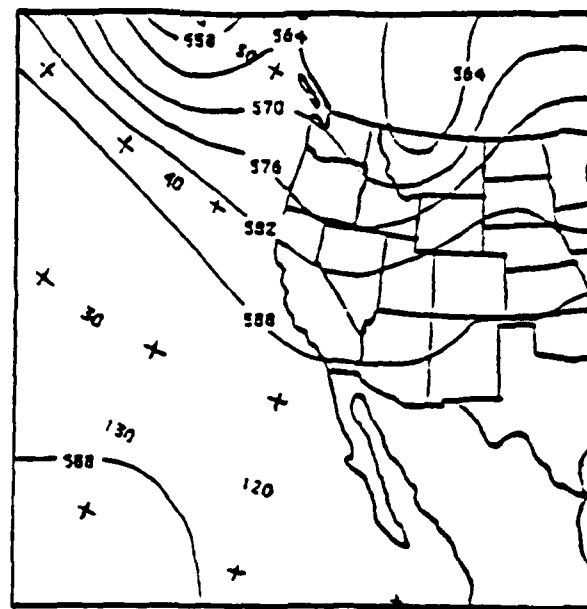


Fig. 58. 6 July 1987 12 UTC Regional OI Analysis: 500 mb heights (top) and surface pressure/1000-500 mb thickness (bottom).

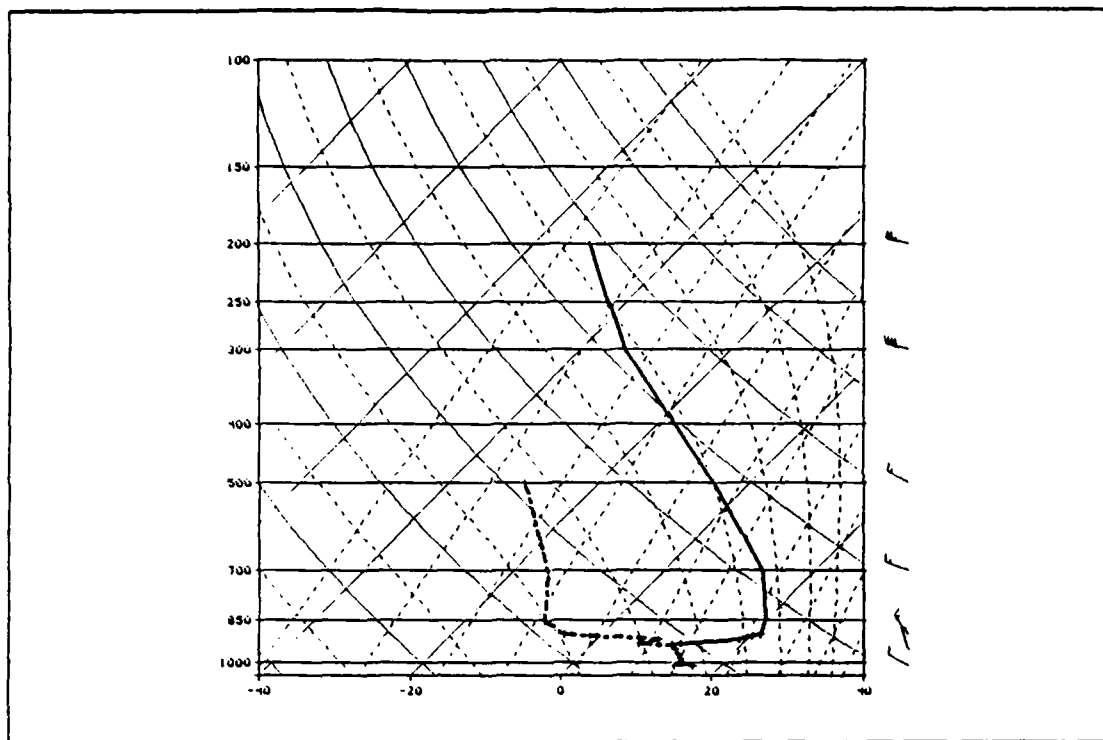


Fig. 59. San Nicolas Island Rawinsonde Sounding: 6 July 1987 1646 UTC.

smaller droplet spectra and the influence of continentally influenced aerosols in this region.

c. Reflectance Cross-Sections

Fig. 62 displays the reflectance across the land breeze frontal feature, identified as I in the images. Channel 1 reflectance drops abruptly at the frontal interface, from approximately 0.85 to 0.42, and then rises past its original brightness over the next 30 pixels. Reflectance in channel 3 rises from an average of 0.27 to 0.35 across the interface.

Reflectance values for cross-section J are shown in Fig. 63. This profile intersects two small clear regions within the Catalina Eddy spiral feature. The rise and fall in channel 3 reflectance at cloud edges from decreasing droplet size and decaying cloud optical depth, respectively, is obvious in the channel 3 profile and is similar to that observed in previous case studies. The rise in reflectance in both channels due to a ship track is evident at the fifth pixel.



Fig. 60. NOAA-10 AVHRR 1524 UTC 6 July 1987 Channel 1: Line segments indicate reflectance cross-sections I through L. Center coordinates 32°35.2'N 122°33.4'W.



Fig. 61. NOAA-10 AVHRR 1524 UTC 6 July 1987 Channel 3 Reflectance: Line segments indicate reflectance cross-sections I through L. Center coordinates 32°35.2'N 122°33.4'W.

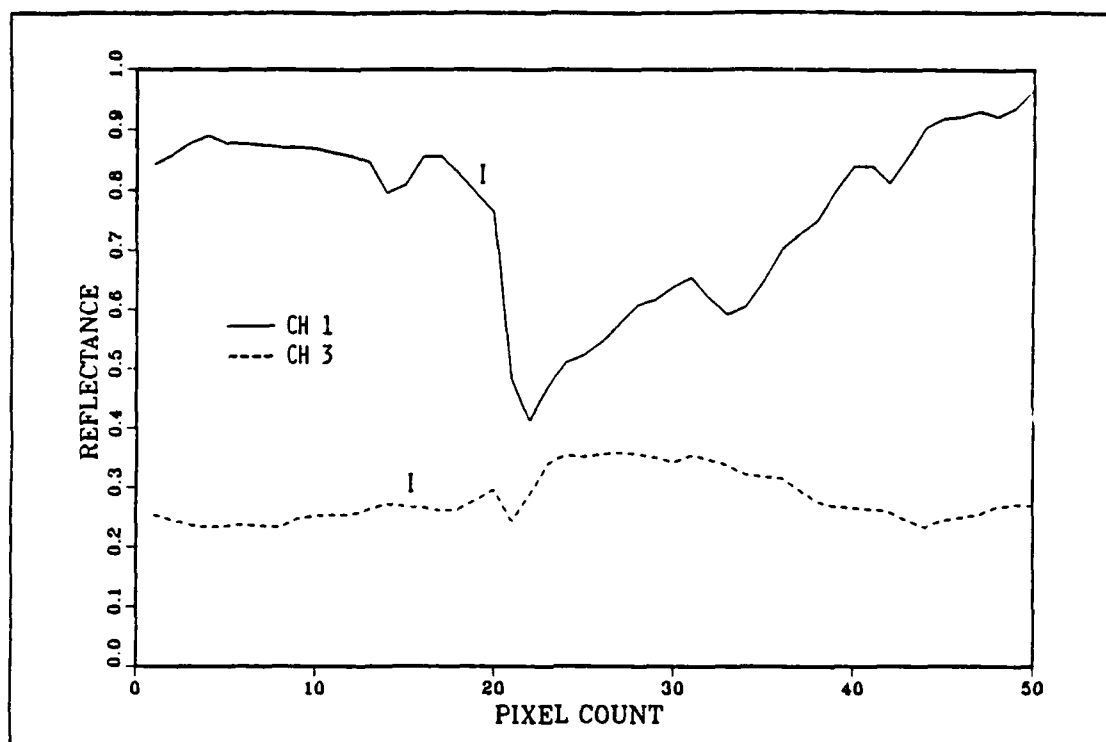


Fig. 62. Reflectance Cross-Section I: Sampled west to east.

Fig. 64 shows two relatively short (25 pixel) cross-sections, labeled K and L. Cross-section K provides reflectance data for the region near the clear intrusion in the northwest portion of the subscene, and intersects a strong ship track (0.08 rise in channel 3 reflectance). The channel 3 profile shows a peak near the cloud edge at the tenth pixel and a decrease to the cloud edge between the fourth and ninth pixels, consistent with other case studies. Cross-section L bisects another ship track, and displays a 0.05 rise in channel 3 reflectance at the ship track position. Both ship tracks in Fig. 64 have less of a signature in channel 1 than the ship tracks seen in the previous case studies.

4. CS4 (18 July)

a. Synoptic Summary

The west coast at 500 mb is being influenced by a deepening wave centered at 43°N 120°W, shown in Fig. 65. The 1037 mb subtropical high is located near the same latitude at 147°W, while thermal troughing is nearly nonexistent. The decay in subsidence strength in association with the trough aloft is reflected in the rawinsonde

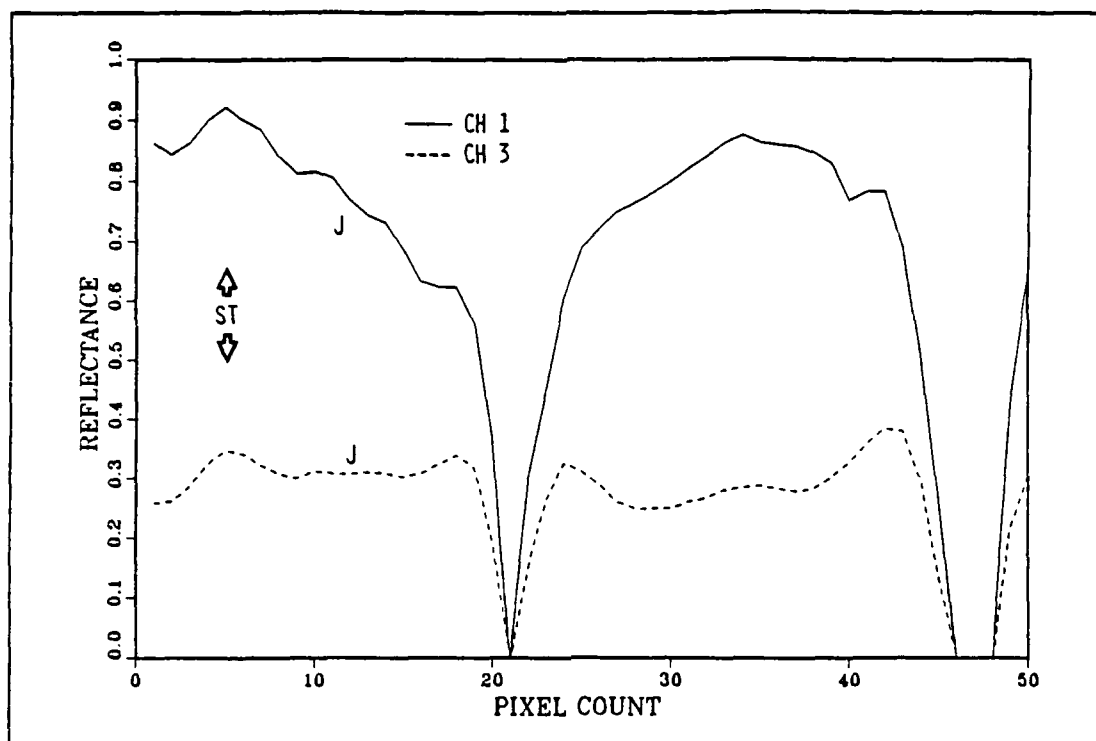


Fig. 63. Reflectance Cross-Section J: Sampled west to east; ST denotes position of ship track.

sounding from Vandenburg Air Force Base shown in Fig. 66. The products of these synoptic ingredients are moderate northwesterly flow and scattered/broken cloudiness within the operating area. These conditions are optimum for examining the reflectance characteristic of individual cloud elements.

b. AVHRR Subscene

The satellite subscene images for CS4 are displayed in Figs. 67 and 68, and originate from the NOAA-10 decending pass crossing 35°N at 16:04:20 UTC. The subscene center coordinates are 35°16.8'N 124°12.4'W. The channel 1 image reveals a solid field of large cloud cells in the western portion of the subscene. A band of clouds appears near subscene center, with small, individual cells south of this feature. Closer to land, the cloudiness is thinner and less well-defined, with evidence of gravity waves propagating within the field. The individual cells, as expected, appear bright in channel 1 near the center and decrease in brightness towards the cloud edge. The cloud boundaries are apparent in channel 3 where they are defined by high reflectance.

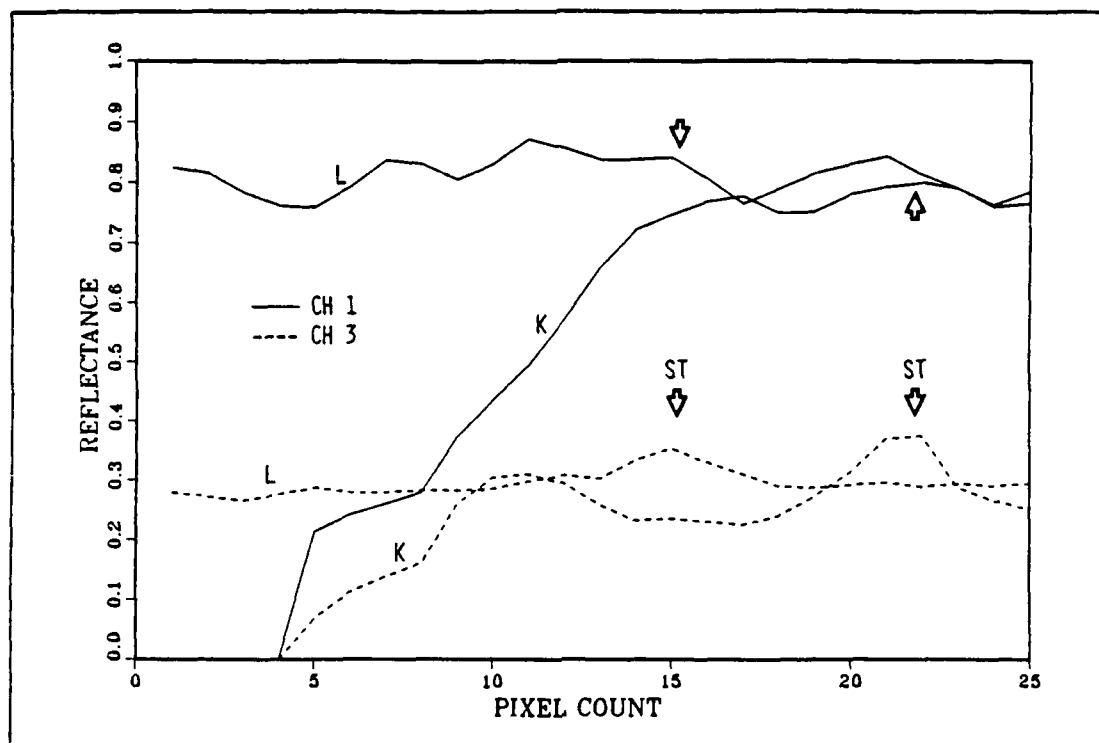


Fig. 64. Reflectance Cross-Sections K and L: Cross-section K sampled west to east; L sampled north to south. ST denotes position of ship track.

c. Reflectance Cross-Sections

Figs. 69 and 70 display two-dimensional reflectance cross-sections within the 18 July subscene, identified as V and W, respectively. These cross-sections encompass individual cloud cells in the region of scattered cloud elements south of the subscene center. Two discrete cells are within cross-section V, while cross-section W highlights a single element. Channel 1 reflectance peaks near the center of each element, and decreases towards the edge as EQLWC and optical depth decrease. McKee and Klehr (1978) shows that cloud microphysical properties have a relatively small effect on reflectance in visible wavelengths compared to variations resulting from cloud geometry. Based on this study and the conclusions drawn from model cloud reflectances, it is clear that changes in cloud thickness and EQLWC are responsible for most of the drop in reflectance towards the cloud edge in both channel 1 cross-sections.

In channel 3, reflectance increases towards the cloud edge away from the element center at all azimuths until at the edge where there is a short decrease. These

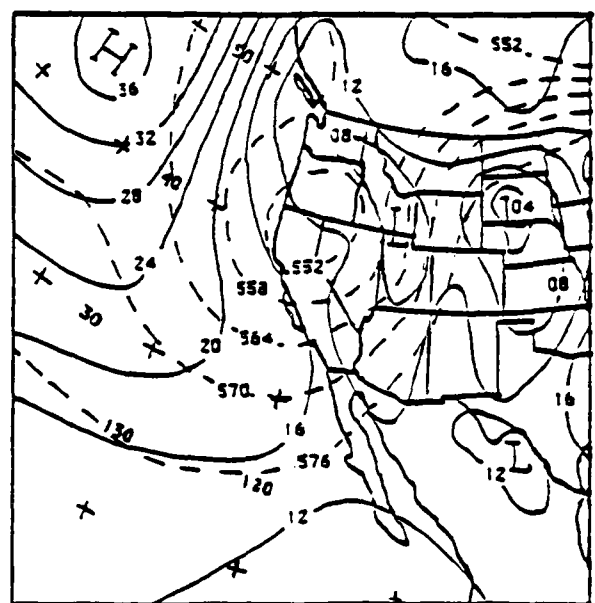
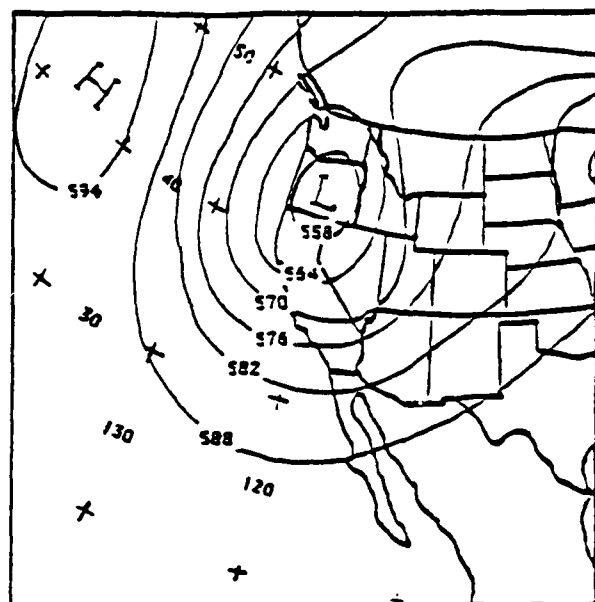


Fig. 65. 18 July 1987 12 UTC Regional OI Analysis: 500 mb heights (top) and surface pressure/1000-500 mb thickness (bottom).

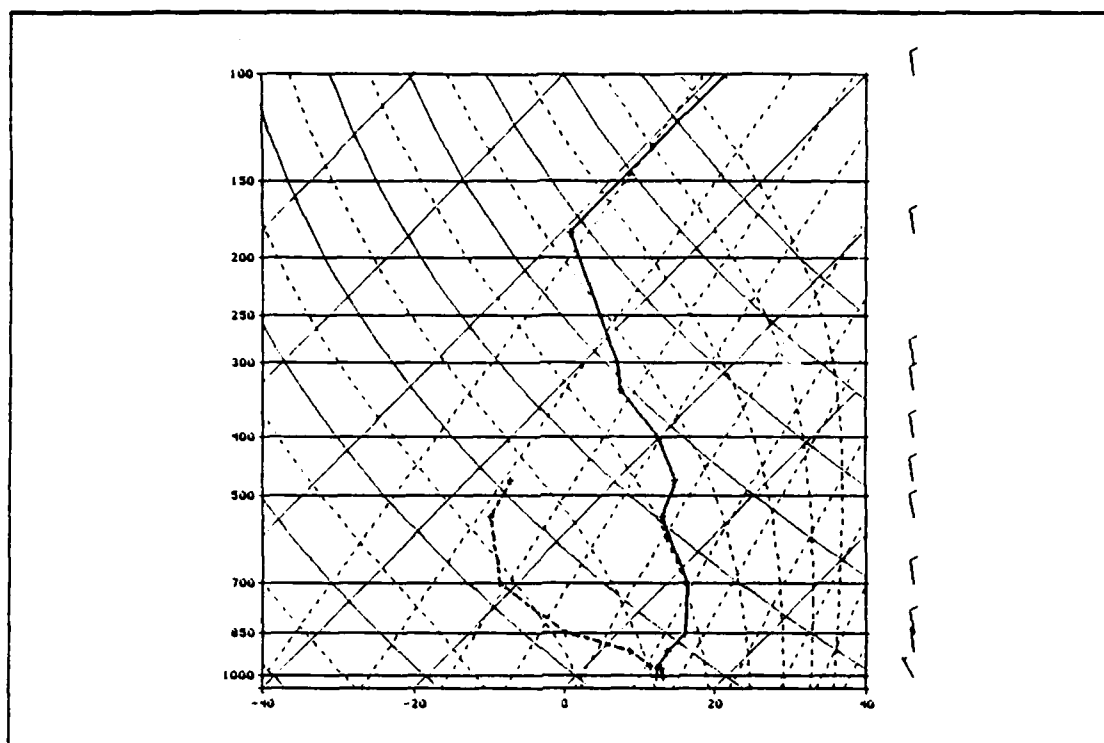


Fig. 66. Vandenburg AFB Rawinsonde Sounding: 18 July 1987 1200 UTC.

effects have been shown in previous cross-sections and may result from the decrease in cloud droplet size with decreasing distance from the cloud edge, except at the immediate edge where the loss of optical depth dominates the microphysical effect. Coakley and Davies (1986) illustrates that increases in channel 3 reflectance at cloud edges may be due to two factors: directionally dependent reflectance from cloud sides and cloud-sun geometry, and variations in cloud droplet size distribution. The solar zenith angle at the two cross-sections is approximately 67° ; if cloud geometry were dominating the channel 3 reflectance variations there should be a strong azimuthal dependency of reflectance circumscribing a cloud element near the solar azimuth angle axis (approximately 106° from north). Although some evidence of this effect is visible in the location of the channel 1 reflectance maxima in cross-section V, the effect is not apparent in either cross-section in channel 3. Based on this, the results of CS4 indicate that the cloud droplet size distribution gradient near the cloud edge may be the source of a majority of the reflectance increase near the cloud edge in scattered stratocumulus/cumulus clouds.

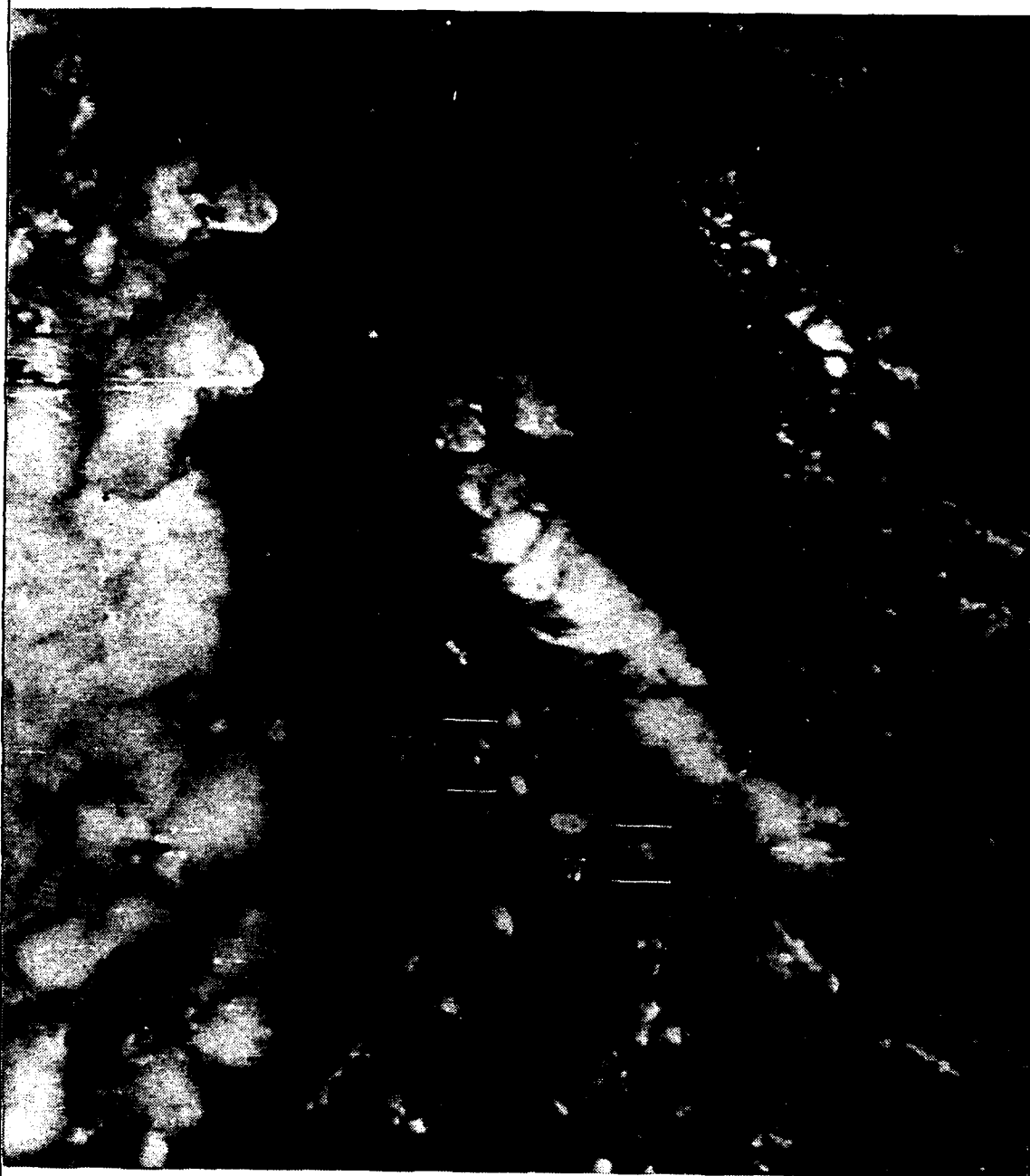


Fig. 67. NOAA-10 AVHRR 1604 UTC 18 July 1987 Channel 1: Boxes indicate two-dimensional reflectance cross-sections V and W. Center coordinates $35^{\circ}16.8'N$ $124^{\circ}12.4'W$.



Fig. 68. NOAA-10 AVHRR 1604 UTC 18 July 1987 Channel 3
Reflectance: Boxes indicate two-dimensional cross-sections V and W.
Center coordinates 35°16.8'N 124°12.4'W.

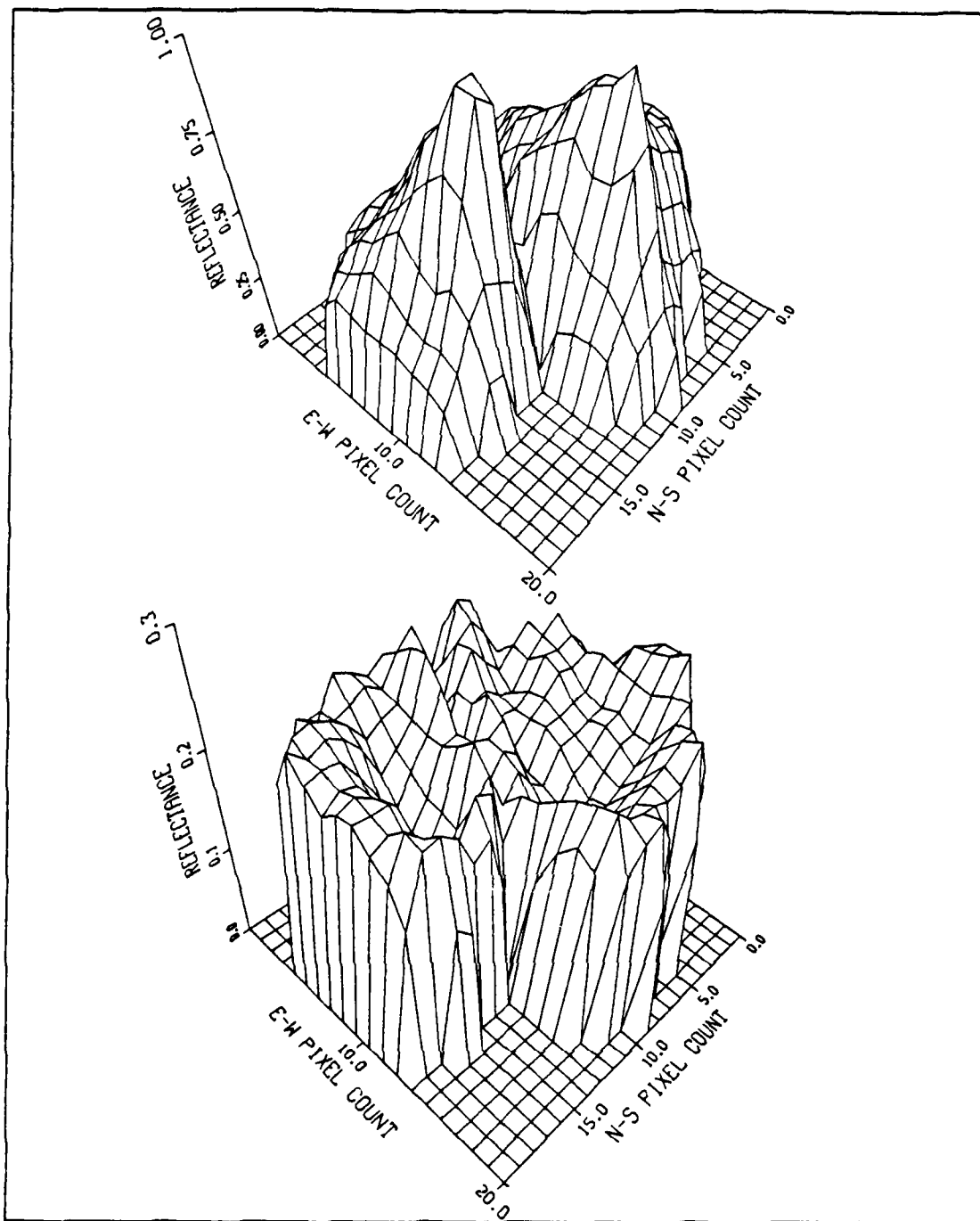


Fig. 69. Two-Dimensional Reflectance Cross-Section V: Channel 1 (top) and channel 3 reflectance (bottom). 2-D pixel origin is to the northwest.

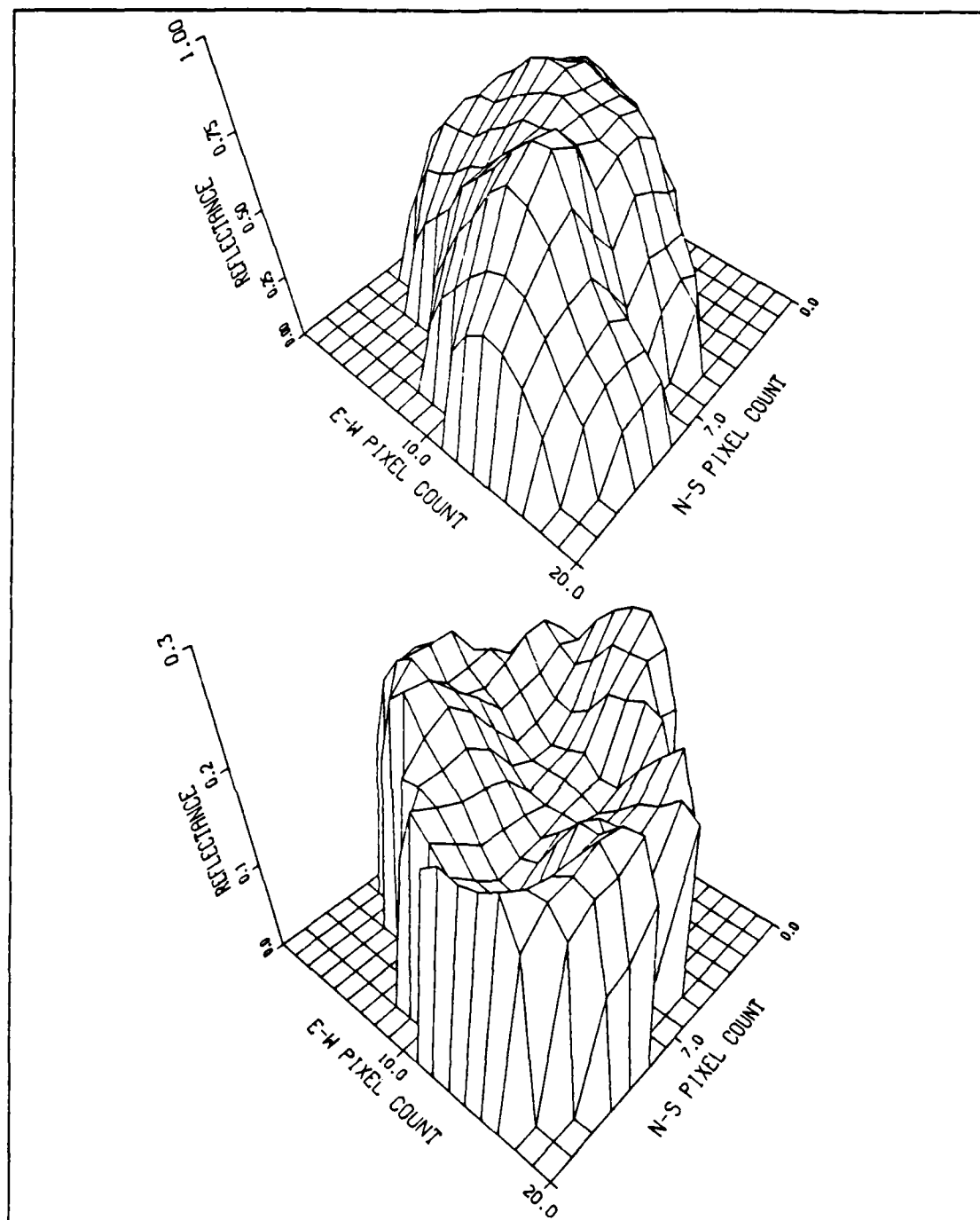


Fig. 70. Two-Dimensional Reflectance Cross-Section W: Channel 1 (top) and channel 3 reflectance (bottom). 2-D pixel origin is to the northwest.

Three individual cloud elements of 10-15 pixel radius are selected in the vicinity of the aircraft mission track, below the southern boundary of the 18 July subscene. This element size is selected in order to approximate the cloud cell from which aircraft measurements are sampled (as illustrated in the next section). Pixel values in these three elements are identified from cloud edge to cloud center, and the resulting reflectances are averaged over eight azimuth angles and all elements. These values are combined into an average cloud reflectance along a line segment from cloud edge to cloud center. An examination of this element "average" reveals channel 1 reflectance values of approximately 0.25, 0.61, 0.75, and 0.9 for four equal segments along the radius line, from cloud edge to cloud center. Channel 3 reflectance averages 0.18 at the cloud edge, increasing to 0.29 immediately inside the cloud edge, with a near-linear decrease to 0.23 in the vicinity of the cloud element center.

d. Aircraft Data

(1) 18 July 1987

TABLE 12 SELECTED NCAR ELECTRA DATA FOR 18 JULY 1987						
Time (UTC) (± 20 sec)	APN-159 Altitude (m)	PMS-King EQLWC (g/m^3)	ASASP conc. (N/cm^3)	ASASP mean radius (μm)	FSSP conc. (N/cm^3)	FSSP mean radius (μm)
1453	935	0.22	800	0.085	71	4.0
1454	930	0.29	900	0.090	63	6.0
1454	935	0.16	750	0.090	76	5.3
1517	980	0.16	420	0.095	53	3.1
1517	1050	0.24	405	0.095	75	5.3
1519	1090	0.27	495	0.092	88	6.2
1521	1140	0.29	480	0.096	111	7.2

The flight track for the 18 July NCAR Electra mission is found in Fig. 71. In the vicinity of the aircraft track, cloud bases and average cloud tops were at altitudes of 900 and 1150 meters, respectively. Due to the difference in time between aircraft in-cloud sampling and the NOAA-10 overpass, a one-to-one match with a particular element is not attempted. Since the intent of CS4 is to examine the reflectance properties of individual cloud elements, the aircraft data are examined in order to locate

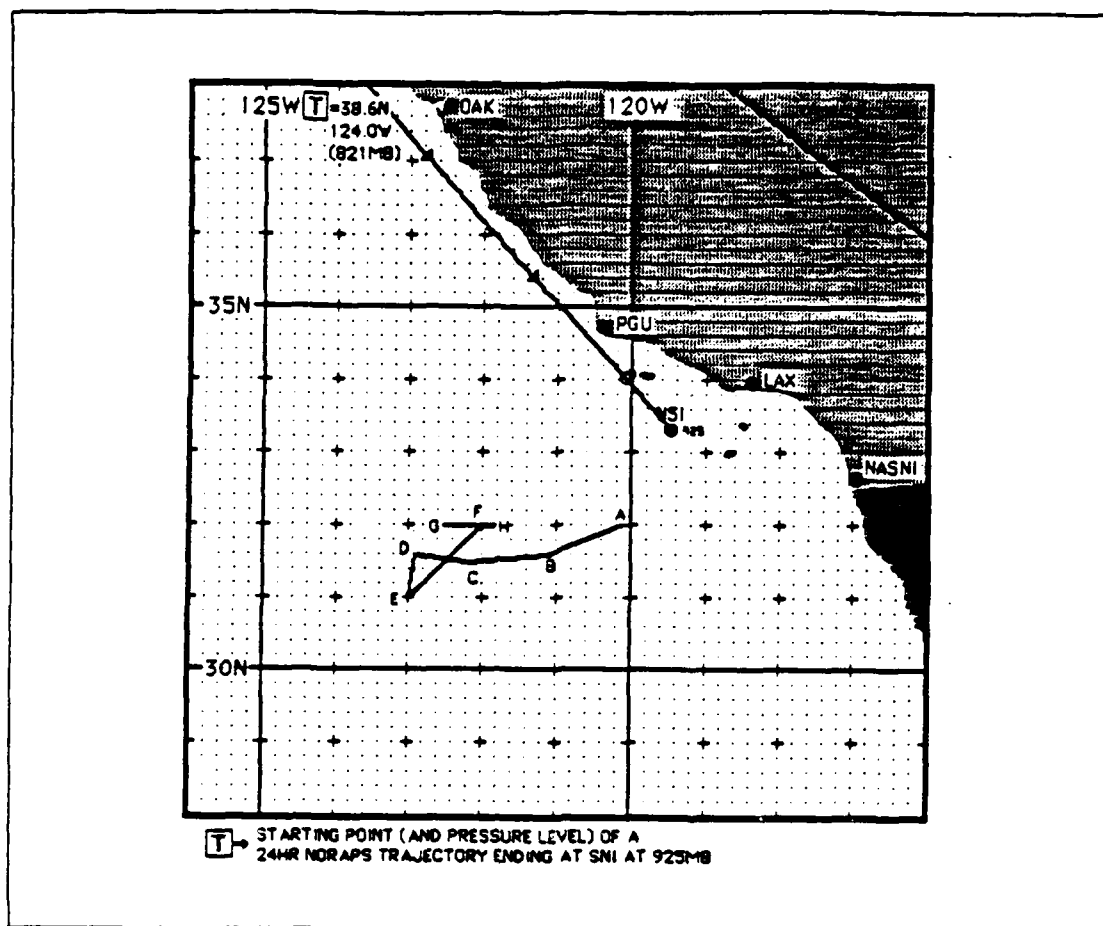


Fig. 71. NCAR Electra Flight Track, 18 July 1987: (from Kloesel *et al.*, 1988)

sampling tracks that intersect these elements. The cloud microphysical data found in Table 12 is acquired from the aircraft track between points G and H, during an in-cloud turbulence leg from 1452-1500 UTC and from a cloud sounding leg from 1511-1523 UTC. In the first leg, a small cloud element is penetrated at an altitude of 940 meters, with the aircraft entering the element at 14:52:55 UTC and exiting the other side at 14:54:20 UTC. In the second leg, the sounding profile intersects a larger cloud element and provides cloud samples from a point near the cloud edge (980 meter altitude at time 15:16:50 UTC) to a region near the element center (1140 meter altitude at time 15:20:20 UTC) at vertical positions immediately below the cloud top.

Both samples indicate decreases in mean droplet size near the cloud edge. Since the size of the element sampled in the sounding leg is representative of the

elements from which reflectance data were derived in the previous section, the droplet size data from this leg will be used for comparison with averaged channel 3 reflectances from CS4. The short duration of in-cloud time for the first sampling leg and the rapid change of cloud microphysical properties with time prevent the one-minute averages of droplet/aerosol concentration in the histograms from providing useful information about the cloud structure. The first leg reveals the expected decrease in cloud droplet size, concentration, and EQLWC near the edge of the cloud, while the aerosol parameters remain relatively unchanged. Histograms for the cloud edge and the cloud interior in the second sampling leg are shown in Fig. 72. The changes in cloud droplet size distribution across the cloud element are clearly evident. As expected, the distribution of aerosols at both locations are nearly identical, while the droplet distribution shows an unmistakable shift toward smaller droplet sizes near the cloud edge. The absence of large cloud droplets and the concentration of aerosol particles indicate that the sampled cloud elements are within continentally influenced air.

5. Reflectance Analysis

In order to correlate the cloud droplet size data from the NCAR Electra with reflectance data from applicable NOAA-9/10 subscenes, the aircraft samples listed in Tables 9 through 11 are examined to determine the samples that coincide with the approximate location of reflectance cross-section data. When a match is identified, a ten-pixel average of reflectance centered near the coincident pixel is performed. This average reflectance value is utilized to make comparisons with the cloud microphysical data. The limits of uncertainty represent a 95% confidence (within two standard deviations) in the value of reflectance along the pixel average, and in the droplet size determination. The uncertainty of droplet size values are a function of the variability and noise contained in the aircraft data. In the case of the 18 July case study, the cloud element averages identified in the previous section are correlated to the aircraft sounding data contained in Table 12.

The results of the intercomparisons are displayed in Fig. 73. As expected, there is little correlation between reflectance and cloud droplet size in channel 1 since the magnitude of reflectance in this portion of the electromagnetic spectrum is heavily dependent upon cloud thickness and EQLWC, as well as the droplet size distribution. The four data points between 3 and 7 μm represent individual cloud element averages from CS4. The data show an increase in reflectance as larger droplets are encountered in the interior of the cloud element where greater EQLWC and cloud thickness exists. The

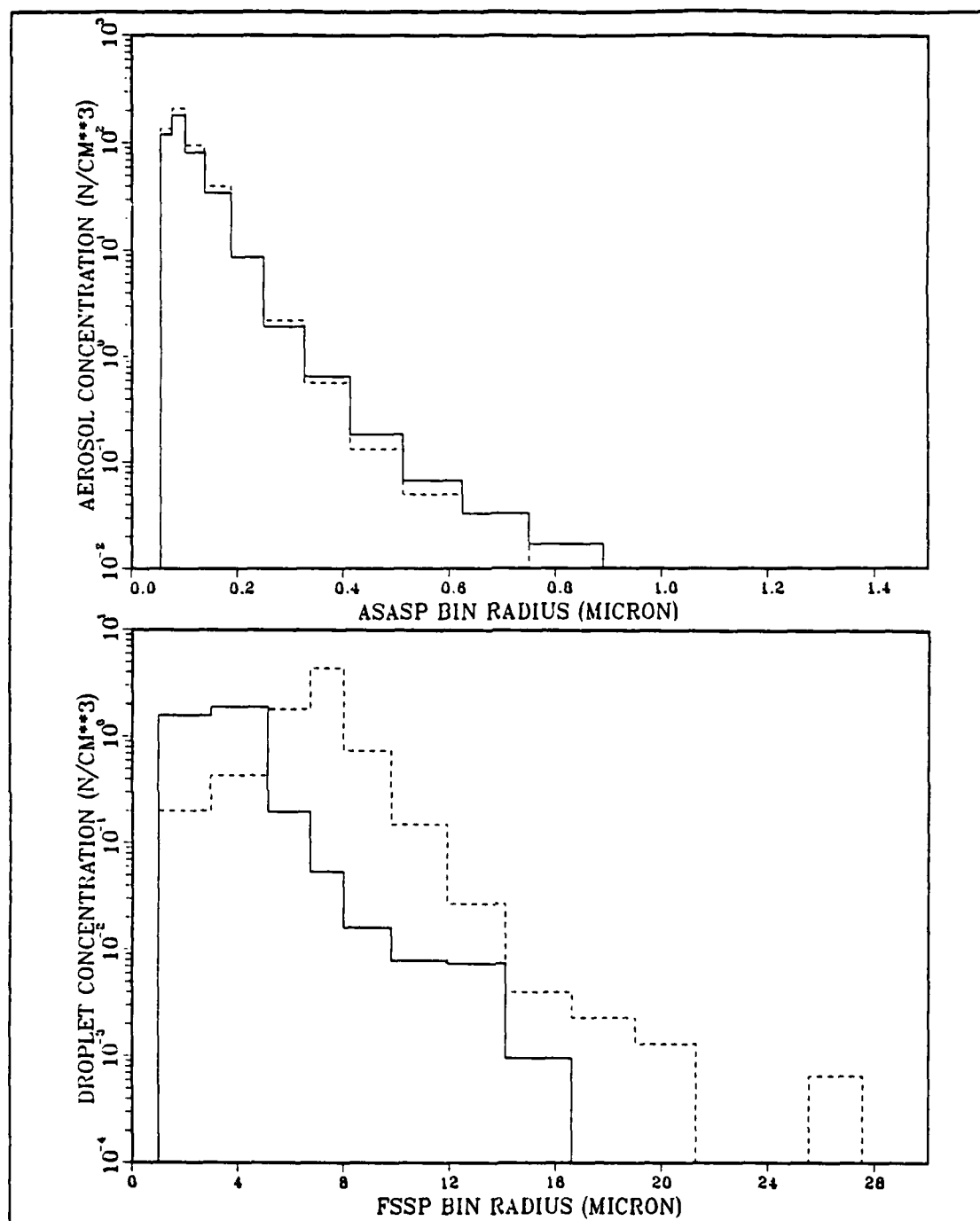


Fig. 72. Size Distribution Histograms for 18 July 1987: ASASP aerosol size distribution (top) and FSSP cloud droplet size distribution (bottom). Dashed lines indicate samples near cloud element interior, solid lines represent the cloud edge regime.

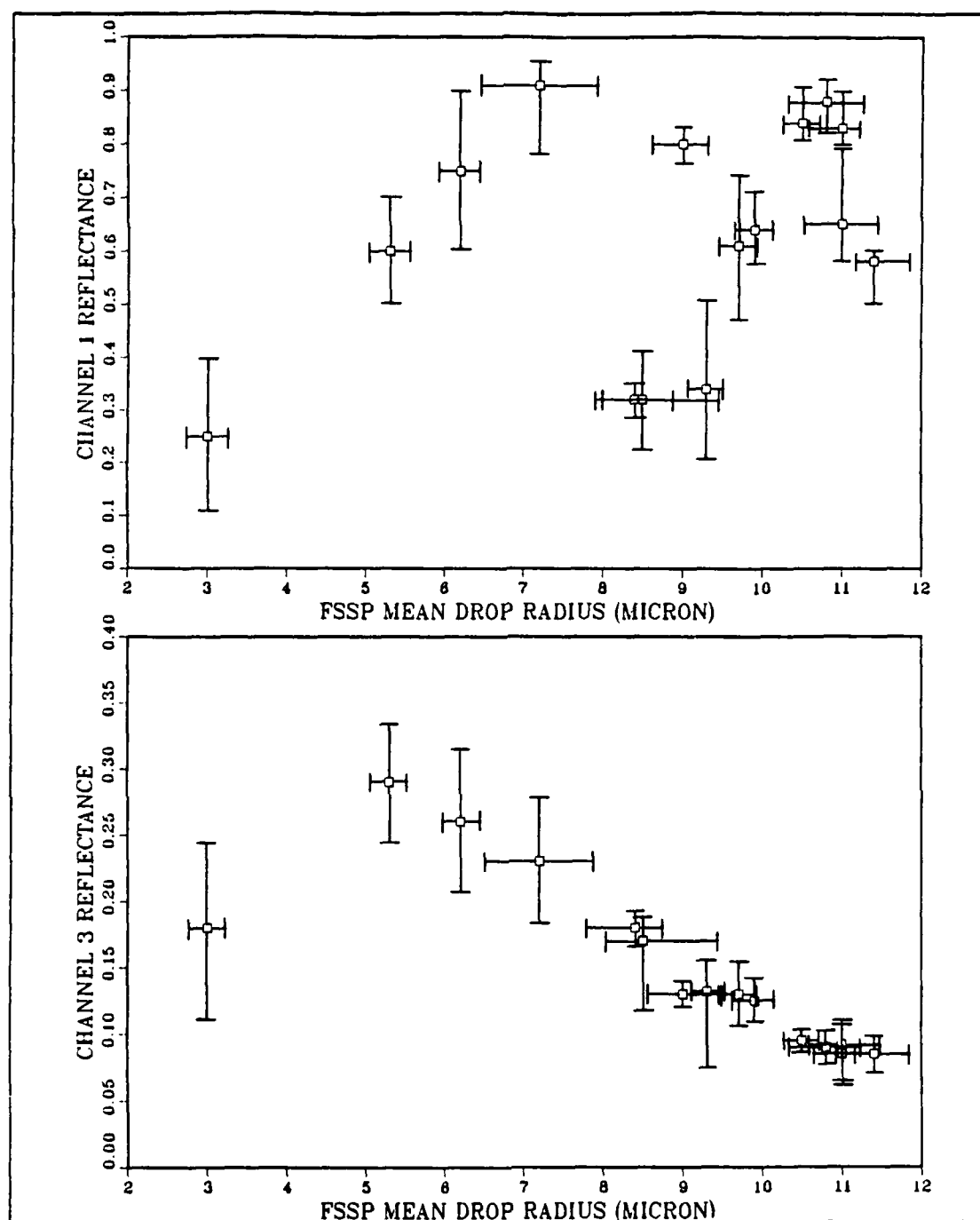


Fig. 73. Reflectance verses FSSP Mean Droplet Radius: Channel 1 (top) and channel 3 (bottom). Brackets indicate 95 percent confidence intervals for reflectance and mean radius.

channel 3 reflectance displays a near-linear correlation with cloud droplet size. The outlying data point at $3\mu\text{m}$ represents the CS4 cloud element edge, where the decrease in cloud thickness and its associated effect on the optical depth is dominating the microphysical effect on reflectance. A review of the aircraft data indicates that the cloud thickness for this element edge sample is less than 80 meters, and the EQLWC is almost half of that found in the cloud interior (0.16 g/m^3 versus 0.29 g/m^3).

Fig. 74 relates channel 1 reflectance to cloud thickness. Cloud thickness values are estimated from APN-159 radar altimeter and PMS-King EQLWC data. The estimations may vary from actual cloud thicknesses by several tens of meters since aircraft measurements must be interpolated horizontally in certain aircraft mission data. The data show increasing channel 1 reflectance with increasing cloud thickness, which is consistent with the dependence on optical depth at this wavelength. Although channel 1 reflectance should vary as a function of droplet radius with constant cloud thickness and EQLWC, there are insufficient data to observe this variation.

Fig. 75 compares the channel 3 results with the model cloud reflectance data discussed and illustrated in Chapter II. Noonkester (1984) showed that the cloud droplet distribution modal radius is, on the average, approximately $1\mu\text{m}$ larger than the mean droplet radius; this is consistent with the NCAR Electra data utilized in this thesis. The difference between droplet distribution modal radius (used in model reflectances) and droplet distribution mean radius (obtained from the aircraft data) adds a small degree of uncertainty to the data in Fig. 75, and is considered in the definition of the region of uncertainty. The model case with a cloud thickness of 250 meters and EQLWC of 0.4 g/m^3 is the most representative of the conditions specified in the model reflectance data in Chapter II. For this comparison, three additional model reflectances were generated for a droplet modal radius of $12\mu\text{m}$ in order to compare delta-Eddington approximations with the aircraft and reflectance data at larger droplet sizes. As seen in Fig. 75, a majority of the region of uncertainty falls within the region defined by the three model cloud droplet distributions. The shift toward model distribution D1 at large droplet sizes and the shift toward model distribution D2 at the smaller droplet sizes is consistent with the shift in distribution shape measured by the aircraft and illustrated in Figs. 33 and 57. Based upon the trend observed at large droplet radii, the relationship between droplet size and channel 3 reflectance will continue to asymptotically approach a reflectance value of zero for droplet radii larger than the largest mean droplet radius measured in the case studies.

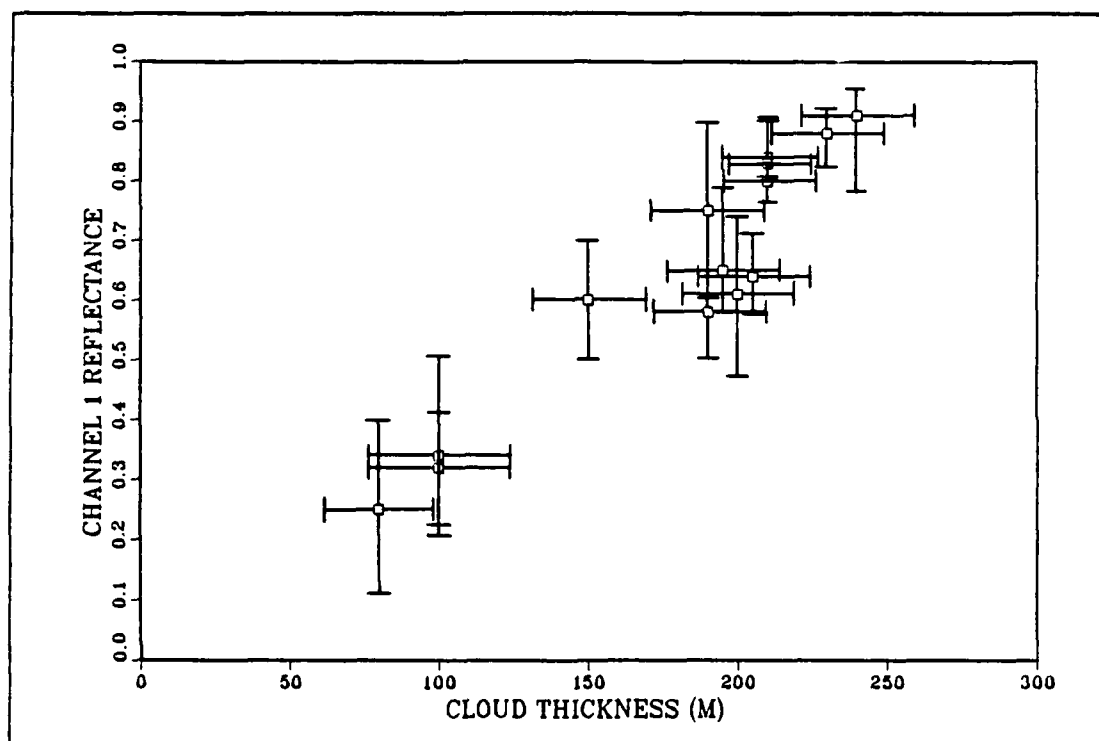


Fig. 74. **Channel 1 Reflectance versus Cloud Thickness:** Cloud thicknesses estimated from APN-159 radar altimeter and PMS-King EQLWC data. Brackets indicate 95 percent confidence intervals for reflectance and cloud thickness.

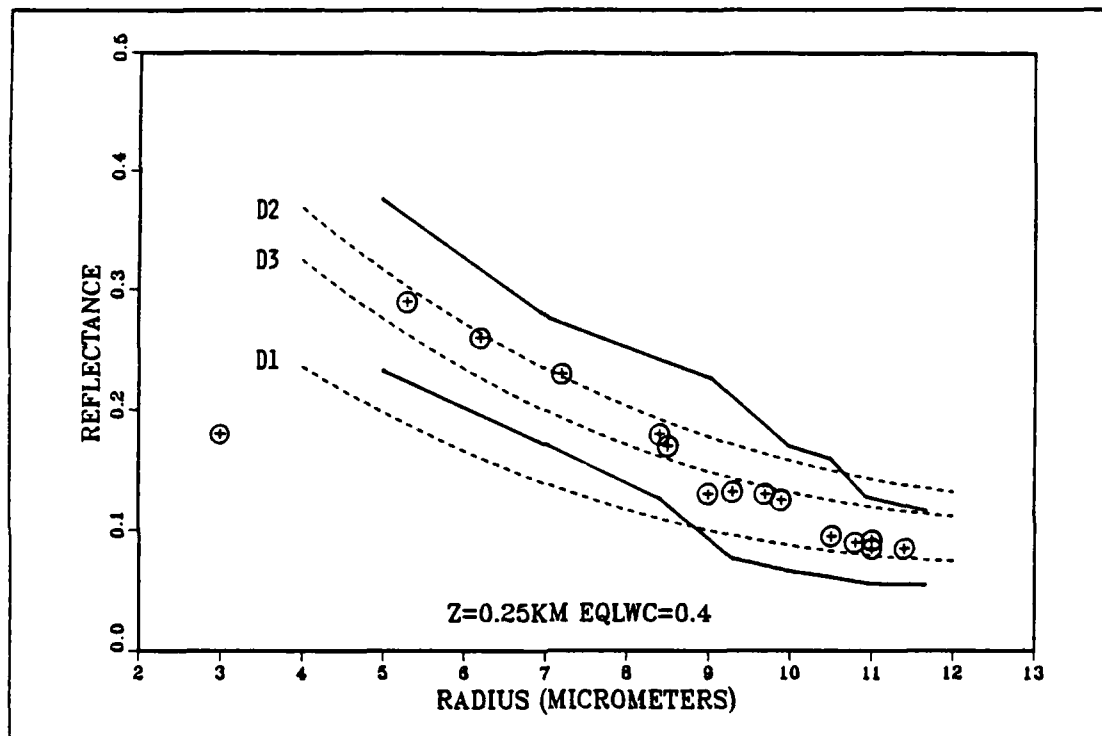


Fig. 75. Channel 3 Reflectance versus Droplet Radius: Dashed lines indicate model cloud reflectance for droplet distributions D1, D2, and D3; solid lines indicate 95 percent confidence interval for data points.

V. CONCLUSIONS AND RECOMMENDATIONS

A. CONCLUSIONS

The relationship between solar reflectance and cloud droplet size distribution has been illustrated by comparing AVHRR satellite data and aircraft measurements. The expected relationship of higher reflectances from smaller cloud droplet size spectra is confirmed by the four case studies presented in this thesis. In the case of continental/marine air mass differences, higher channel 3 reflectivities are associated with higher concentrations of aerosols, higher concentrations of cloud droplets, and a shift towards a smaller mean cloud droplet radius. In the case of individual cloud elements, higher channel 3 reflectivities are associated with a strong shift towards a smaller mean droplet radius, even though EQLWC and droplet concentration decrease and the aerosol concentration remains relatively unchanged. The strength of channel 1 reflectance provides a measure of optical depth, ensuring that it is sufficiently "thick" to allow deductions of cloud properties from channel 3 measurements. The strong dependence of channel 3 reflectance on cloud droplet size distribution allows inference of cloud composition characteristics from satellite data. This dependence is closely approximated by model cloud reflectances based on Mie theory and the delta-Eddington approximation. Assuming that the MABL is well-mixed, the satellite reflectance data provide an indication of the concentration and nature of the aerosol distribution below the cloud layer.

Regions of continental air mass influence over the ocean may be generated by synoptically forced offshore flow over the western coast of the U.S. and Canada, and may be advected with the wind field. These regions may vary in their concentration of continental aerosols and associated CCN (and mean cloud droplet size) from the strength of the offshore flow, as well as the duration of time that this flow persists prior to it being replaced by the climatological northwesterly flow from marine sources. The continental/marine air mass interface identified in the satellite data seems to be advected at a rate slightly slower than the wind forcing, suggesting that some mixing of aerosols persists across the interface. The 1550 per cm^3 aerosol concentration measured at a point approximately 300 n mi from the coastline in CS2 indicates that significant concentrations of continental aerosol have the potential to be advected far offshore and affect the reflectance of stratocumulus cloud fields over thousands of square miles.

The stratocumulus cloud fields within the continental influence may appear more continuous and less broken than clouds within the marine influence under similar conditions. In several cases, continental-marine interfaces identified in channel 3 reflectance imagery can be located utilizing the variations observed in channel 1.

Although model cloud reflectance calculations suggest that continentally influenced clouds should increase in brightness in channel 1 as well as channel 3, these regions appear less bright than the marine stratocumulus in the visible. Measurements of cloud top EQLWC in both air mass regimes indicate relatively constant values (near 0.31 g/m^3) which are consistent with those observed by Noonkester (1984). Only cloud-edge measurements give significantly lower levels of EQLWC. It appears that changes in stratocumulus cloud thickness and horizontal cloud coverage occur in cloud fields modified by the addition of continental CCN, so that the scattering optical depth is reduced in the continental regime. This reduces the reflectance in channel 1 but does not affect channel 3 reflectance for stratocumulus clouds of sufficient thickness (> 100 meters). The model reflectance calculations seem to hold true for ship effluent tracks, where increased reflectivity in both satellite channels is observed.

Cloud elements surrounded by sub-saturated air exhibit a characteristic signature in channel 3 reflectance. This signature is consistent with horizontally varying droplet size distribution and optical depth. The channel 3 reflectance increases from the cloud element center to the cloud edge where the greatest entrainment of ambient air is taking place. The reflectance decreases at the immediate cloud edge where the loss of optical depth dominates the microphysical effect. This signature appears to be of a greater influence on channel 3 reflectance than variations in cloud and sun-cloud-satellite geometry, and is even observed in individual convective turrets within a stratocumulus cloud field. The effect is also observed at cloud edges other than those resulting from the convective circulation within a cloud element, such as the clear areas due to turbulent mixing associated with the Catalina Eddy in CS3. Channel 1 reflectance measurements in cloud elements show a decrease in reflectance towards the cloud edge as a result of decreasing optical depth.

Model cloud reflectance calculations suggest that higher solar reflectances occur with droplet size distributions that have a strong peak at the modal radius, while lower reflectance results from a broader and less strongly peaked droplet size distribution. The trend observed in the reflectance/aircraft data support this dependence. The mean droplet size measurements in marine environments correspond to the larger droplet sizes

which are shifted in reflectance towards the values represented by the broad model droplet size distribution; while continentally influenced values are shifted toward the strongly peaked model droplet size distribution reflectances. The droplet spectra histograms reveal the change between environments and the consistency with the modeled expectations.

The relationship between channel 3 reflectance and mean cloud droplet radius illustrated in this thesis indicates the potential to make accurate estimations of the microphysical properties of the MABL based upon satellite data. Even with the limited sample contained herein, mean cloud droplet sizes can be estimated within an approximate range of $3\mu\text{m}$ with 95% confidence for mean cloud droplet sizes less than $10\mu\text{m}$ in stratocumulus clouds of sufficient optical depth. At larger mean radii, the small change in channel 3 reflectance with varying droplet size make the estimation more difficult. The precision of this estimation should improve as more reflectance/droplet size correlations are made in future research.

Observations of reflectance from channels 1 and 3 have the potential to reveal the location, extent, and the horizontal microphysical variability of sub-synoptic scale phenomena such as land-sea breeze circulations, topographically induced features such as the Catalina Eddy, gravity waves, and sources of natural and industrial pollution. Such a capability may provide a tool to ascertain the impact of events such as forest fires, industrial accidents, or volcanic activity on the environment.

B. RECOMMENDATIONS

Future observations of marine stratocumulus clouds, such as those which will occur in conjunction with the next FIRE marine stratocumulus IFO tentatively scheduled for July 1990 at an undetermined site, should include plans to vector aircraft across strong continental marine air mass boundaries on short notice by experiment team members collecting real-time AVHRR data. Ideally, the aircraft would perform a cloud sounding leg of 100+ nautical miles centered on the air mass interface, with the sounding leg being coincident with the satellite overpass subsequent to the overpass used to localize the region of interest. Instructions concerning the location of applicable sampling locations could be relayed to aircraft enroute to its geographic objective. Likewise, samples through individual cloud elements should be performed as close as possible to satellite overpass times. This would allow precise correlation between measured reflectance and cloud elements, and would provide the opportunity for measurements to be performed in local, short-duration phenomena such as ship effluent tracks. This would also avoid

the "hit-or-miss" strategy of sampling specific features within the stratocumulus cloud field.

The connection between channel 3 reflectance and MABL turbulence needs to be examined. Entity type entrainment mixing (ETEM), discussed by Telford and Wagner (1981) and Telford *et al.* (1984), may describe the interaction between the stratocumulus cloud top and the subsidence inversion. ETEM in a stratocumulus cloud regime changes little in the horizontal in the absence of topographic influences. The entrainment results in a gradient of cloud droplet sizes at the cloud top, with the depth of this gradient dependent upon the strength of turbulent energy within the MABL. This droplet size gradient is within the depth of the cloud acting as the source of channel 3 reflectance. It is possible that changes in cloud top entrainment due to turbulence variations caused by changes in sea-surface temperature, MABL wind speed, and synoptic forcing could affect channel 3 reflectance sufficiently enough to reduce the precision of cloud droplet size estimation techniques. It has been shown that entrainment near the edge of individual cloud elements has a significant effect on channel 3 reflectance. Accounting for the effect of turbulence on solar reflectance will allow estimations of cloud droplet size distribution to be more closely correlated to the aerosol environment within the MABL since the CCN composition would dominate the factors affecting cloud droplet size distribution.

Variations in reflectance due to anisotropy need to be described in greater detail. As mentioned in Chapter II, the anisotropic reflectance factors provided by Taylor and Stowe (1984) represent spectrally integrated values for wavelengths between $0.2\mu\text{m}$ and $50\mu\text{m}$, are based on a finite number of NIMBUS-7 data, and represent an average value for a discrete angular bin. It is likely that the anisotropic reflectance factors vary as a function of wavelength. Regardless of the quality of any smoothing routine designed to approximate the effect of anisotropy over the entire domain of reflective surfaces, satellite and solar zenith angles, and relative azimuth angles, it will only be as good as the accuracy of the original bin values. As the availability of anisotropic reflectance data grows, the revised measurements should be incorporated into any scheme dependent upon the conversion of directional reflectance to isotropic reflectance.

The effect of changing cloud reflectance due to spatial variations in aerosol concentration and composition on the global climate must be incorporated into climate models. As discussed by Twomey *et al.* (1984), slight variations in cloud-related parameters in global climate models results in a considerable climatic response. Failure to

consider clouds as reflectance "variables" may lead to an underestimate of global albedo. The simplicity of the technique utilized in this thesis makes it ideal for performing climatological studies through the use of archived AVHRR data. Through a study such as this, temporal trends in cloud reflectance due to microphysical variations could be identified. This potential may be especially valuable in describing the influence of DMS on cloud albedo over remote oceanic regions where in-situ measurements are impractical.

Model reflectance data should be assimilated in preparation for the new $1.6\mu\text{m}$ imaging channel to be included with the AVHRR instrument on future satellites. As suggested by Wetzell and Vonder Haar (1986), the implementation of this new sensor coupled with the potential for testing and utilizing more sophisticated sensors on Defense Meteorological Satellite Program (DMSP) and GOES platforms provides impetus for increasing focus on the applications of NIR satellite imagery in determining cloud microphysical structure. The ability to cross-correlate NIR reflectance from two separate wavelength bands will enable more precise determinations of cloud microphysical characteristics.

APPENDIX COMPOSITE IMAGES

The composite RGB images for each of the nine case study subscenes are shown in Fig. 76 through 84. The line segments indicate reflectance cross-sections corresponding to those which appear in the monochromatic imagery in Chapter IV. Chapter III explains the interpretation of these images.

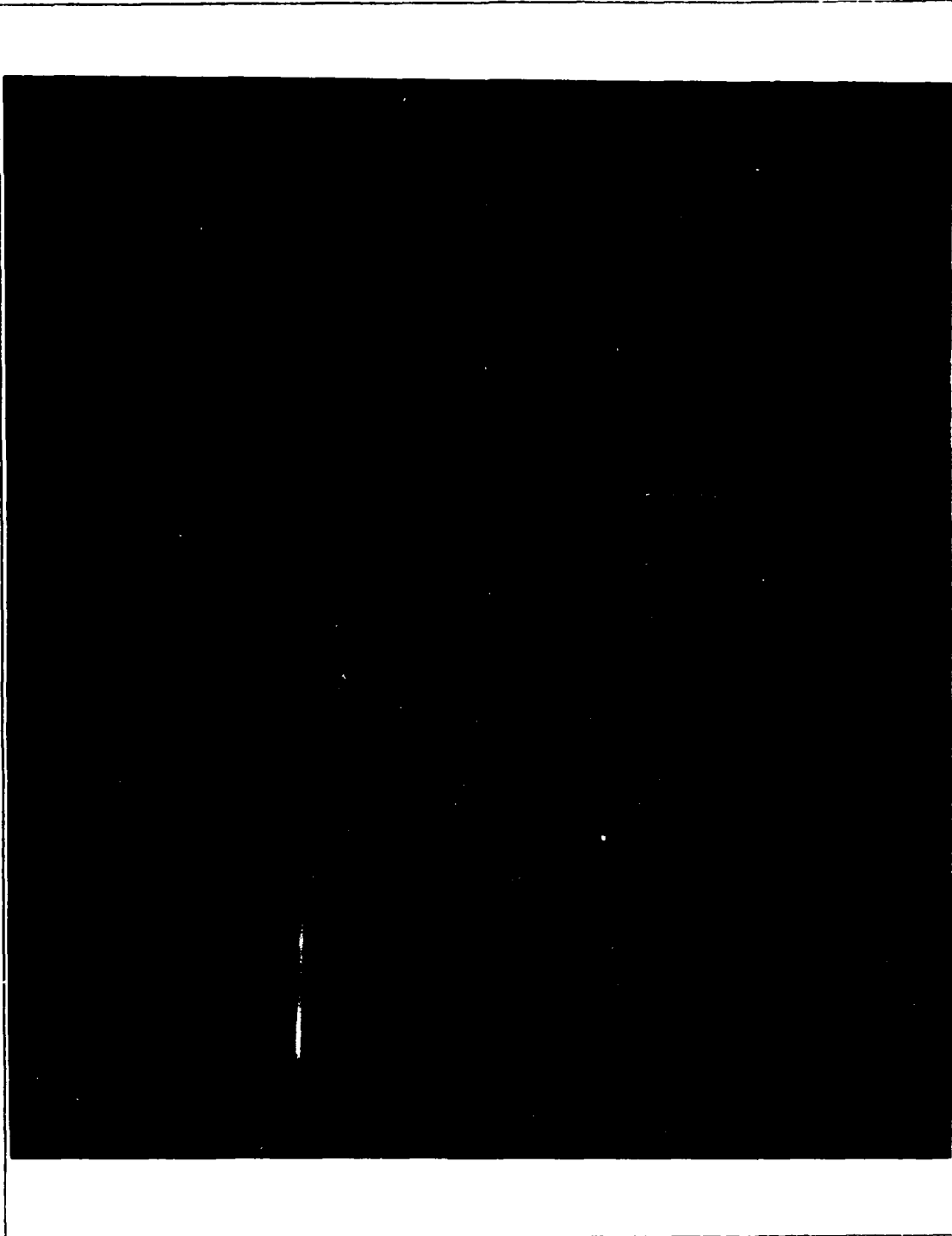


Fig. 76. NOAA-10 AVHRR 1639 UTC 28 June 1987 Composite Image

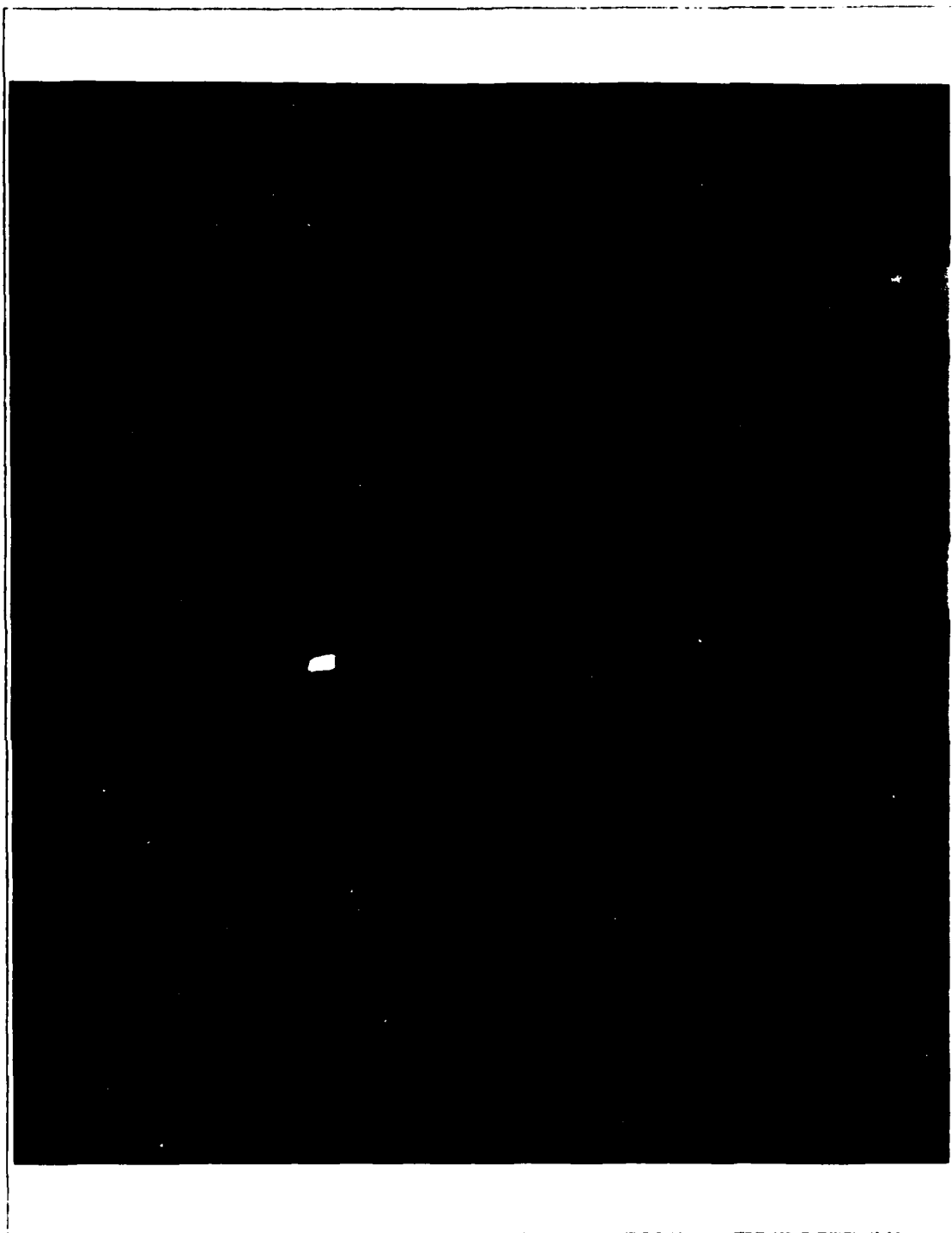


Fig. 77. NOAA-9 AVHRR 2230 UTC 29 June 1987 Composite Image

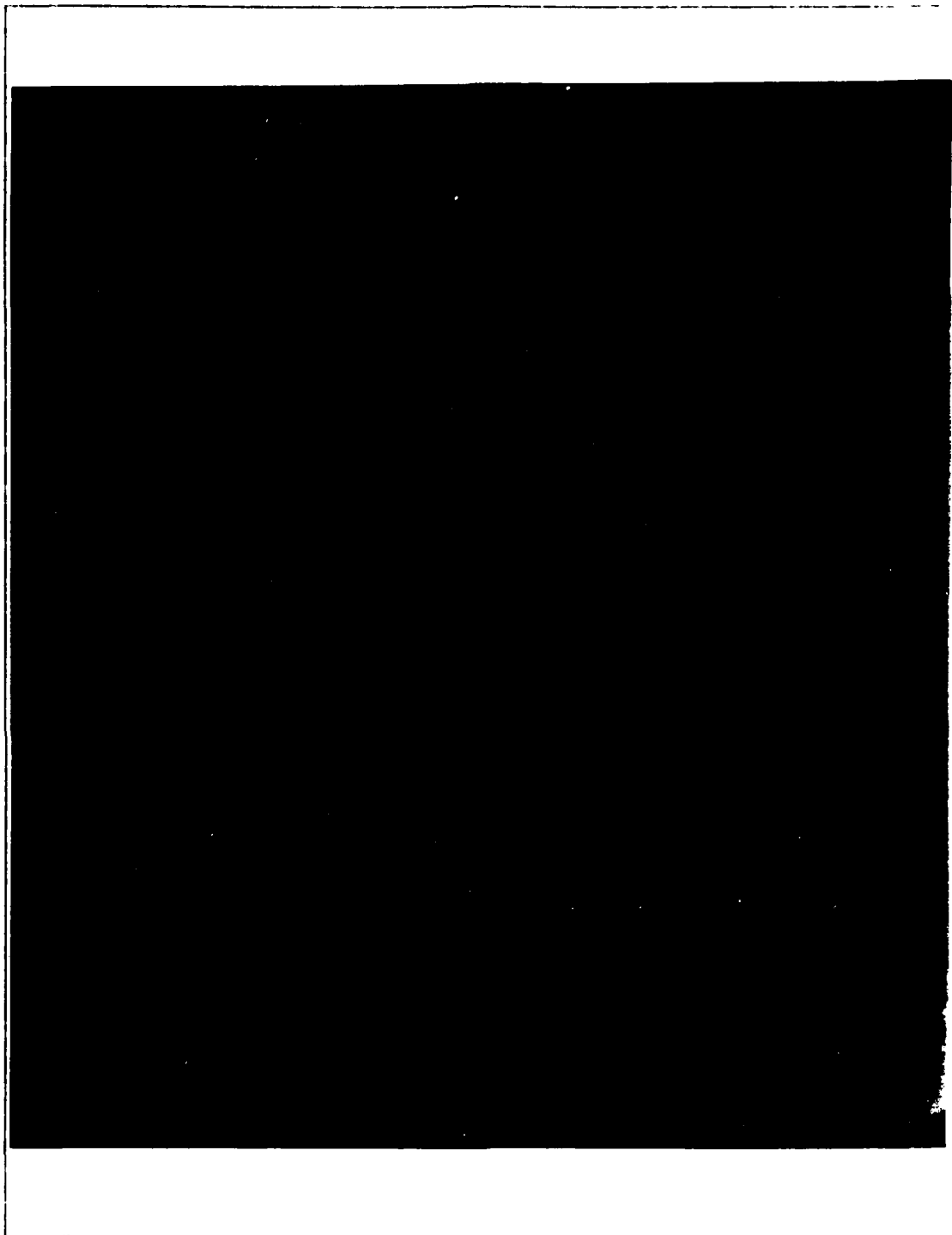


Fig. 78. NOAA-10 AVHRR 1555 UTC 30 June 1997 Composite Imag

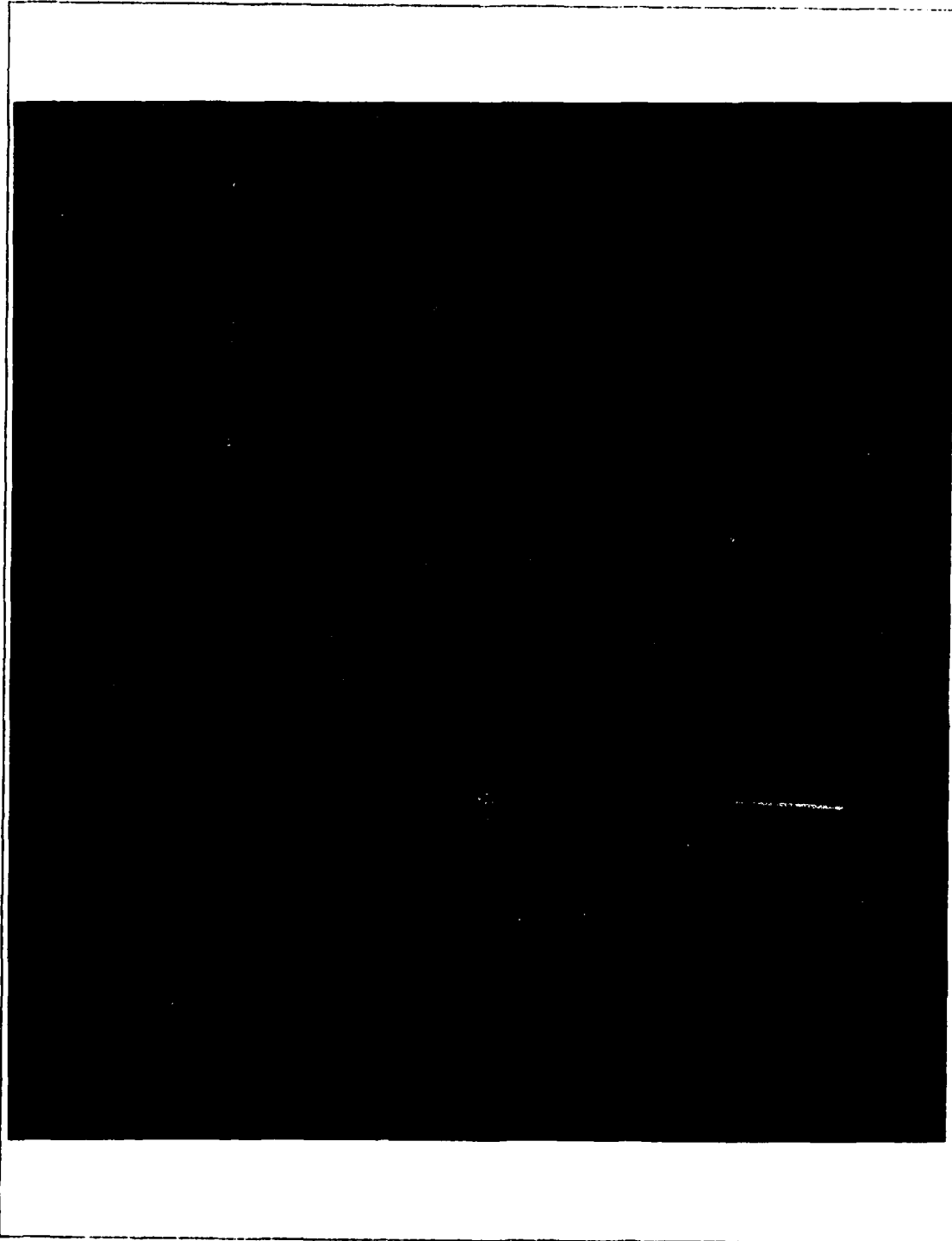


Fig. 79. NOAA-10 AVHRR 1613 UTC 13 July 1987 Composite Imag.

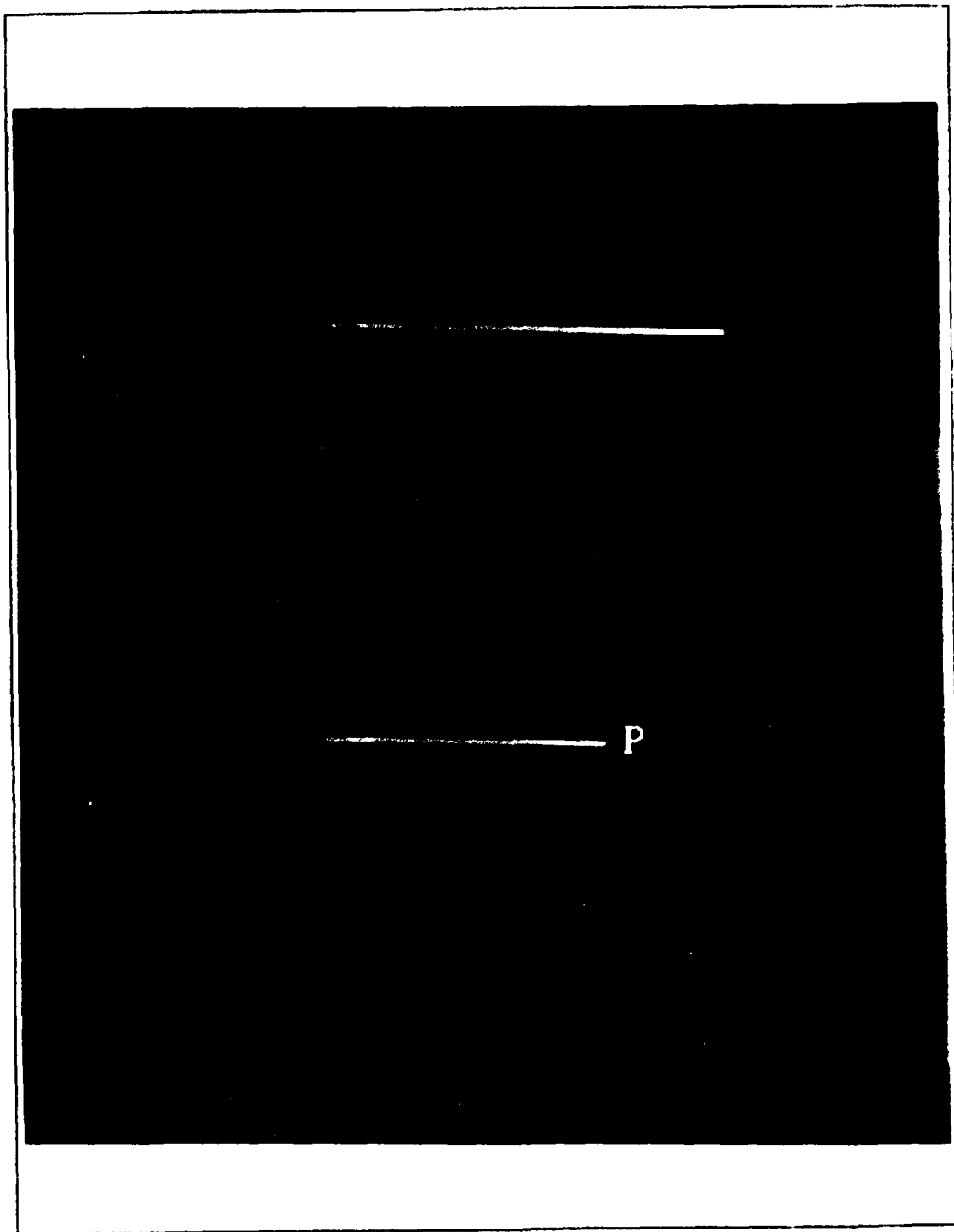


Fig. 80. NOAA-9 AVHRR 2321 UTC 13 July 1987 Composite Image

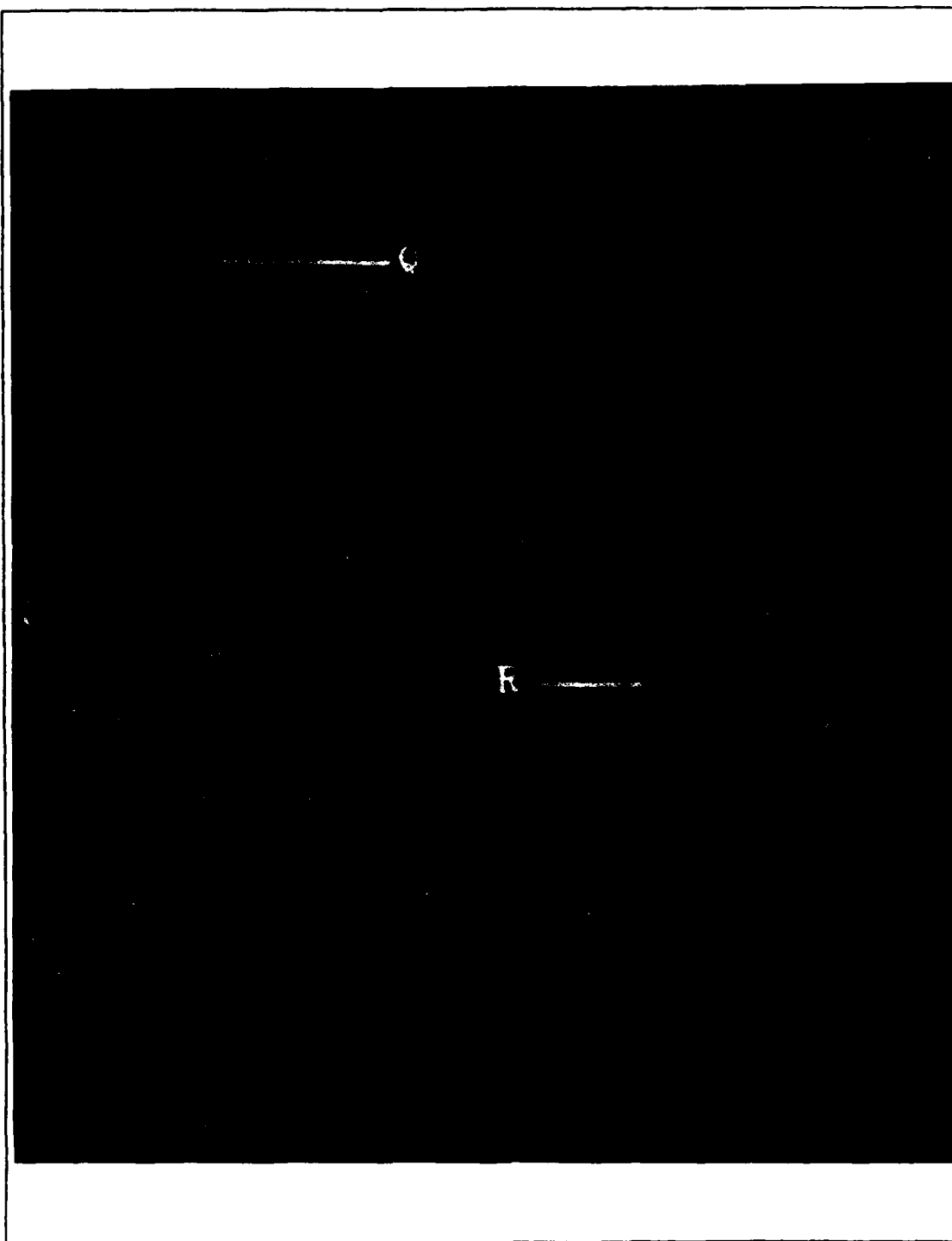


Fig. 81. NOAA-10 AVHRR 1551 UTC 14 July 1987 Composite Image

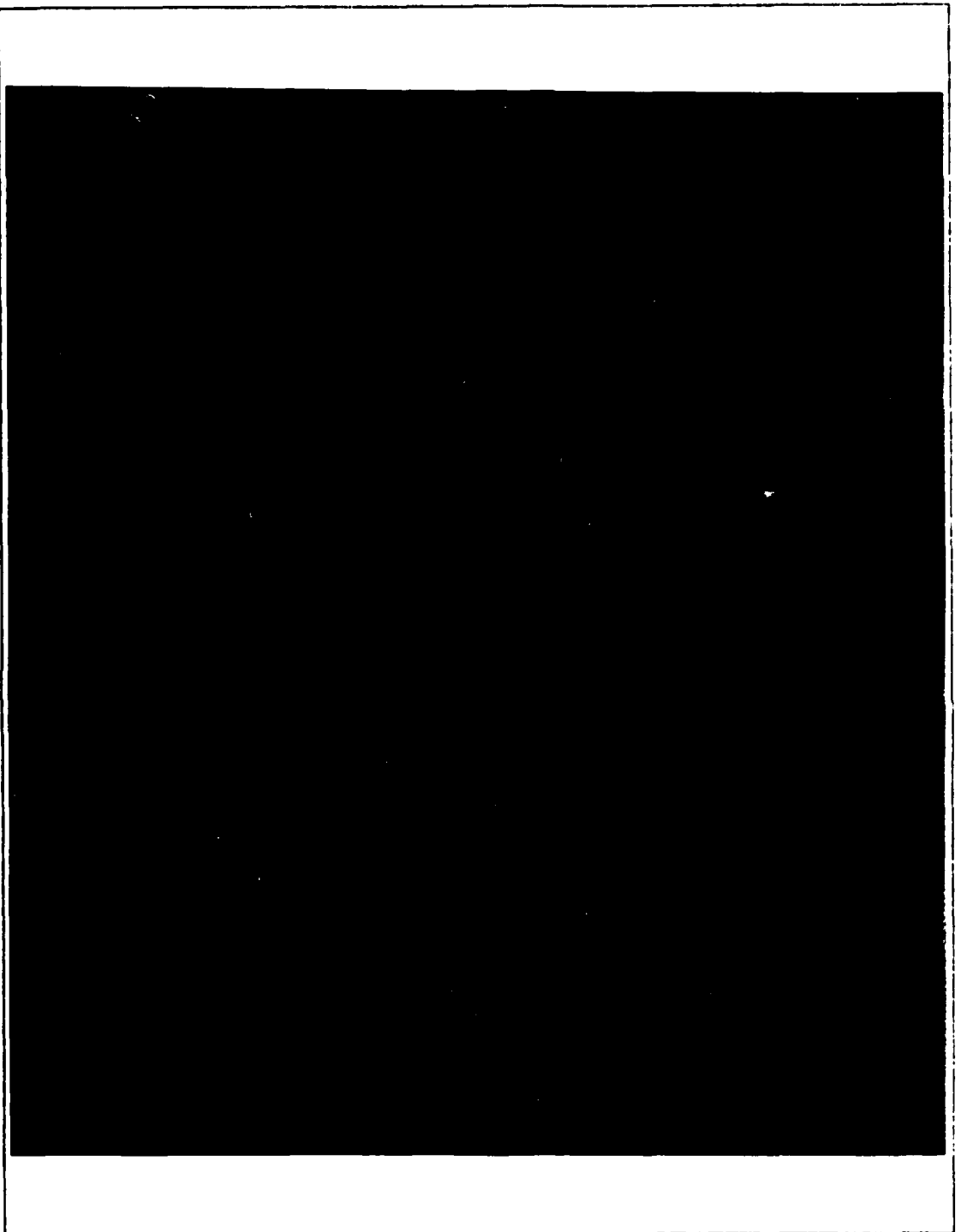
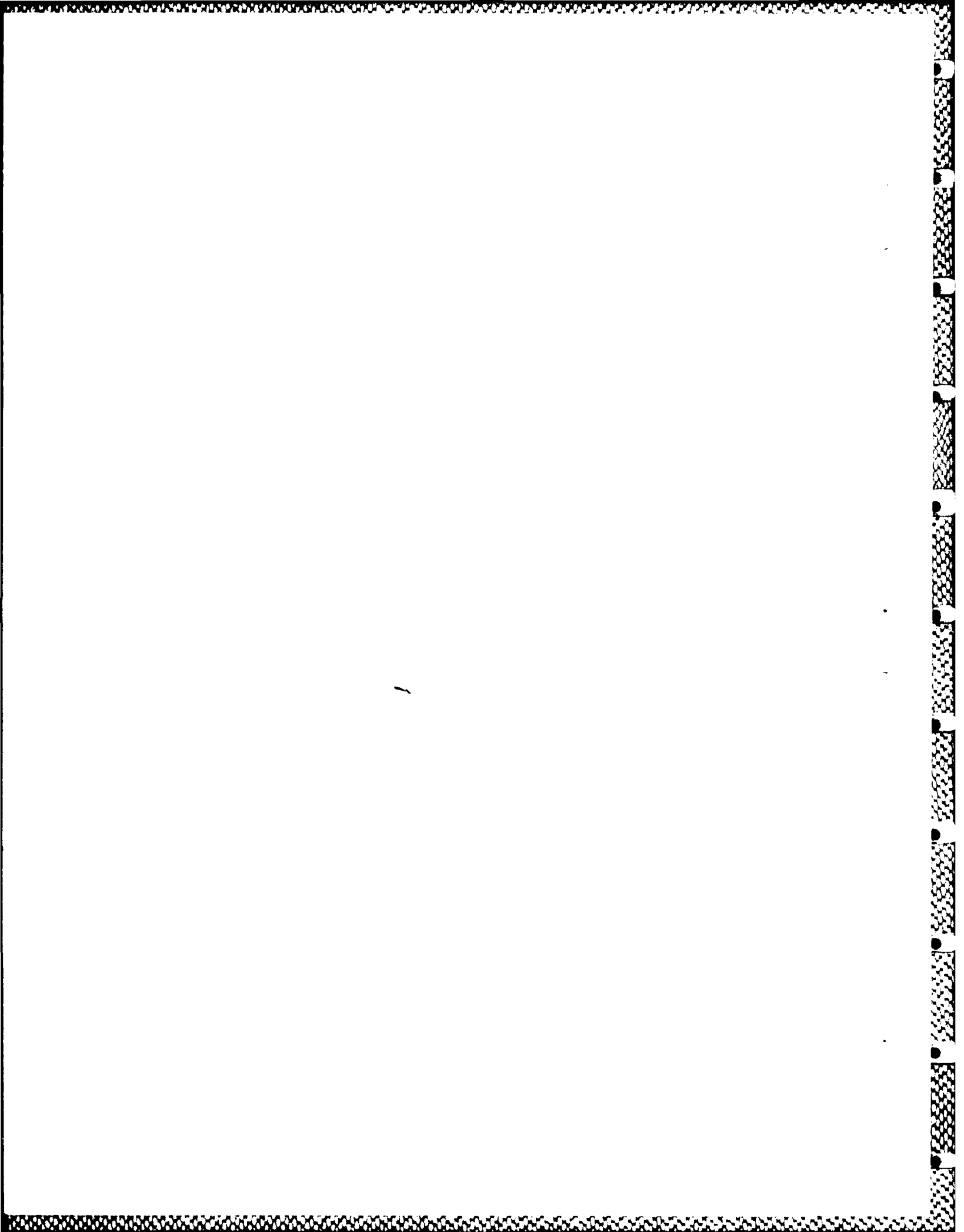


Fig. 82. NOAA-9 AVHRR 2310 UTC 14 July 1987 Composite Image



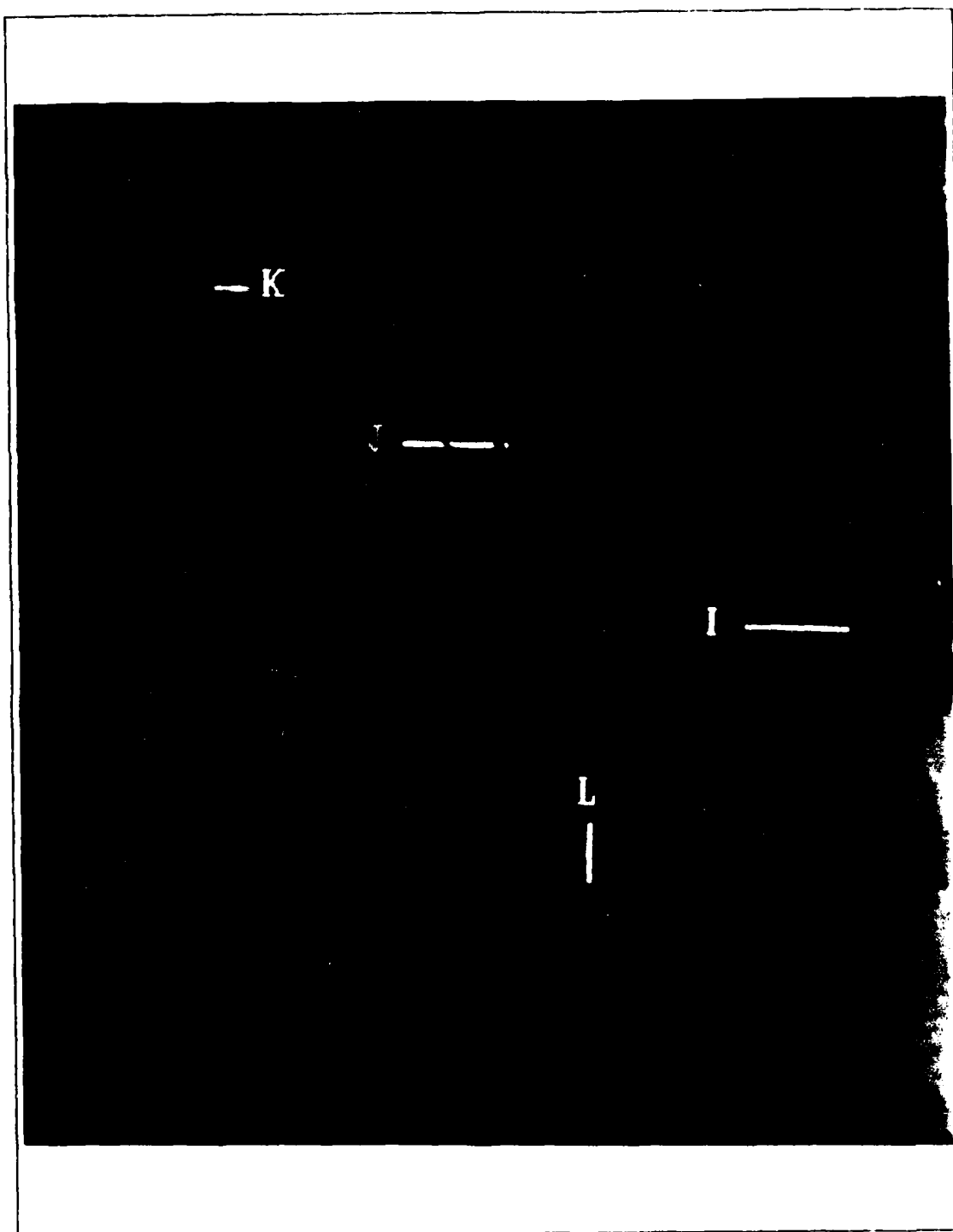


Fig. 83. NOAA-10 AVHRR 1524 UTC 6 July 1987 Composite Image



Fig. 84. NOAA-10 AVHRR 1604 UTC 18 July 1987 Composite Image

LIST OF REFERENCES

- Allen, R. C., Jr., 1987: Automated satellite cloud analysis: A multispectral approach to the problem of snow/cloud discrimination. M.S. thesis, Naval Postgraduate School, Monterey, CA.
- Arking, A. and J. D. Childs, 1985: Retrieval of cloud cover parameters from multispectral satellite images. *J. Climate Appl. Meteor.*, **24**, 322-333.
- Bell, G. J. and M. C. Wong, 1981: The near-infrared radiation received by satellites from clouds. *Mon. Wea. Rev.*, **109**, 2158-2163.
- Bloembergen, N., C. K. Patel and G. Pake (chairpersons), 1987: Science and Technology of Directed Energy Weapons. Report of the American Physical Society Study Group, *Reviews of Modern Physics*, **59**, S1- S202.
- Brock, J. R., 1972: Condensation growth of atmospheric aerosols. *Aerosols and Atmospheric Chemistry* (G. M. Hidy, Ed.), Academic Press, New York, 149-153.
- Chahine, M. T., D. J. McCleese, P. W. Rosenkranz and D. H. Staelin, 1983: Interaction mechanisms within the atmosphere. *Manual of Remote Sensing* (R. N. Colwell, Ed.), 2d ed., Vol. 1, Sheridan Press, New York, 165-230.
- Charlson, R. J., J. E. Lovelock, M. O. Andreae, and S. G. Warren, 1987: Oceanic phytoplankton, atmospheric sulphur, cloud albedo and climate. *Nature*, **326**, 655-661.
- Coakley, J. A., Jr., R. L. Bernstein and P. A. Durkee, 1987: Effect of ship-stack effluents on cloud reflectivity. *Science*, **237**, 953-1084.
- Coakley, J. A., Jr., R. D. Cess and F. B. Yurevich, 1983: The effect of tropospheric aerosols on the earth's radiation budget: A parameterization for climate models. *J. Atmos. Sci.*, **40**, 116-138.
- Coakley, J. A., Jr., and R. Davies, 1986: The effect of cloud sides on reflected solar radiation as deduced from satellite observations. *J. Atmos. Sci.*, **43**, 1025-1035.
- Cordray, D. M., J. W. Fitzgerald, S. G. Gathman, J. N. Hayes, J. E. Kenney, G. P. Mueller and R. E. Ruskin, 1977: Meteorological Sensitivity Study on High Energy Laser Propagation. Naval Research Laboratory Report 8097, Washington, D.C., 81 pp.
- Cox, S. K., D. S. McDougal, D. A. Randall and R. A. Schiffer, 1987: FIRE-The First ISCCP Regional Experiment. *Bull. Amer. Meteor. Soc.*, **68**, 114-118.
- Deirmendjian, D., 1969: Electromagnetic scattering on spherical polydispersions. Elsevier, New York, 290pp.

- Hansen, J. E. and J. B. Pollack, 1970: Near-infrared light scattering by terrestrial clouds. *J. Atmos. Sci.*, **27**, 265-281.
- Hansen, J. E. and L. D. Travis, 1974: Light scattering in planetary atmospheres. *Space Sci. Rev.*, **16**, 527-610.
- Hindman, E. E., II, P. V. Hobbs and L. F. Radke, 1977: Cloud condensation nucleus size distributions and their effects on cloud droplet size distributions. *J. Atmos. Sci.*, **34**, 951-956.
- Hunt, G. E., 1972: Radiative properties of terrestrial clouds at visible and infra-red thermal window wavelengths. *Quart. J. R. Met. Soc.*, **99**, 346-369.
- Joseph, J. H., W. J. Wiscombe and J. A. Weinman, 1976: The delta-Eddington approximation for radiative flux transfer. *J. Atmos. Sci.*, **33**, 2452-2459.
- Kloesel, K. A., B. A. Albrecht and D. P. Wylie, 1988: FIRE Marine Stratocumulus Observations -- Summary of Operations and Synoptic Conditions. FIRE Technical Report No. 1, Penn State Univ., State College, PA, 171 pp.
- Lauritson, L., G. J. Nelson and F. W. Porto, 1979: Data Extraction and Calibration of TIROS-N NOAA Radiometers. NOAA Technical Memorandum NESS 107, U.S. Dept. of Commerce, Washington, D.C., Appendix B.
- Liou, K. N., 1980: An Introduction to Atmospheric Radiation. Academic Press, New York, 392 pp.
- McKee, T. B. and J. T. Klehr, 1978: Effects of cloud shape on scattered solar radiation. *Mon. Wea. Rev.*, **106**, 399-404.
- Miller, E. R. and R. B. Friesen, 1987: Standard Output Data Products from the NCAR Research Aviation Facility. Bulletin No. 9, National Center for Atmospheric Research, Boulder, CO, 69 pp.
- Milton, A. F., G. L. Harvey and A. W. Schmidt, 1977: Comparison of the 3-5 Micrometer and 8-12 Micrometer Regions for Advanced Thermal Imaging Systems: LOWTRAN Revisited. Naval Research Laboratory Report 8172, Washington, D.C., 35 pp.
- Noonkester, V. R., 1984: Droplet spectra observed in marine stratus cloud layers. *J. Atmos. Sci.*, **41**, 829-845.
- Randall, D. A., J. A. Coakley, Jr., C. W. Fairall, R. A. Kropfli and D. H. Lenschow, 1984: Outlook for research on subtropical marine stratiform clouds. *Bull. Amer. Meteor. Soc.*, **65**, 1290-1301.
- Rogers, J. M., 1987: Investigation of Anomalous Cloud Features in 3.7 Micrometer Satellite Imagery. M. S. thesis, Naval Postgraduate School, Monterey, CA.
- Rogers, R. R., 1979: A Short Course in Cloud Physics. 2d ed., Pergamon Press, New York, 235 pp.

- Ruff, I. and A. Gruber, 1983: Multispectral identification of clouds and earth surfaces using AVHRR radiometric data. *Fifth Conf. on Atmospheric Radiation*, NOAA/NESDIS, Washington, D.C., 475-478.
- Slinn, W. G. N., 1975: Atmospheric aerosol particles in surface-level air. *Atmospheric Environment*, **9**, 763-764.
- Taylor, V. R., and L. L. Stowe, 1984: Atlas of Reflectance Patterns for Uniform Earth and Cloud Surfaces (NIMBUS-7 ERB--61 days). NOAA Tech. Rep. NESDIS 10, U.S. Dept. of Commerce, Washington, D.C., 66 pp.
- Telford, J. W., T. S. Keck and S. K. Chai, 1984: Entrainment at cloud tops and the droplet spectra. *J. Atmos. Sci.*, **41**, 3170-3179.
- Telford, J. W. and P. B. Wagner, 1981: Observations of condensation growth determined by entity type mixing. *Pure Appl. Geophys.*, **119**, 934-965.
- Twomey, S., 1977: The influence of pollution on the shortwave albedo of clouds. *J. Atmos. Sci.*, **34**, 1149-1152.
- Twomey, S. and T. Cocks, 1982: Spectral reflectance of clouds in the near-infrared: comparison of measurements and calculations. *J. Meteor. Soc. Japan*, **60**, 583-592.
- Twomey, S., M. Piepgrass and T. L. Wolfe, 1984: An assessment of the impact of pollution on global cloud albedo. *Tellus*, **36B**, 356-366.
- Twomey, S. and J. Warner, 1967: Comparison of measurements of cloud droplets and cloud nuclei. *J. Atmos. Sci.*, **24**, 702-703.
- Wakimoto, R. M., 1987: The Catalina Eddy and its effect on pollution over southern California. *Mon. Wea. Rev.*, **115**, 837-855.
- Warner, J. and S. Twomey, 1967: The production of cloud nuclei by cane fires and the effect on cloud droplet concentration. *J. Atmos. Sci.*, **24**, 704-706.
- Welch, R. M., S. K. Cox and J. M. Davis, 1980: Solar Radiation and Clouds. *Meteor. Monogr.*, No. 39, Amer. Meteor. Soc., 96 pp.
- Wetzel, M. and T. Vonder Haar, 1986: Modeling and observation of near-IR cloud signatures in the marine boundary layer. *Fourth Tri-Service Cloud Modeling Workshop*, Air Force Geophysics Laboratory, Hanscom Air Force Base, MA, 50-63.
- Wiscombe, W. J., 1980: Improved Mie scattering algorithms. *Applied Optics*, **19**, 1505-1509.

INITIAL DISTRIBUTION LIST

	No. Copies
1. Defense Technical Information Center Cameron Station Alexandria, VA 22304-6145	2
2. Library, Code 0142 Naval Postgraduate School Monterey, CA 93943-5002	2
3. Chief of Naval Research 800 N. Quincy Street Arlington, VA 22217-5000	1
4. Oceanographer of the Navy Naval Observatory 34th and Massachusetts Avenue NW Washington, DC 20390-5000	1
5. Commander Naval Oceanography Command NSTL, MS 39522-5000	1
6. Commanding Officer Fleet Numerical Oceanography Center Monterey, CA 93943-5005	1
7. Chairman, Code 63Rd Department of Meteorology Naval Postgraduate School Monterey, CA 93943-5000	1
8. Chairman, Code 68Co Department of Oceanography Naval Postgraduate School Monterey, CA 93943-5000	1
9. Professor Philip A. Durkee, 63De Naval Postgraduate School Monterey, CA 93943-5000	2
10. Professor Carlyle H. Wash, 63Wx Naval Postgraduate School Monterey, CA 93943-5000	1
11. LT Gary M. Mineart COMPHIBGRU ONE FPO San Francisco, CA 96601-6006	4

- | | | |
|-----|----------------------------------------------------------------------------------------------------------------|---|
| 12. | Commanding Officer
Naval Environmental Prediction
Research Facility
Monterey, CA 93943-5006 | 1 |
| 13. | Chairman, Oceanography Department
U.S. Naval Academy
Annapolis, MD 21402-5000 | 1 |
| 14. | Library
Scripps Institution of Oceanography
P.O. Box 2367
La Jolla, CA 92037-5000 | 1 |
| 15. | Library Acquisitions
National Center for Atmospheric Research
P.O. Box 3000
Boulder, CO 80307-5000 | 1 |
| 16. | CAPT Marshall P. Waters III, USNR
Oceanography Department
U.S. Naval Academy
Annapolis, MD 21402-5000 | 1 |